

Field Line Resonance in Two and a Half Dimensions

DRAFT VERSION CREATED ON APRIL 8, 2016

© Charles A. McEachern 2016



The text of this work is licensed under a Creative Commons Attribution-ShareAlike 4.0 International license.

⁵ Acknowledgements

⁶ Acknowledgement placeholder.

⁷ Dedication

⁸ Dedication placeholder.

Abstract

¹⁰ Abstract placeholder.

Contents

¹¹	Acknowledgements	i
¹³	Dedication	ii
¹⁴	Abstract	iii
¹⁵	List of Tables	vii
¹⁶	List of Figures	viii
¹⁷	1 Introduction	1
¹⁸	1.1 Structure of the Present Work	2
¹⁹	2 The Near-Earth Environment	4
²⁰	2.1 The Outer Magnetosphere	4
²¹	2.2 The Inner Magnetosphere	6
²²	2.3 The Ionosphere	8
²³	2.4 Geomagnetic Storms and Substorms	9
²⁴	3 Field Line Resonance	11
²⁵	3.1 Harmonic Structure	14
²⁶	3.2 Azimuthal Modenumber	17
²⁷	3.3 Poloidal and Toroidal Polarizations	18
²⁸	3.4 Giant Pulsations	20
²⁹	3.5 Motivations for the Present Work	21

30	4 Waves in Cold Resistive Plasma	24
31	4.1 Guided Propagation	26
32	4.2 Compressional Propagation	27
33	4.3 High Altitude Limit	29
34	4.4 Implications to the Present Work	30
35	5 “Tuna Half” Dimensional Model	32
36	5.1 Coordinate System	33
37	5.2 Physical Parameter Profiles	37
38	5.3 Driving	40
39	5.4 Maxwell’s Equations	43
40	5.5 Boundary Conditions	47
41	6 Electron Inertial Effects	52
42	6.1 The Boris Factor	53
43	6.2 Parallel Currents and Electric Fields	55
44	6.3 Inertial Length Scales	61
45	6.4 Discussion	62
46	7 Numerical Results	64
47	7.1 Modenumber and Compression	64
48	7.2 Resonance and Rotation on the Dayside	70
49	7.3 Resonance and Rotation on the Nightside	77
50	7.4 Ground Signatures and Giant Pulsations	81
51	7.5 Discussion	85
52	8 Observations	87
53	8.1 Sampling Bias and Event Selection	87
54	8.2 Events by Mode	91
55	8.3 Events by Amplitude	95
56	8.4 Events by Frequency	99
57	8.5 Events by Phase	101
58	8.6 Discussion	106

59	9 Conclusion	107
60	9.1 Summary of Results	107
61	9.2 Future Work	107
62	References	109

⁶³ List of Tables

⁶⁴	3.1 IAGA Magnetic Pulsation Frequency Bands	12
⁶⁵	5.1 Typical Parameters for the Tuna Density Profile	38
⁶⁶	5.2 Integrated Atmospheric Conductivity	48

⁶⁷ **List of Figures**

68	2.1 Outer Magnetosphere Cutaway	5
69	2.2 Inner Magnetosphere Cutaway	7
70	3.1 Alfvén Bounce Frequencies	13
71	3.2 First and Second Harmonic Resonances	15
72	3.3 Large and Small Azimuthal Modenumbers	17
73	3.4 Poloidal Mode Structure	19
74	3.5 Toroidal Mode Structure	20
75	4.1 Compressional Alfvén Wave Cutoff Frequencies	31
76	5.1 Nonorthogonal Dipole Grid	37
77	5.2 Alfvén Speed Profiles	39
78	5.3 Ionospheric Conductivity Profiles	40
79	5.4 Decreasing Penetration with Increasing Modenumber	42
80	5.5 Sym-H for June 2013 Storm	43
81	6.1 Plasma Frequency Profile	54
82	6.2 Electric Field Snapshots	56
83	6.3 Current and Poynting Flux at 100 km	57
84	6.4 Current and Poynting Flux at 1000 km	59
85	6.5 Power Density at the Ionosphere	60
86	6.6 Parallel Electric Fields by Perpendicular Grid Resolution	62
87	7.1 Magnetic Field Snapshots from a Small- m Run	67
88	7.2 Magnetic Field Snapshots from a Large- m Run	68
89	7.3 Compressional Coupling to the Poloidal Mode	69
90	7.4 Dayside Poloidal and Toroidal Energy	74

91	7.5 Dayside Poloidal Energy Distribution	75
92	7.6 Dayside Toroidal Energy Distribution	76
93	7.7 Nightside Poloidal and Toroidal Energy	78
94	7.8 Nightside Poloidal Energy Distribution	79
95	7.9 Nightside Toroidal Energy Distribution	80
96	7.10 Dayside Ground Magnetic Fields	83
97	7.11 Nightside Ground Magnetic Fields	84
98	8.1 Distribution of Usable Van Allen Probe Data	89
99	8.2 Observation Rate of Pc4 Events	92
100	8.3 Observation Rate of Pc4 Events by Mode	94
101	8.4 Amplitude Distribution of Pc4 Events by Mode	96
102	8.5 Waveforms and Spectra for a Strong Pc4 Event	97
103	8.6 Observation Rate of Pc4 Events by Mode and Amplitude	98
104	8.7 Frequency Distribution of Pc4 Events by Mode	99
105	8.8 Observation Rate of Pc4 Events by Mode and Frequency	100
106	8.9 Waveforms and Spectra for a Pc4 Event	103
107	8.10 Phase Distribution of Pc4 Events by Mode	104
108	8.11 Observation Rate of Pc4 Events by Mode and Phase	105

¹⁰⁹ **Chapter 1**

¹¹⁰ **Introduction**

¹¹¹ 1859 was a pivotal year in human history. The United States moved steadily toward
¹¹² the American Civil War, which would abolish slavery and consolidate the power of
¹¹³ the federal government. A slew of conflicts in Southern Europe, such as the Austro-
¹¹⁴ Sardinian War, set the stage for the unification of Italy. The Taiping Civil War — one
¹¹⁵ of the bloodiest conflicts of all time — is considered by many to mark the beginning
¹¹⁶ of modern Chinese history. *Origin of Species* was published. The first transatlantic
¹¹⁷ telegraph cable was laid.

¹¹⁸ Meanwhile, ambivalent to humanity, the Sun belched an intense burst of charged parti-
¹¹⁹ cles and magnetic energy directly at Earth. The resulting geomagnetic storm¹ caused
¹²⁰ telegraph systems to fail across the Western hemisphere, electrocuting operators and
¹²¹ starting fires[35, 96]. Displays of the northern lights were visible as far south as Cuba.

¹²² The Solar Storm of 1859 was perhaps the most powerful in recorded history, but by no
¹²³ means was it a one-time event. The Sun discharges hundreds of coronal mass ejections
¹²⁴ (CMEs) per year, of all sizes, in all directions. In fact, a comparably large CME narrowly
¹²⁵ missed Earth in 2012[72]. Had it not, it's estimated it would have caused widespread,
¹²⁶ long-term electrical outages, with a damage toll on the order of 10^{12} dollars[66].

¹The Solar Storm of 1859 is also called the Carrington Event, after English astronomer Richard Carrington. He drew a connection between the storm's geomagnetic activity and the sunspots he had observed the day before.

127 The Sun’s extreme — and temperamental — effect on Earth’s magnetic environment
128 makes a compelling case for the ongoing study of space weather. Such research has
129 evolved over the past century from sunspot counts and compass readings to multi-
130 satellite missions and supercomputer simulations. Modern methods have dramatically
131 increased humanity’s understanding of the relationship between the Sun and the Earth;
132 however, significant uncertainty continues to surround geomagnetic storms, substorms,
133 and the various energy transport mechanisms that make them up.

134 The present work focuses in particular on the phenomenon of field line resonance: Alfvén
135 waves bouncing between the northern and southern hemispheres. Such waves play an
136 important part in the energization of magnetospheric particles, the transport of energy
137 from high to low altitude, and the driving of currents at the top of the atmosphere.

138 **TODO:** More is needed before we can jump into a description of the present work.
139 Introduce what we’re working on a bit ore specifically. Talk about how space is a
140 laboratory that teaches us about plasma in a way that’s relevant to both astrophysics
141 and fusion reactors, which are hard to measure. Fishbone instability.

142 1.1 Structure of the Present Work

143 Chapter 2 surveys the near-Earth environment. Prominent features of the magneto-
144 sphere are defined. The response of the magnetosphere to transient solar wind events
145 is summarized.

146 Chapter 3 introduces the field line resonance phenomenon, in terms of both the under-
147 lying physics and notable work on the topic. Jargon is introduced to clarify important
148 elements of wave structure. Several open questions about field line resonances (FLRs)
149 are offered as motivations for the present work.

150 Chapter 4 lays the groundwork for a numerical model by exploring the fundamental
151 equations of waves in a cold, resistive plasma — such as Earth’s magnetosphere. Char-
152 acteristic scales are gleaned from the resulting dispersion relations.

- 153 Chapter 5 presents Tuna, a new two and a half dimensional simulation designed specif-
154 ically for the realistic modeling of FLRs. Tuna’s non-orthogonal geometry, height-
155 resolved ionosphere, novel driving mechanism, and coupling to the atmosphere are ex-
156 plained.
- 157 Chapter 6 considers the addition of electron inertial effects to Tuna, touches on what
158 can be learned from them, and shows that they incur an unreasonable computational
159 cost. (Electron inertia is neglected in the results presented in other chapters.)
- 160 Chapter 7 describes the core numerical results of the work, unifying several of the
161 questions posed in Chapter 3. Significant depth is added to past work on finite poloidal
162 lifetimes[64, 78]. Interplay between poloidal-toroidal coupling, shear-compressional cou-
163 pling, and Joule dissipation is considered from several angles.
- 164 Chapter 8 puts the numerical results in physical context through the analysis of data
165 from the Van Allen Probes mission. FLR occurrence rates are considered in terms of
166 location, mode structure, and polarization – parameters which have been only partially
167 addressed by other recent FLR surveys[17, 70].
- 168 Chapter 9 briefly summarizes the results shown in the above chapters — the code
169 development, analysis of numerical results, and satellite observation — and suggests
170 further directions.

¹⁷¹ **Chapter 2**

¹⁷² **The Near-Earth Environment**

¹⁷³ From Earth’s surface to a height of a hundred kilometers or so, the atmosphere is a
¹⁷⁴ well-behaved fluid: a collisional ensemble of neutral atoms. Higher up, its behavior
¹⁷⁵ changes dramatically. As altitude increases, solar ultraviolet radiation becomes more
¹⁷⁶ intense, which ionizes atmospheric atoms. Density also decreases, slowing collisional
¹⁷⁷ recombination. Whereas the neutral atmosphere is held against Earth’s surface by
¹⁷⁸ gravity, the motion of charged particles is dominated by Earth’s geomagnetic field, as
¹⁷⁹ well as the electromagnetic disturbances created as that field is hammered by the solar
¹⁸⁰ wind.

¹⁸¹ The present section outlines the structure of the magnetosphere; that is, the region of
¹⁸² space governed primarily by Earth’s magnetic field. Particular emphasis is placed on
¹⁸³ structures which relate closely to field line resonance.

¹⁸⁴ **2.1 The Outer Magnetosphere**

¹⁸⁵ Plasma behavior within Earth’s magnetosphere is ultimately driven by the solar wind: a
¹⁸⁶ hot (~ 100 eV), fast-moving (~ 100 km/s) plasma threaded by the interplanetary magnetic
¹⁸⁷ field (~ 1 nT)¹. The density of the solar wind is on the order of 10^6 /cm³; in a laboratory

¹Listed values correspond to the solar wind at Earth’s orbit.

188 setting, this would constitute an ultra-high vacuum (atmospheric density at sea level is
189 $\sim 10^{19} / \text{cm}^3$), but compared to much of the magnetopause it's quite dense.



Figure 2.1: TODO: The outer magnetosphere...

190 The magnetosphere's outer boundary represents a balance between the solar wind dy-
191 namic pressure and the magnetic pressure of Earth's dipole field. On the dayside, the
192 dipole is compressed, pushing this boundary to within about $10 R_E$ of Earth². The
193 nightside magnetosphere is stretched into a long tail which may exceed $50 R_E$ in width
194 and $100 R_E$ in length.

195 When the interplanetary magnetic field opposes the geomagnetic field at the nose of
196 the magnetosphere, magnetic reconnection occurs. Closed magnetospheric field lines
197 "break," opening up to the interplanetary magnetic field³. They then move tailward

²Distances in the magnetosphere are typically measured in units of Earth radii: $1 R_E \equiv 6378 \text{ km}$.

³Closed field lines connect at both ends to the magnetic dynamo at Earth's core. Open field lines meet Earth at only one end; the other connects to the interplanetary magnetic field. The distinction is important because charged particle motion is guided by magnetic field lines, as discussed in Chapter 3.

198 across the poles, dragging their frozen-in plasma with them⁴. Reconnection in the tail
199 allows magnetic field lines to convect back to the day side, across the flanks. This
200 process is called the Dungey cycle[22].

201 Viewed from the north, the Dungey cycle involves a clockwise flow of flux and plasma on
202 the dusk side and a counterclockwise flow on the dawn side. The motion is accompanied
203 by a convection electric field, per Ohm's law⁵.

204 **TODO:** Jets from magnetic reconnection... release of magnetic tension!

205 Consistent with Ampère's law, the interplanetary magnetic field is separated from the
206 magnetosphere by a current sheet: the magnetopause. On the dayside, the magne-
207 topause current flows duskward; on the nightside, it flows downward around the mag-
208 netail.

209 Plasma within the tail is cool ($\sim 100 \text{ eV}$) and rarefied ($\sim 10^{-2} / \text{cm}^3$). Earth's dipole is
210 significantly deformed in the magnetotail; field lines in the northern lobe of the tail
211 points more or less Earthward, and vice versa. The two lobes are divided by the plasma
212 sheet, which is comparably hot ($\sim 10^3 \text{ eV}$) and dense ($\sim 1 / \text{cm}^3$). The plasma sheet
213 carries a duskward current which connects to the magnetopause current.

214 2.2 The Inner Magnetosphere

215 Within about **TODO:** $L \sim 10$ (where L is the McIlwain parameter⁶), the dipole
216 magnetic field is not appreciably deformed by the solar wind. As a result, the structures
217 in the inner magnetosphere follow closely from the motion of charged particles in an
218 ideal dipole field.

⁴In the outer magnetosphere (as well as most of the inner magnetosphere), collisions are so infrequent that magnetic flux is said to be “frozen in” to the plasma. Charged particles move freely along magnetic field lines, but cannot cross from one line to another. Compression of the magnetic field is synonymous with compression of the ambient plasma.

⁵In the case of an ideal plasma, Ohm's law takes the form $E + U \times B = 0$.

⁶The McIlwain parameter L is used to index field lines in Earth's dipole geometry: $L \equiv \frac{r}{\sin^2 \theta}$ for colatitude θ and radius r in Earth radii. For example, the $L = 5$ field line passes through the equatorial plane at a geocentric radius of $5 R_E$, then meets the Earth at a colatitude of $\arcsin \sqrt{\frac{1}{5}} \sim 27^\circ$ (equally, a latitude of $\arccos \sqrt{\frac{1}{5}} \sim 63^\circ$).

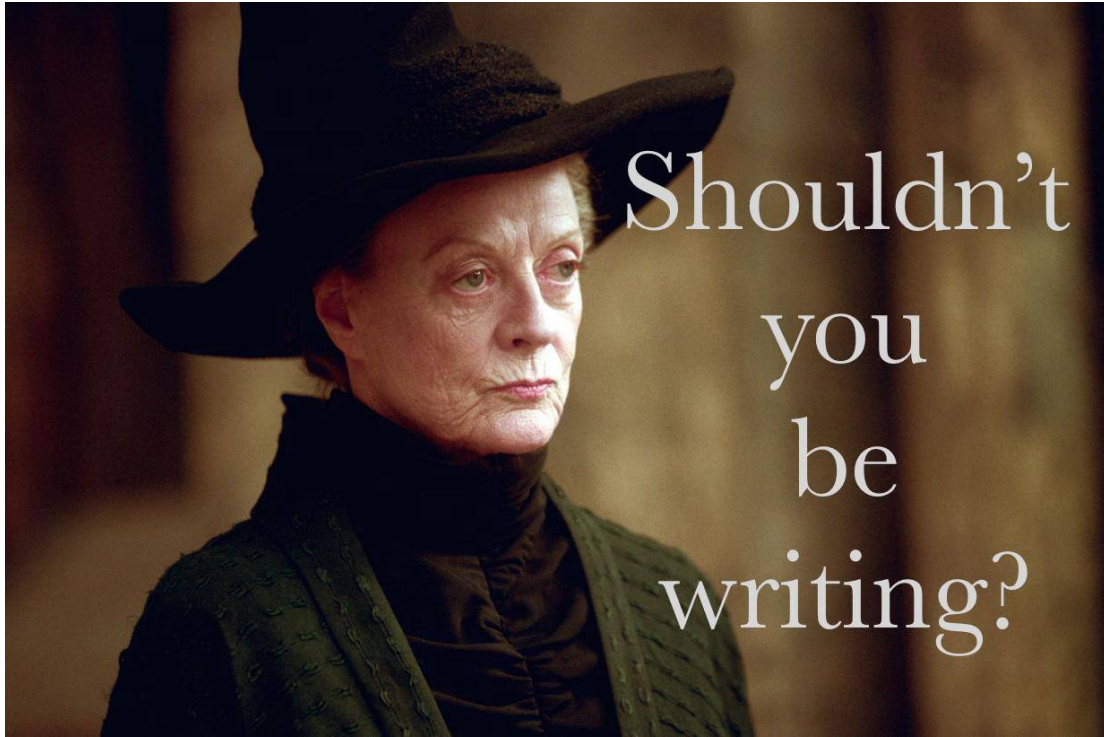


Figure 2.2: TODO: The inner magnetosphere...

- 219 The plasmasphere — a cold (~ 1 eV), dense ($10^2 / \text{cm}^3$ to $10^4 / \text{cm}^3$) torus of corotating
220 plasma — is formed by the outward drift of atmospheric ions along magnetic closed
221 field lines. Its outer boundary, is thought to represent a balance between the corotation
222 electric field (per the rotation of Earth's magnetic dipole) and the convection electric
223 field (associated with the convection of magnetic flux during the Dungey cycle). Particle
224 density drops sharply at the edge of the plasmasphere; the boundary is called the
225 plasmapause. The plasmapause typically falls around $L = 4$, though during prolonged
226 quiet times it can extend to $L = 6$ or larger.
- 227 Energetic particles trapped within the inner magnetosphere are divided into two popu-
228 lations.
- 229 The Van Allen radiation belts are made up of particles with energy above 10^5 eV or
230 so. The inner belt ($L \lesssim 2$) is primarily composed of protons, the decay remnants of

231 neutrons freed from the atmosphere by cosmic rays. The outer belt ($L \gtrsim 4$) is primarily
232 composed of high-energy electrons.

233 Particles with energies of 10^3 eV to 10^5 eV make up the ring current, which extends
234 from $L \sim 3$ to $L \sim 5$. Gradient-curvature drift carries ions and electrons in opposite
235 directions; the net result is a westward current. During quiet times, the ring current
236 causes magnetic a southward magnetic field on the order of 1 nT at Earth's equator⁷.

237 2.3 The Ionosphere

238 Earth's neutral atmosphere is an excellent insulator. Collisions are so frequent that
239 charged particles quickly thermalize and recombine. The breakdown of air molecules
240 into a conductive plasma (as happens during a lightning strike, for example) requires
241 electric fields on the order of 10^9 mV/m.

242 Currents are also suppressed by the magnetosphere. In the absence of collisions, elec-
243 trons and ions drift alongside one another in response to an electric field, creating no
244 net current perpendicular to the magnetic field⁸. Magnetic field lines are (to a good
245 approximation) equipotential contours; electric fields do not form along them to drive
246 parallel currents.

247 The ionosphere is a sweet spot between the two regimes. Collisions are frequent enough
248 to disrupt the drift of ions, but not frequent enough to immobilize the electrons. The
249 result is nonzero Pedersen and Hall conductivity, corresponding to current along the
250 electric field and in the $\underline{B} \times \underline{E}$ direction respectively. Collisions in the ionosphere
251 also give rise to a finite parallel conductivity, allowing for the formation of potential
252 structures along the magnetic field line.

253 **TODO: Field-aligned currents depend on the level of geomagnetic activity... but do**
254 **they ever completely go away?**

⁷For comparison, Earth's dipole field points north at the equator with a magnitude over 10^4 nT.

⁸The so-called E -cross- B drift is associated with a velocity of $\underline{U} = \frac{1}{B^2} \underline{E} \times \underline{B}$, independent of a charged particle's mass or sign.

255 The convection electric field (associated with the Dungey cycle, Section 2.1) drives Ped-
256 ersen currents in the ionosphere. It is these currents that give rise to the strongest mag-
257 netic fields on the ground. Pedersen currents flow downward on the flanks and duskward
258 across the poles. The currents remain divergence-free by connecting to field-aligned cur-
259 rents at the edges of the polar cap. The field-aligned currents, in turn, connect to the
260 magnetopause current, the cross-tail current, and the (partial) ring current.

261 When electron density is low, thermal velocities may be unable to carry enough current
262 to satisfy $\nabla \cdot \underline{J} = 0$. This leads to the formation of potential structures along geomagnetic
263 field lines in the ionosphere. Such structures accelerate particles along magnetic field
264 lines, leading to the precipitation of energetic particles into the atmosphere. As the
265 particles thermalize, they excite atmospheric atoms. The resulting spontaneous emission
266 is often in the visible spectrum, giving rise to the aurora.

267 **TODO:** Particles can also be excited by Alfvén waves... this probably goes in Chapter 3.
268

269 **2.4 Geomagnetic Storms and Substorms**

270 The quiet geomagnetic behavior described above is periodically disturbed by transient
271 solar phenomena such as corotating interaction regions (CIRs) and coronal mass ejec-
272 tions (CMEs). CMEs, as noted in Chapter 1, are bursts of unusually dense solar wind
273 which are ejected from regions of high magnetic activity on the Sun; they are most
274 common at the height of the eleven-year solar cycle. CIRs, on the other hand, occur
275 when a relatively fast region of the solar wind catches up to an earlier and slower-moving
276 pocket of solar wind, resulting in a pair of shockwaves.

277 During a storm, increased solar wind intensity results in enhanced magnetic reconnection
278 on the dayside. As the newly-opened field lines are swept tailward, the convection
279 electric field is strengthened. The plasmasphere — the outer boundary of which is
280 set by a balance between the convection electric field and the (more or less constant)
281 corotation electric field — sheds its outer layers. A large number of energetic particles
282 are also injected into the ring current[68].

283 The strength of the storm is gauged by the size of the magnetic perturbation created
284 by the ring current⁹. A small storm has a magnitude of 50 nT to 100 nT. Large storms
285 may reach 250 nT to 500 nT. The Carrington Event, mentioned in Chapter 1, is thought
286 to have exceeded 1700 nT[96].

287 The main phase of a storm typically lasts for several hours. Storm recovery — the grad-
288 ual return of the storm index to zero — typically lasts several days. The plasmapause
289 refilling occurs on timescales of **TODO: ???**. Geomagnetic storms occur tens of times
290 per year at the height of the solar cycle, and just a few times per year otherwise.

291 Whereas storms are prompted by large solar wind events on the dayside, geomagnetic
292 substorms are primarily a nightside occurrence. As flux accumulates in the tail, mag-
293 netic tension builds in the stretched field lines. A substorm is an impulsive release of
294 that tension.

295 **TODO: Phases of a substorm.** Definition of a substorm comes from [1]. Revised by [69].

296

297 At substorm onset, a burst of reconnection occurs in the tail. A jet of plasma is launched
298 Earthward from the reconnection site (and another is launched tailward, and lost to the
299 solar wind). The Earthward plasma injection injects particles into the ring current.
300 The outer radiation belt is depleted, then repopulated. Energetic particles precipitate
301 into the atmosphere, giving rise to a distinctive **TODO: hour-long** sequence of auroral
302 signatures.

303 Concurrent with substorm onset, impulsive Alfvén waves are observed with periods of
304 a minute or two. The precise ordering of events — whether reconnection causes the
305 waves, or vice versa, or if they share a common cause — remains controversial.

306 Each substorm lasts several hours, including the time it takes for the ring current to
307 return to pre-substorm levels. Several substorms may occur per day during quiet times.
308 During a storm, substorms become far more frequent; by the time one has ended,
309 another may have already begun.

⁹The most commonly used storm index is DST, which is computed hourly using measurements from several ground magnetometers near the equator. The Sym-H index, used in Section 5.3, is computed once per minute.

310 **Chapter 3**

311 **Field Line Resonance**

312 The motion of a charged particle in a dipole field can be described in terms of three
313 fundamental motions. The first is cyclotron motion: a particle orbits around a magnetic
314 field line in accordance with the Lorentz force. The second is bounce motion: while
315 orbiting, the particle moves along the field line like a bead on a wire, back and forth
316 between the northern and southern hemispheres¹. The third is drift motion: as particles
317 orbit and bounce, they also move azimuthally around Earth per the gradient-curvature
318 drift.

319 Characteristic timescales for each of the above motions depend on particle energy. Elec-
320 tron cyclotron motion is on the order of TODO: ... in the ionosphere, and closer to
321 TODO: ... in the tail; ions gyrate slower by three orders of magnitude due to their
322 larger mass. TODO: Bounce... Drift...

323 Wave-particle resonance arises when a particle's periodic motion matches with the fre-
324 quency of a coincident electromagnetic wave[24, 63, 74, 85]. In the particle's rest frame,
325 the wave then appears as a net electric field. This allows a net movement of energy

¹As a particle approaches Earth, it experiences an ever-stronger magnetic field. The particle's perpendicular kinetic energy increases in proportion with the magnetic field in order to conserve its first adiabatic invariant. When the perpendicular kinetic energy can no longer increase — that is, when the parallel kinetic energy is zero — the particle bounces back. (If the parallel kinetic energy is sufficiently large, the particle doesn't bounce; it precipitates into the atmosphere.)

326 between the wave and the particle. The interaction is analogous to a surfer moving
327 along with — and being accelerated by — a wave in the ocean.

328 In the present work, the waves in question are field line resonances (FLRs). An FLR
329 is a standing harmonic on a geomagnetic field line. It can also be envisioned as a
330 superposition of traveling waves, reflecting back and forth between its northern and
331 southern foot points at the conducting ionosphere. These waves travel at the Alfvén
332 speed². The fundamental equations of field line resonance were presented by Dungey in
333 1954[21]; since then, they have remained a topic of active study.

334 So-called ultra low frequency waves — of which FLRs are a subset — are categorized
335 by morphology. Continuous (long-lived) pulsations are termed Pc, while irregular pul-
336 sations are called Pi. Within each are a number of frequency bands; see Table 3.1[45].

Table 3.1: IAGA Magnetic Pulsation Frequency Bands

	Pc1	Pc2	Pc3	Pc4	Pc5	Pi1	Pi2
Period (s)	0.2–5	5–10	10–45	45–150	150–600	1–40	40–150
Frequency (mHz)	200–5000	100–200	22–100	7–22	2–7	25–1000	7–25

337 **TODO:** Boundaries between wave bands are, in practice, not strict. They are sometimes
338 fudged to better match phenomenological boundaries.

339 FLRs fall into the Pc3, Pc4, and Pc5 ranges. The present work focuses specifically
340 on the Pc4 band: waves with periods of a minute or two. Frequencies in the Pc4
341 range typically coincide with Alfvén bounce times³ near the plasmapause: $L \sim 4$ to
342 $L \sim 6$ [3, 17, 25, 56]⁴. In fact, the large radial gradients in the Alfvén speed near the
343 plasmapause act as an effective potential well, trapping FLRs[16, 50, 53, 54, 62, 88].

²The Alfvén speed is given by v_A is given by $v_A^2 \equiv \frac{B^2}{\mu_0 \rho}$, where B is the magnitude of the magnetic field, μ_0 is the magnetic constant, and ρ is the mass density of the ambient plasma. It can vary by several orders of magnitude over the length of a magnetic field line.

³The Alfvén frequency is the inverse of the Alfvén bounce time: $\frac{2\pi}{\omega_A} \equiv \oint \frac{dz}{v_A}$.

⁴Not coincidentally, these are the same L -shells where the Van Allen Probes spend most of their time; see Chapter 8.

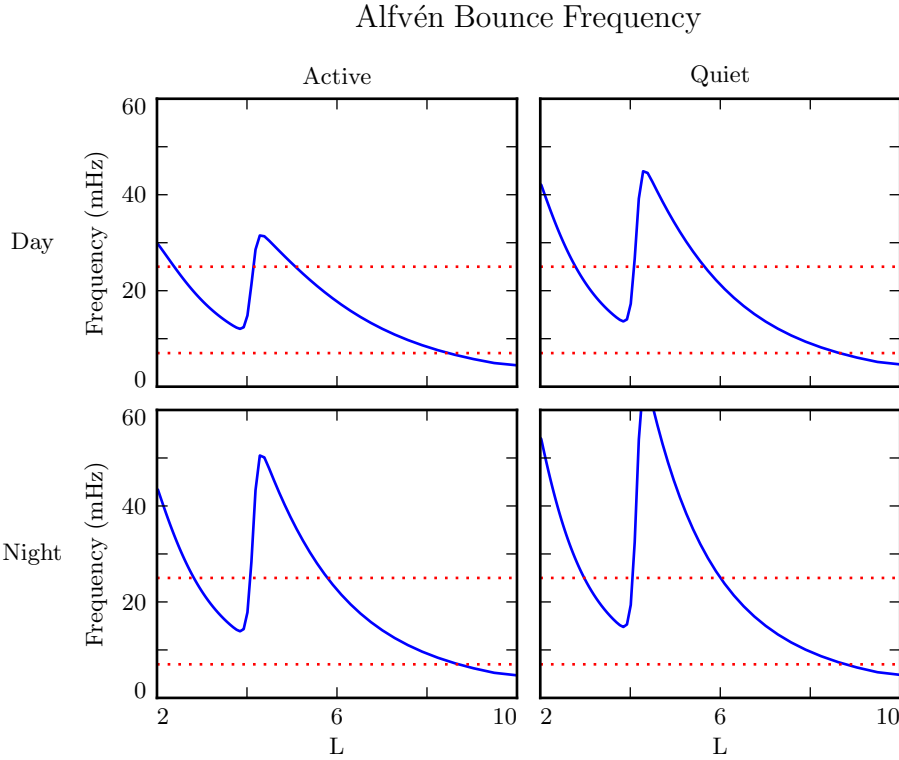


Figure 3.1: The above are bounce frequencies for an Alfvén wave moving back and forth along a geomagnetic field line. Alfvén speeds are computed based on profiles from Kelley[48], as discussed in Section 5.2. Notably, the bounce frequency depends significantly on the position of the plasmasphere, taken here to be at $L = 4$. Dotted lines indicate the Pc4 frequency range: 7 mHz to 25 mHz.

- ³⁴⁴ In addition to being radially localized, FLRs in the Pc4 frequency band (also called Pc4
- ³⁴⁵ pulsations, or just Pc4s) are localized in magnetic local time (MLT⁵). They have also
- ³⁴⁶ been shown to occur preferentially on the dayside, during storms or storm recovery[3,
- ³⁴⁷ 17, 25, 52, 56, 97].
- ³⁴⁸ In the inner magnetosphere, the Alfvén frequency — and thus the frequency of FLRs
- ³⁴⁹ — often coincides with integer or half-integer⁶ multiples of particle drift frequencies[18].

⁵Noon points toward the Sun and midnight away from it, with 06:00 and 18:00 at the respective dawn and dusk flanks.

⁶See Section 3.1.

350 The resulting wave-particle interactions can give rise to significant energization and
351 radial diffusion of the particles. In some cases, the waves also include an electric field
352 parallel to the background magnetic field, contributing to the precipitation of energetic
353 particles into the neutral atmosphere[32, 33, 93, 103].

354 The present chapter introduces the structural characteristics of FLRs, how those charac-
355 teristics affect wave behavior, and several unresolved questions related to that behavior.

356 **TODO:** The polarization of long-period Alfven waves is rotated by $\sim 90^\circ$ when passing
357 through the ionosphere[41]. A wave that is azimuthally polarized in space is polarized
358 north-south on the ground, and vice versa. It has been noted specifically that Pgs
359 exhibit east-west polarized ground signatures[92].

360 **TODO:** Other planets[31]? Seems exciting but maybe not relevant.

361 3.1 Harmonic Structure

362 Wave structure along a geomagnetic field line is indicated by harmonic number. The
363 first (or fundamental) harmonic has a wavelength twice as long as the field line. It
364 exhibits an antinode in the perpendicular electric field at the equator, along with a
365 node in the perpendicular magnetic field. The second harmonic is a single wavelength
366 along the field line. Its perpendicular magnetic perturbation has an antinode at the
367 equator, while its perpendicular electric field has a node. Figure 3.2 shows a qualitative
368 sketch of each: a series of snapshots in time, in the rest frame of the wave. Perpendicular
369 electric and magnetic field perturbations are shown in blue and red respectively.

370 A first-harmonic FLR that is periodic or localized in the azimuthal direction is conducive
371 to drift-resonant wave-particle interactions[18, 75]. The particle is like a child on a swing:
372 whenever the path of the particle (or child) gets close to the wave (parent), it gets a
373 push, and always in the same direction. The wave fields spend half its time pointing
374 the other direction, just as the parent must shift their weight backward to get ready for
375 the next push, but at that point the particle (child) is far away.

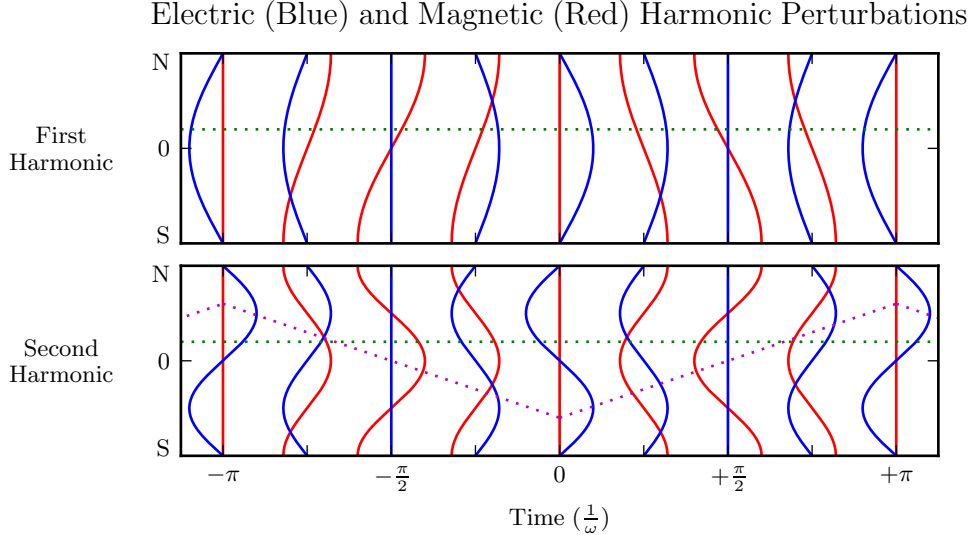


Figure 3.2: The first (or fundamental) harmonic has an antinode in its perpendicular electric field (blue) at the equator, along with a node in its perpendicular magnetic field perturbation (red). A single satellite can identify the first harmonic by the relative phase of the electric and magnetic field perturbations: an observer north of the equator (green) will see the magnetic field perturbation lead the electric field by 90° . The second harmonic is the opposite: it has an electric field node at the equator, and an observer north of the equator will see the magnetic field perturbation lag the electric field by 90° . The purple line sketches the path of a particle in drift-bounce resonance; in the particle’s rest frame, the electric field is always to the right. **TODO:** Actually, toroidal waves are flipped — Faraday’s law gives $\frac{\partial}{\partial t} B_x \sim \frac{\partial}{\partial z} E_y$ but $\frac{\partial}{\partial t} B_y \sim -\frac{\partial}{\partial z} E_x$.

376 Second-harmonic FLRs interact with particles through the drift-bounce resonance, which
 377 is slightly more complicated. As the particle drifts azimuthally, it also zig-zags north-
 378 south. The combination of those two periodic motions must align with the phase of
 379 the wave electric field. An example path is shown by the purple line in Figure 3.2: the
 380 particle experiences a rightward electric field throughout the wave’s oscillation.

The drift and drift-bounce resonance conditions are written, respectively[89]:

$$\omega - m\omega_D = 0 \quad \text{and} \quad \omega - m\omega_D = \omega_B \quad (3.1)$$

381 Where ω is the frequency of the wave, ω_D and ω_B are the particle's drift and bounce
382 frequencies respectively, and m is the wave's azimuthal modenumber, as discussed in
383 Section 3.2.

384 In principle, the first and second harmonics can be distinguished by their frequencies,
385 even from a single-point observation[15, 34]. In practice, however, this is not a reliable
386 approach[90]. There are significant uncertainties surrounding the number density profile
387 — and thus the Alfvén speed profile — along a geomagnetic field line.

388 Harmonic structure can also be deduced by noting the phase offset between the wave
389 magnetic field and its electric field (or the plasma velocity)[17, 92]. In Figure 3.2,
390 the green line indicates an observer just north of the magnetic equator. For the first
391 harmonic, the observer sees the electric field waveform lead the magnetic field by a
392 phase of 90° ; for the second harmonic, the electric field waveform lags by 90° . (South
393 of the equator, the signs are reversed.) Notably, this approach has only become viable
394 with the advent of satellites carrying both electric and magnetic field instrumentation,
395 such as THEMIS in 2007[4] and the Van Allen Probes⁷ in 2012[86].

396 Strictly speaking, the the phase offset of the electric and magnetic fields does not provide
397 the harmonic number — only its parity. It's reasonably safe to assume that an even mode
398 is the second harmonic; the second harmonic is by far the most commonly observed[44,
399 83, 91], due in part to its excitement by the antisymmetric balloon instability[9, 11,
400 13, 85]. However, the distinction between the first and third harmonics is not always
401 clear; this issue is discussed further in Chapter 8. Higher harmonics than that are not
402 expected in the Pc4 frequency band.

403 **TODO:** Second-harmonic FLRs are unlikely to cause ground signatures[92].

404 **TODO:** Dai found a nice event[18] that was unambiguously determined to be a fundamental-
405 mode Pc4 in drift-resonant interaction with $\sim 10^5$ eV ions. Consistent with [94]. Other
406 observations of odd harmonics: [104, 26].

⁷The Van Allen Probes were previously called RBSP, for Radiation Belt Storm Probes.

407 **3.2 Azimuthal Modenumber**

408 The wavelength of an FLR in the azimuthal direction is indicated by its azimuthal
409 wavelength. A wave with modenumber m has an azimuthal wavelength that spans $\frac{24}{m}$
410 hours in MLT.



Figure 3.3: TODO: Large and small azimuthal modenumbers.

411 Waves with small azimuthal modenumbers ($0 < m < 10$) are typically driven by broad-
412 band energy sources at the magnetosphere's boundary, such as variations in the so-
413 lar wind pressure[19, 38, 49, 107, 108], sporadic magnetic reconnection[42], or Kelvin-
414 Helmholtz waves on the magnetopause[10, 57, 84]. In the low- m regime, the shear and
415 compressional Alfvén waves are coupled, which allows energy to move across field lines
416 until the driving frequency lines up with the local Alfvén frequency[59]. Because of their
417 broadband energy source, low- m FLRs often have a mishmash of frequencies present in
418 their spectra[17].

- 419 When the azimuthal modenumber is large (or, equally, when the azimuthal wavelength
 420 is small), the shear and compressional Alfvén waves are decoupled[15, 78]⁸. As a result,
 421 FLRs must be driven from within the magnetosphere. Proposed energy sources include
 422 phase space gradients near the plasmapause[18], particularly as the plasmasphere refills
 423 after a storm or substorm[25, 55].
- 424 The ionosphere is known to attenuate waves with small spatial extent in the perpendicular
 425 direction[43, 102, 106]. As a result, FLRs may create no signature on the ground if
 426 their azimuthal modenumber is large. For example, a recent paper by Takahashi shows
 427 a strong (2 nT at $L \sim 10$), clear resonance with $|m| \gtrsim 70$ and no corresponding ground
 428 signature[90].

Southwood[85] and Glassmeier[29] show that a low frequency wave passing through the ionosphere on its way to Earth will be attenuated per

$$\frac{B_E}{B_I} = \frac{\Sigma_H}{\Sigma_P} \exp\left(-m \frac{R_I - R_E}{R_E \sin \theta}\right) \quad (3.2)$$

- 429 Where B_E and B_I are the magnetic field strengths at R_E (Earth's surface, 6783 km
 430 geocentric) and R_I (the ionosphere, \sim 6900 km geocentric) respectively. The integrated
 431 ionospheric Pedersen and Hall conductivities, Σ_P and Σ_H , are typically within a factor
 432 of two of one another. Field lines near the plasmapause can be traced to Earth at
 433 $\sin \theta \sim 0.4$. That is, by the time it reaches the ground, the magnetic field from an FLR
 434 with $m = 10$ is weaker by a factor of two; at $m = 100$, the factor is closer to 100.

435 3.3 Poloidal and Toroidal Polarizations

- 436 Based on polarization, each FLR can be classified as either poloidal or toroidal. The
 437 poloidal mode is a field line displacement in the meridional plane, as shown in Figure 3.4,
 438 with an accompanying electric field in the azimuthal direction. The toroidal mode's
 439 magnetic displacement is azimuthal, per Figure 3.5; the associated electric field is in the
 440 meridional plane.

⁸Equally, the strength of a wave's parallel component hint at its modenumber, a point which is revisited in Chapter 8.

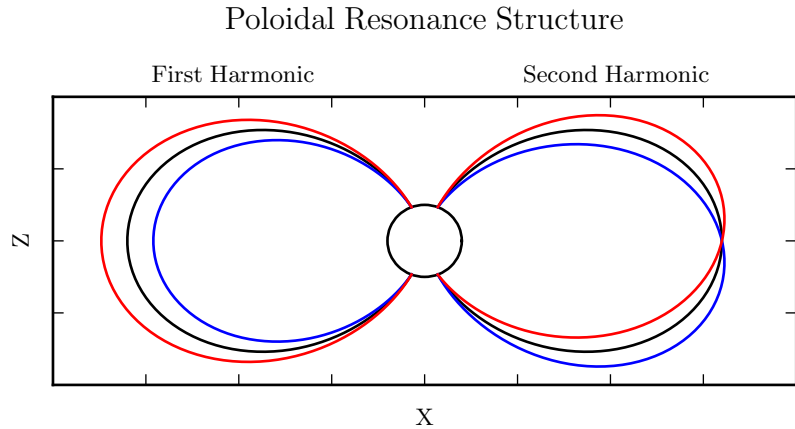


Figure 3.4: The poloidal resonance is a magnetic field in the meridional plane. The displacement is radial near the equator, and can be accompanied by enhancement in the parallel magnetic field near the ionosphere. The first harmonic is shown on the left, and the second harmonic on the right. Lines are colored red and blue only to contrast with the unperturbed black field line.

- 441 Both poloidal and toroidal waves are noted for their ability to contribute to the energiza-
- 442 tion and radial diffusion of trapped particles. The poloidal mode interacts more strongly,
- 443 since its electric field is aligned with the trapped particles' drift motion. Poloidally-
- 444 polarized waves are also more prone to creating magnetic signatures on the ground, due
- 445 to ducting in the ionosphere[27, 36].

- 446 Toroidal modes have been shown to far outnumber poloidal modes[3]. Perhaps not
- 447 coincidentally, poloidally-polarized waves rotate asymptotically to the toroidal mode[64,
- 448 65, 78]. Poloidal waves with low azimuthal modenumber — such as those driven by
- 449 broadband sources at the magnetopause — rotate on timescales comparable to their
- 450 oscillation periods.

- 451 TODO: Fishbone instability[12, 67]. Like the poloidal mode, but for lab plasmas.

- 452 TODO: Poloidal and toroidal modes are coupled by the ionospheric Hall conductivity[47].
- 453 The Hall conductivity also increases the “ringtime” of these resonances, allowing them

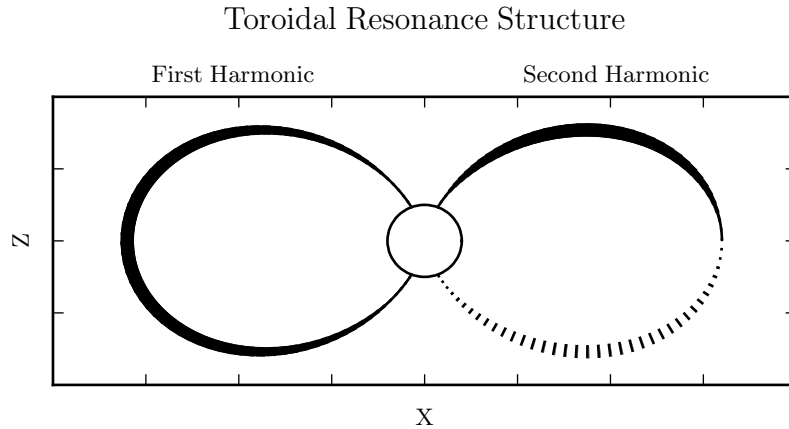


Figure 3.5: A toroidally-polarized FLR has a magnetic perturbation in the azimuthal direction, as shown. Bold lines are taken to be above the page, and dotted lines below the page, with the displacement indicated by the line's width. The first harmonic — where the entire field line oscillates in and out of the page — is shown on the left. The second harmonic is on the right, with northern and southern halves perturbed in opposite directions.

454 to oscillate through the inductive process rather than be dissipated as Joule heating[100].

455

456 TODO: Toroidal modes show a clear frequency dependence with L . Poloidal modes less
457 so. Citation...?

458 3.4 Giant Pulsations

459 The study of geomagnetic pulsations long predates satellites, sounding rockets, or even
460 the word “magnetohydrodynamics”⁹. Large, regular oscillations in the magnetic field
461 were noted as early as 1901[5]. Eventually, the term “giant pulsation,” or Pg, arose to
462 describe such pulsations.

⁹The term was first used by Alfvén in the 1940s[2].

463 On the ground, Pgs are notable for their strikingly sinusoidal waveforms, their eastward
464 drifts, and their specific occurrence pattern: Pgs are typically seen pre-dawn, at latitudes
465 of 60° to 70° . Pgs generally fall into the Pc4 frequency band¹⁰. Their harmonic structure
466 was a source of controversy for decades, but recent multisatellite observations seem to be
467 in agreement that they are odd harmonics, probably fundamental[30, 40, 51, 52, 89, 92].
468 They are poloidally polarized, with modenumbers $10 \lesssim m \lesssim 40$ [28, 40, 75, 81, 92].

469 Whereas FLRs are waves in space which may produce ground signatures, “giant pul-
470 sation” refers to the ground signature specifically¹¹. That is, Takahashi’s satellite ob-
471 servation of a sinusoidal, morningside, high- m , fundamental poloidal resonance was not
472 classified as a Pg because it did not produce a signal on the ground[90].

473 **TODO: Pgs are localized to within 2° to 5° in latitude[70, 89, 98].**

474 Due to their remarkably clear waveforms, Pgs are typically found by “visual inspection
475 of magnetometer data”[70]. Over the course of the past century, a number of multi-year
476 (sometimes multi-decade[7]) surveys have totaled nearly one thousand Pg events. On
477 average, a ground magnetometer near 66° magnetic latitude observes ~ 10 Pg events per
478 year[7, 39, 80, 87]. Observations are not distributed uniformly; rather, giant pulsations
479 become more common near the equinox and during times of low solar activity.

480 Unlike Pc4 pulsations in general, Pgs show no particular correlation with storm phase[70].
481 However, they do often occur as the magnetosphere recovers from a substorm[70, 81].

482 **3.5 Motivations for the Present Work**

483 A great deal has been learned — and continues to be learned — through observations of
484 field line resonance. However, the cost-to-benefit ratio is climbing. As summarized in the
485 sections above, FLR behavior depends significantly on harmonic structure, azimuthal
486 modenumber, and polarization — not to mention frequency, spectral width, and so

¹⁰The Pc4 range is periods of 45 s to 140 s, while Pgs are often said to range from 60 s to 200 s[7].

¹¹Historically, the wave designations shown in Table 3.1 all referred to ground phenomena. Over time,
they have come to describe satellite observations as well, including those without corresponding sig-
natures on the ground.

487 on. With each degree of freedom comes the necessity for an additional simultaneous
488 observation.

489 Similarly, as FLRs have been shown to depend on ever-more-specific magnetospheric
490 conditions, analytical techniques have fallen out of favor. The height-resolved iono-
491 sphere, the multidimensional Alfvén speed profile, and the inconvenient geometry com-
492 bine to create a problem beyond the reasonable purview of pencil and paper.

493 That is, the topic of field line resonance is ripe for numerical modeling.

494 Past models of the magnetosphere have been ill-suited for the consideration of FLRs.
495 Reasons include overly-simplified treatment of the ionospheric boundary, no consider-
496 ation of the plasmapause, limited range in m , and the inability to compute ground
497 signatures. Chapter 5 presents a model which addresses these issues, allowing the com-
498 putation of field line resonance with unparalleled attention to realism.

499 The model allows a bird’s-eye view of the structure and evolution of FLRs. As such,
500 not only can several open questions be addressed, but their answers serve to unify a
501 number of seemingly-disparate properties described in the sections above.

502 The rotation of poloidally-polarized waves to the toroidal mode is investigated. Par-
503 ticular attention is paid to the importance of azimuthal modenumber and ionospheric
504 conductivity. The interplay between said rotation and the transport of energy across
505 field lines — which also depends on azimuthal modenumber — is considered as well.

506 By their nature, drifting particles have the potential to spur wave-particle interactions
507 at all MLT. However, Pc4 observations are strongly peaked on the dayside. In a 2015
508 paper, Dai notes, “It is not clear why noncompressional [high- m] Pc4 poloidal waves,
509 which are presumably driven by instability within the magnetosphere, preferentially
510 occur on the dayside”[17]. Motoba, later that year, echoes, “It is unclear whether other
511 generation mechanisms of fundamental standing waves ... can explain the localization
512 of Pgs in local time”[70]. This, too, is considered numerically: to what degree is field
513 line resonance affected by the (day-night asymmetric) conditions of the ionosphere?

514 **TODO:** Transition... With the above in mind, what data would be super helpful?

515 It's been shown that a ground magnetometer 66° north of the magnetic equator observes
516 \sim 10 Pg events per year. It's also been shown that poloidal Pc4s are rare compared to
517 toroidal ones, and that most poloidal Pc4s are even harmonics. However, little attention
518 has been paid to how these rates line up with one another. Given the relative occurrence
519 rate of poloidal and toroidal waves, of odd and even harmonics, and of diffuse and sharp
520 spectral peaks, just how unusual are giant pulsations?

521 Chapter 4

522 Waves in Cold Resistive Plasma

523 Before delving into the implementation of the numerical model, it's instructive to consider the fundamental equations of waves in a cold, resistive plasma.

The evolution of electric and magnetic fields is governed by Ampère's law and Faraday's law. Notably, the present work takes the linearized versions of Maxwell's equations; the vectors \underline{E} and \underline{B} indicate perturbations above the zeroth-order magnetic field.

$$\underline{\epsilon} \cdot \frac{\partial}{\partial t} \underline{E} = \frac{1}{\mu_0} \nabla \times \underline{B} - \underline{J} \quad \frac{\partial}{\partial t} \underline{B} = -\nabla \times \underline{E} \quad (4.1)$$

Current follows Ohm's law. For currents perpendicular to the background magnetic field, Kirchhoff's formulation is sufficient. Conductivity is much higher along the magnetic field lines¹, so it's appropriate to also include the electron inertial term².

$$0 = \underline{\sigma}_{\perp} \cdot \underline{E}_{\perp} - \underline{J}_{\perp} \quad \frac{1}{\nu} \frac{\partial}{\partial t} J_z = \sigma_0 E_z - J_z \quad (4.2)$$

¹The dipole coordinate system is defined rigorously in Section 5.1; at present, it's sufficient to take \hat{z} parallel to the zeroth-order magnetic field, and \hat{x} and \hat{y} perpendicular to \hat{z} (and to each other).

²Electron inertial effects are not included in the model described in Chapter 5, or in the results in Chapter 7; however, their implementation and impact are explored in Chapter 6.

Derivatives in Equations (4.1) and (4.2) can be evaluated by performing a Fourier transform. They can then be combined, eliminating the magnetic field and current terms.

$$\begin{aligned} 0 &= \underline{\underline{E}}_{\perp} + \frac{v_A^2}{\omega^2} (\underline{k} \times \underline{k} \times \underline{E})_{\perp} + \frac{i}{\epsilon_{\perp}\omega} \underline{\sigma}_{\perp} \cdot \underline{E}_{\perp} \\ 0 &= E_z + \frac{c^2}{\omega^2} (\underline{k} \times \underline{k} \times \underline{E})_z + \frac{i\omega_P^2}{\omega(\nu - i\omega)} E_z \end{aligned} \quad (4.3)$$

The speed of light, Alfvén speed (including the displacement current correction), plasma frequency, and parallel conductivity are defined in the usual way:

$$c^2 \equiv \frac{1}{\mu_0\epsilon_0} \quad v_A^2 \equiv \frac{1}{\mu_0\epsilon_{\perp}} \quad \omega_P^2 \equiv \frac{ne^2}{m_e\epsilon_0} \quad \sigma_0 \equiv \frac{ne^2}{m_e\nu} \quad (4.4)$$

Using the vector identity $\underline{k} \times \underline{k} \times \underline{E} = \underline{k} \underline{k} \cdot \underline{E} - k^2 \underline{E}$, Equation (4.3) can be reassembled into a single expression,

$$0 = \left(\underline{\underline{\mathbb{I}}} + \frac{1}{\omega^2} \underline{\underline{V}}^2 \cdot \underline{k} \underline{k} - \frac{k^2}{\omega^2} \underline{\underline{V}}^2 + \frac{i}{\omega} \underline{\underline{\Omega}} \right) \cdot \underline{E} \quad (4.5)$$

Where $\underline{\underline{\mathbb{I}}}$ is the identity tensor and in x - y - z coordinates,

$$\underline{\underline{V}}^2 \equiv \begin{bmatrix} v_A^2 & 0 & 0 \\ 0 & v_A^2 & 0 \\ 0 & 0 & c^2 \end{bmatrix} \quad \text{and} \quad \underline{\underline{\Omega}} \equiv \begin{bmatrix} \frac{\sigma_P}{\epsilon_{\perp}} & \frac{-\sigma_H}{\epsilon_{\perp}} & 0 \\ \frac{\sigma_H}{\epsilon_{\perp}} & \frac{\sigma_P}{\epsilon_{\perp}} & 0 \\ 0 & 0 & \frac{\omega_P^2}{(\nu - i\omega)} \end{bmatrix} \quad (4.6)$$

525 In Equation (4.5), the expression in parentheses is the dispersion tensor. Nontrivial
526 solutions exist only when its determinant is zero. This gives rise to a seventh-order
527 polynomial in ω , so rather than a direct solution it's necessary to consider limits of
528 specific interest.

529 Without loss of generality, the wave vector \underline{k} may be taken to lie in the x - z plane — that
530 is, with $k_y = 0$. The distinction between the two perpendicular directions is discussed
531 in Section 4.4.

532 **4.1 Guided Propagation**

533 The wave vector of a field line resonance aligns closely to the background magnetic
534 field. By supposing that the two align exactly (that is, taking $k_x = 0$), the parallel and
535 perpendicular components of the dispersion relation are decoupled.

The parallel-polarized component — that is, the solution when $E_x = E_y = 0$ — is quadratic, and thus can be solved directly.

$$0 = \omega^2 + i\nu\omega - \omega_P^2 \quad \text{so} \quad \omega = -\frac{i\nu}{2} \pm \sqrt{\omega_P^2 - \frac{\nu^2}{4}} \quad (4.7)$$

536 It bears noting that the plasma frequency is large — not just compared to Pc4 frequencies,
537 but even compared to the collision frequencies in the ionosphere³.

Expanding Equation (4.7) with respect to large ω_P , the dispersion relation becomes

$$\omega^2 = \omega_P^2 \pm i\nu\omega_P + \dots \quad (4.8)$$

538 Equation (4.8) can hardly be called a wave, as it does not depend on the wave vector
539 k . Rather, it is the plasma oscillation⁴: electrons vibrating in response to a charge
540 separation along the background magnetic field.

541 The plasma oscillation is not specifically relevant to the study of field line resonance.
542 The two phenomena are separated by six orders of magnitude in frequency. The topic
543 is revisited in Chapter 6 insomuch as it is inseparable from the electron inertial effects
544 in Ohm's law.

³The collision frequency may match or exceed the plasma frequency for a thin slice at the bottom of the ionosphere, where the density of neutral atoms is large; however, it falls off quickly. Above an altitude of 200 km, conservatively[73], the plasma frequency exceeds the collision frequency by an order of magnitude or more.

⁴The plasma oscillation is also called the Langmuir wave, after Irving Langmuir.

The perpendicular ($E_z = 0$) components of the dispersion relation give an expression quartic in ω .

$$0 = \omega^4 + 2i\frac{\sigma_P}{\epsilon_\perp}\omega^3 - \left(2k_z^2v_A^2 + \frac{\sigma_P^2 + \sigma_H^2}{\epsilon_\perp^2}\right)\omega^2 - 2ik_z^2v_A^2\frac{\sigma_P}{\epsilon_\perp}\omega + k_z^4v_A^4 \quad (4.9)$$

Like the parallel-polarized component above, Equation (4.9) can be solved directly. Noting that \pm and \oplus are independent,

$$\omega = \left(\frac{\pm\sigma_H - i\sigma_P}{2\epsilon_\perp}\right) \oplus \sqrt{k_z^2v_A^2 + \left(\frac{\pm\sigma_H - i\sigma_P}{2\epsilon_\perp}\right)^2} \quad (4.10)$$

Also like the parallel-polarized component, the exact solution is less useful than its Taylor expansion. The Pedersen and Hall conductivities are large near the ionospheric boundary, but fall off quickly; for the vast majority of the field line, the ratios $\frac{\sigma_P}{\epsilon_\perp}$ and $\frac{\sigma_H}{\epsilon_\perp}$ are small compared to field line resonance frequencies. Expanding with respect to small conductivity gives

$$\omega^2 = k_z^2v_A^2 \oplus k_zv_A\frac{\sigma_H \pm i\sigma_P}{\epsilon_\perp} + \dots \quad (4.11)$$

545 This is the shear Alfvén wave, with a shift to its frequency due to the conductivity of
 546 the ionosphere. It travels along the background magnetic field like a bead on a string,
 547 with electric and magnetic field perturbations perpendicular to the magnetic field line
 548 (and to one another).

549 4.2 Compressional Propagation

550 The partner to guided motion is compressional motion; in order for energy to move
 551 across field lines, the wave vector must have a component perpendicular to \hat{z} . If the
 552 wave vector is completely perpendicular to the magnetic field line ($k_z = 0$), the parallel
 553 and perpendicular components of the dispersion relation decouple, as in Section 4.1.

The parallel-polarized ($E_x = E_y = 0$) component of the dispersion relation is

$$0 = \omega^3 + i\nu\omega^2 - (k_x^2 c^2 + \omega_P^2) \omega - ik_x^2 c^2 \nu \quad (4.12)$$

Equation (4.12) can be solved directly, though its solution (as a cubic) is far too long to be useful. Expanding with respect to the large plasma frequency, gives

$$\omega^2 = k^2 c^2 + \omega_P^2 - i\nu\omega_P + \dots \quad (4.13)$$

554 This is the O mode, a compressional wave with an electric field perturbation along
555 the background magnetic field. Like the plasma oscillation discussed in Section 4.1, its
556 frequency is very large compared to that of a field line resonance.

The perpendicular-polarized ($E_z = 0$) component of the compressional dispersion relation is also cubic.

$$0 = \omega^3 + 2i\frac{\sigma_P}{\epsilon_\perp}\omega^2 - \left(2k_x^2 v_A^2 + \frac{\sigma_P^2 + \sigma_H^2}{\epsilon_\perp^2}\right) \omega - ik_x^2 v_A^2 \frac{\sigma_P}{\epsilon_\perp} \quad (4.14)$$

A wave moving across magnetic field lines near the ionospheric boundary will encounter large $\frac{\sigma_P}{\epsilon_\perp}$ and $\frac{\sigma_H}{\epsilon_\perp}$, while at moderate to high altitudes those ratios will be small. Solving Equation (4.14) in those two limits respectively gives:

$$\omega^2 = k_x^2 v_A^2 \pm ik_x v_A \frac{\sigma_P}{\epsilon_\perp} + \dots \quad \text{and} \quad \omega^2 = k_x^2 v_A^2 + \left(\frac{\sigma_H \pm i\sigma_P}{\epsilon_\perp}\right)^2 + \dots \quad (4.15)$$

557 In both limits, Equation (4.15) describes a compressional Alfvén wave. The magnetic
558 field perturbation is along the background magnetic field — indicating compression of
559 the frozen-in plasma — while the electric field perturbation is perpendicular to both
560 the magnetic field and the wave vector.

561 **TODO: Double check terminology.** Jesse's dissertation disagrees with Bob's notes.

562 4.3 High Altitude Limit

563 In the limit of large radial distance, it's reasonable to take the collision frequency to
 564 zero; doing so also neglects the Pedersen and Hall conductivities.

Whereas in Sections 4.1 and 4.2 it was the parallel-polarized component of the dispersion relation that factored out from the other two, the high altitude limit decouples the component polarized out of the x - z plane. The y -polarized dispersion ($E_x = E_z = 0$) is simply:

$$\omega^2 = k^2 v_A^2 \quad (4.16)$$

565 Equation (4.16) describes an Alfvén wave with an arbitrary angle of propagation. De-
 566 pending on the angle between the wave vector and the background magnetic field, it
 567 could be guided, compressional, or somewhere in between. Regardless of propagation
 568 angle, the electric field perturbation is perpendicular to both the direction of propaga-
 569 tion and the magnetic field perturbation.

The other two components (from $E_y = 0$) of the high altitude dispersion tensor give an expression quadratic in ω^2 :

$$0 = \omega^4 - (k_x^2 c^2 + k_z^2 v_A^2 + \omega_P^2) \omega^2 + k_z^2 v_A^2 \omega_P^2 \quad (4.17)$$

Which can be solved for

$$\omega^2 = \frac{1}{2} (k_x^2 c^2 + k_z^2 v_A^2 + \omega_P^2) \pm \sqrt{\frac{1}{4} (k_x^2 c^2 + k_z^2 v_A^2 + \omega_P^2)^2 - k_z^2 v_A^2 \omega_P^2} \quad (4.18)$$

Noting again that ω_P is very large, the two roots can be expanded to

$$\omega^2 = k_z^2 v_A^2 \left(1 - \frac{k_x^2 c^2 + k_z^2 v_A^2}{\omega_P^2} \right) + \dots \quad \text{and} \quad \omega^2 = k_x^2 c^2 + k_z^2 v_A^2 + \omega_P^2 + \dots \quad (4.19)$$

570 The first is a shear Alfvén wave, as in Equation (4.11). The second oscillates faster than
 571 the plasma frequency; like the plasma oscillation in Equation (4.8) and the O mode in
 572 Equation (4.13), it's far outside the Pc4 frequency range.

573 4.4 Implications to the Present Work

574 The present section's findings carry three significant implications for the present work.
 575 First — with the exception of the plasma oscillation and similar modes, which are
 576 revisited in Chapter 6 — waves propagate at the Alfvén speed. This, in combination
 577 with the grid configuration, will constrain the time step that can be used to model them
 578 numerically. The time step must be sufficiently small that information traveling at the
 579 Alfvén speed cannot “skip over” entire grid cells⁵.

Second, the results of the present section allow an estimate of the magnitude of parallel electric field that might be expected from a field line resonance compared to its perpendicular electric field. Between the full dispersion tensor form in Equation (4.5) and the Alfvén wave described by Equation (4.19),

$$\left| \frac{E_z}{E_x} \right| = \frac{k_x k_z c^2}{\omega^2 - k_x^2 c^2 - \omega_P^2} \sim \frac{k^2 c^2}{\omega_P^2} \quad (4.20)$$

580 In essence, the relative magnitudes of the parallel and perpendicular electric fields should
 581 be in proportion to the square of the relative magnitudes of the electron inertial length
 582 (1 km to 100 km) and the wavelength ($\sim 10^5$ km). That is, parallel electric fields should
 583 be smaller than the perpendicular electric fields by six or more orders of magnitude.

584 Finally, the dispersion relations shown above indicate how the behavior of a field line
 585 resonance should behave as the azimuthal modenumber becomes large.

586 Whereas the shear Alfvén wave's dispersion relation depends only on the parallel com-
 587 ponent of the wave vector, the compressional Alfvén wave depends on its magnitude:
 588 $\omega^2 = k^2 v_A^2$. If the frequency is smaller than $k v_A$, the wave will become evanescent. The

⁵As is the convention, the time step is scaled down from the smallest Alfvén zone crossing time by a Courant factor, typically 0.1, meaning that it takes at least ten time steps to cross a grid cell.

589 wave vector's magnitude can be no smaller than its smallest component, however, and
 590 the azimuthal component scales with the azimuthal modenumber: $k_y \sim \frac{m}{2\pi r}$.

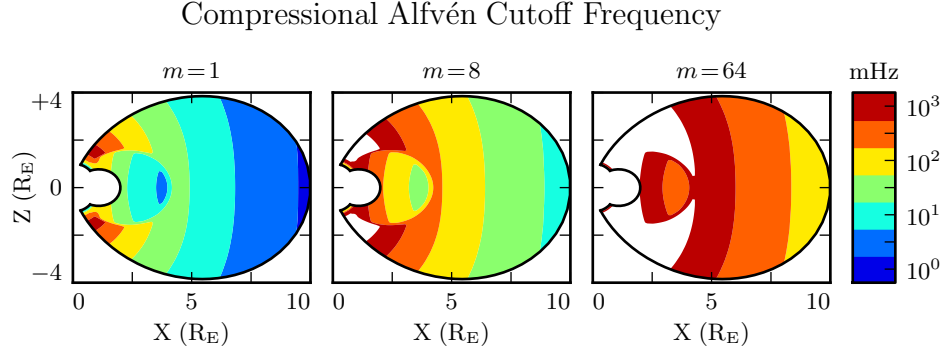


Figure 4.1: Taking $k_y \sim \frac{m}{2\pi r}$ as a lower bound for the magnitude of the wave vector, the above figure demonstrates the lowest frequency at which compressional Alfvén waves may propagate as a function of position and m . Regions shown in white are off the color scale — they have a lower bound on the order of 10^4 mHz or more. The above Alfvén frequency profile is from Kelley[48], for quiet dayside conditions, as discussed in Section 5.2.

591 This imposes a frequency cutoff on compressional Alfvén waves which scales with the
 592 azimuthal modenumber, as shown in Figure 4.1. At small values of m , most of the mag-
 593 netosphere is conducive to compressional Alfvén waves in the Pc4 frequency range. As
 594 m increases, and the wave vector with it, the inner magnetosphere becomes increasingly
 595 inaccessible to them.

596 **Chapter 5**

597 **“Tuna Half” Dimensional Model**

598 The present section describes the implementation of Tuna, a new two and a half dimensional
599 Alfvén wave code based largely on work by Lysak[58, 61].

600 The half-integer dimensionality refers to the fact that Tuna’s spatial grid resolves a
601 two-dimensional slice of the magnetosphere, but that electric and magnetic fields —
602 as well as their curls — are three-dimensional vectors. This apparent contradiction is
603 reconciled by the use of a fixed azimuthal modenumber, m . Electric and magnetic fields
604 are taken to be complex-valued, varying azimuthally per $\exp(im\phi)$; derivatives with
605 respect to ϕ are then replaced by a factor of im .

606 Unlike a fully three-dimensional code, Tuna cannot resolve the evolution of wave structures
607 in the azimuthal direction. Furthermore, the model does not allow coupling between
608 the dayside and nightside magnetospheres. What Tuna does offer is efficiency.
609 The model’s economical geometry allows it to include a realistic Earthward boundary:
610 grid spacing on the order of 10 km, a height-resolved ionospheric conductivity tensor,
611 and even the computation of magnetic field signatures at the ground. Such features are
612 computationally infeasible for a large global code.

613 Tuna was developed with field line resonance in mind. As discussed in Chapter 3,
614 such waves are azimuthally localized, minimizing the importance of Tuna’s missing half
615 dimension. Moreover, because field line resonances are known to be affected by both

616 the ionosphere and the plasmasphere, a faithful treatment of the inner magnetosphere
617 is a crucial part of studying them numerically.

618 Perhaps the most exciting feature of Tuna is its novel driving mechanism: ring current
619 perturbation. Codes similar to Tuna have traditionally been driven using compressional
620 pulses at the outer boundary[58, 61, 100, 101]. This has precluded the investigation of
621 waves with large azimuthal modenumber — such as giant pulsations — which are guided,
622 and thus must be driven from within the magnetosphere.

623 TODO: The dipole geometry isn't super new, but it's not widely used. The height-
624 resolved ionosphere is new and exciting! Ground signatures are new and exciting!

625 TODO: The support software — the driver and the plotter — are also significant. Do
626 they get mentioned here? Does the Git repository where the code can be accessed get
627 mentioned here?

628 5.1 Coordinate System

Field line resonance has traditionally been modeled by straightening the field lines into a rectangular configuration[21, 64], by unrolling the azimuthal coordinate into a cylindrical coordinate system[78], or through the use of dipole coordinates[77]¹:

$$x \equiv -\frac{\sin^2 \theta}{r} \quad y \equiv \phi \quad z \equiv \frac{\cos \theta}{r^2} \quad (5.1)$$

629 Where r , θ , and ϕ take on their usual spherical meanings of radial distance, colatitude,
630 and azimuthal angle respectively.

631 The dipole coordinate x is constant over each equipotential shell², y is azimuthal angle,
632 and z indexes each field line from south to north. The unit vectors \hat{x} , \hat{y} , and \hat{z} point

¹The dipole coordinates x , y and z are perhaps more commonly named μ , ϕ , and ν respectively; however, in the present work, μ and ν take other meanings.

²In fact, x is inversely proportional to the McIlwain parameter L .

633 in the crosswise³ (radially outward at the equator), azimuthal (eastward), and parallel
 634 (northward at the equator) directions respectively.

Notably, the dipole coordinates in Equation (5.1) are normal to one another. While mathematically convenient, they do not readily accommodate a fixed-altitude boundary at the ionosphere, nor do they allow the dipole magnetic field to intersect the boundary at an oblique angle, as Earth's field does. As a solution, a nonorthogonal set of dipole coordinates was developed numerically by Proehl[76], then formalized analytically by Lysak[58] in terms of their contravariant components:

$$u^1 = -\frac{R_I}{r} \sin^2 \theta \quad u^2 = \phi \quad u^3 = \frac{R_I^2}{r^2} \frac{\cos \theta}{\cos \theta_0} \quad (5.2)$$

635 Above, R_I is the position of the ionosphere relative to Earth's center; it's typically taken
 636 to be $1 R_E + 100 \text{ km}$.

637 Like the dipole coordinates x , y , and z , Lysak's coordinates u^1 , u^2 , and u^3 correspond to
 638 L -shell, azimuthal angle, and position along a field line respectively. However, compared
 639 to z , u^3 has been renormalized using the invariant colatitude⁴ θ_0 . As a result, u^3 takes
 640 the value $+1$ at the northern ionospheric boundary and -1 at the southern ionospheric
 641 boundary for all field lines.

Because Lysak's coordinate system is not orthogonal⁵, it's necessary to consider covariant and contravariant basis vectors separately.

$$\hat{e}_i \equiv \frac{\partial}{\partial u^i} \underline{x} \quad \hat{e}^i \equiv \frac{\partial}{\partial \underline{x}} u^i \quad (5.3)$$

Covariant basis vectors \hat{e}_i are normal to the curve defined by constant u^i , while contravariant basis vectors \hat{e}^i are tangent to the coordinate curve (equivalently, \hat{e}^i is normal

³In the context of in situ measurements taken near the equatorial plane, \hat{x} is referred to as the radial direction; however, the present work extends the dipole grid to low altitudes, where \hat{x} can be more horizontal than vertical. The term "crosswise" is meant to indicate that \hat{x} is defined by the cross product of \hat{y} and \hat{z} .

⁴The invariant colatitude is the colatitude θ at which a field line intersects the ionosphere. It is related to the McIlwain parameter by $\cos \theta_0 \equiv \sqrt{1 - \frac{R_I}{L}}$.

⁵Curves of constant u^1 and curves of constant u^3 can intersect at non-right angles.

to the plane defined by constant u^j for all $j \neq i$). These vectors are reciprocal⁶ to one another, and can be combined to give components of the metric tensor $\underline{\underline{g}}$ [20].

$$\hat{e}^i \cdot \hat{e}_j = \delta_j^i \quad g_{ij} \equiv \hat{e}_i \cdot \hat{e}_j \quad g^{ij} \equiv \hat{e}^i \cdot \hat{e}^j \quad (5.4)$$

The metric tensor allows rotation between covariant and contravariant representations of vectors.

$$A_i = g_{ij} A^j \quad \text{and} \quad A^i = g^{ij} A_j \quad \text{where} \quad A_i \equiv \underline{A} \cdot \hat{e}_i \quad \text{and} \quad A^i \equiv \underline{A} \cdot \hat{e}^i \quad (5.5)$$

In addition, the determinant of the metric tensor is used to define cross products and curls⁷.

$$(\underline{A} \times \underline{B})^i = \frac{\varepsilon^{ijk}}{\sqrt{g}} A_j B_k \quad \text{and} \quad (\nabla \times \underline{A})^i = \frac{\varepsilon^{ijk}}{\sqrt{g}} \frac{\partial}{\partial u^j} A_k \quad \text{where} \quad g \equiv \det \underline{\underline{g}} \quad (5.6)$$

Explicit forms of the basis vectors and metric tensor can be found in the appendix of Lysak's 2004 paper[58]. At present, it's sufficient to note the mapping between Lysak's basis vectors and the usual dipole unit vectors.

$$\hat{x} = \frac{1}{\sqrt{g^{11}}} \hat{e}^1 \quad \hat{y} = \frac{1}{\sqrt{g^{22}}} \hat{e}^2 \quad \hat{z} = \frac{1}{\sqrt{g^{33}}} \hat{e}^3 \quad (5.7)$$

⁶⁴² TODO: Do these need to be written out? Referring people to the code, which will be in a public Git repository, is also a possibility.

The basis vectors can also be mapped to the spherical unit vectors, though Equation (5.8) is valid only at the ionospheric boundary.

$$\hat{\theta} = \frac{1}{\sqrt{g_{11}}} \hat{e}_1 \quad \hat{\phi} = \frac{1}{\sqrt{g_{22}}} \hat{e}_2 \quad \hat{r} = \frac{1}{\sqrt{g_{33}}} \hat{e}_3 \quad (5.8)$$

⁶The symbol δ_j^i is the Kronecker delta; the present work also makes use of the Levi-Civita symbol ε^{ijk} and Einstein's convention of implied summation over repeated indeces[23].

⁷The square root of the determinant of the metric tensor is called the Jacobian. It's sometimes denoted using the letter J , which is reserved for current in the present work.

644 The coordinates converge at the equatorial ionosphere, so an inner boundary is necessary
645 to maintain finite grid spacing. It's typically placed at $L = 2$. The outer boundary is
646 at $L = 10$. The dipole approximation of Earth's magnetic field is tenuous at the outer
647 boundary (particularly on the dayside); however, in practice, wave activity is localized
648 inside $L \sim 7$. The grid is spaced uniformly in u^1 , which gives finer resolution close to
649 Earth and coarser resolution at large distances.

650 Spacing in u^3 is set by placing grid points along the outermost field line. The points are
651 closest together at the ionosphere, and grow towards the equator. The spacing increases
652 in a geometric fashion, typically by 3%.

653 Typically, Tuna uses a grid 150 points in u^1 by 350 points in u^3 . The result is a resolution
654 on the order of 10 km at the ionosphere, which increases to the order of 10³ km at the
655 midpoint of the outermost field line.

656 There are no grid points in u^2 due to the two-and-a-half-dimensional nature of the
657 model. Fields are assumed to vary as $\exp(imu^2)$ — equally, $\exp(im\phi)$ — so derivatives
658 with respect to u^2 are equivalent to a factor of im . In effect, the real component of
659 each field is azimuthally in phase with the (purely real) driving, while imaginary values
660 represent behavior that is azimuthally offset.

661 The simulation's time step is set based on the grid spacing. As is the convention, δt is
662 set to match the smallest Alfvén zone crossing time, scaled down by a Courant factor
663 (typically 0.1). It bears noting that the smallest crossing time need not correspond to
664 the smallest zone; the Alfvén speed peaks several thousand kilometers above Earth's
665 surface, in the so-called Ionospheric Alfvén Resonator[61]. A typical time step is on the
666 order of 10⁻⁵ s.

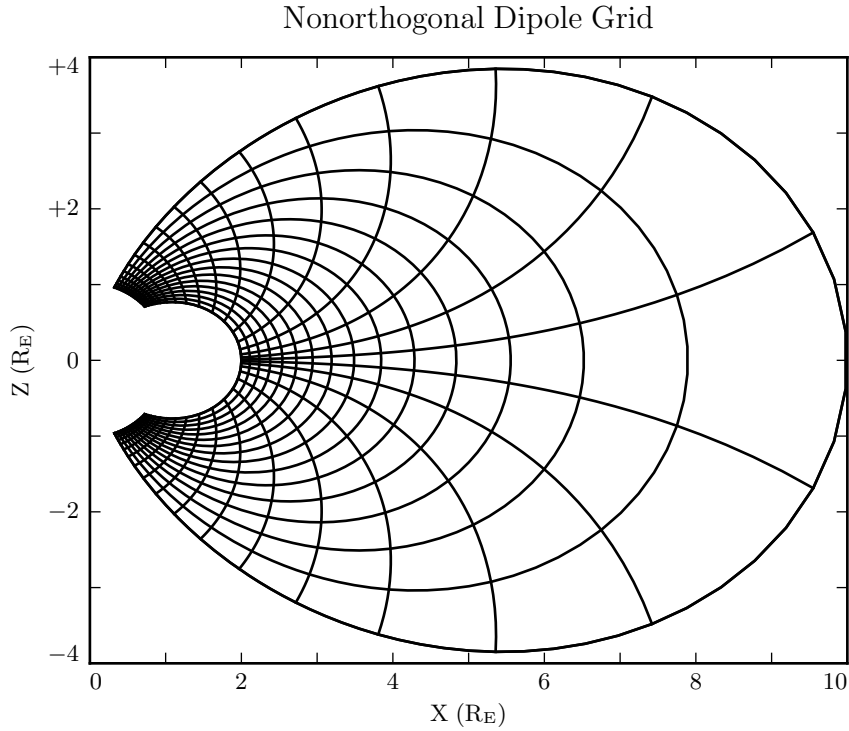


Figure 5.1: The model’s nonorthogonal dipole grid. Every fifth point is shown in each direction. The high concentration of grid points near Earth’s equator is a consequence of the coordinate system, which converges at the equatorial ionosphere. Earth (not shown) is centered at the origin with unit radius.

667 5.2 Physical Parameter Profiles

Tuna models Earth’s magnetic field to be an ideal dipole, so the zeroth-order field strength is written in the usual form:

$$\underline{B}_0 = 3.1 \times 10^4 \text{ nT} \left(\frac{R_E}{r} \right)^3 \left(2 \cos \theta \hat{r} - \sin \theta \hat{\theta} \right) \quad (5.9)$$

Number density is taken to be the sum of an inverse-radial-dependent auroral profile and a plasmaspheric profile dependent on the L -shell[61]:

$$n = n_{AZ} \frac{r_{AZ}}{r} + n_{PS} \exp\left(\frac{-L}{L_{PS}}\right) \left(\frac{1}{2} - \frac{1}{2} \tanh \frac{L - L_{PP}}{\delta L_{PP}} \right) \quad (5.10)$$

668 Where typical values are shown in Table 5.1.

Table 5.1: Typical Parameters for the Tuna Density Profile

Variable	Value	Description
L_{PS}	1.1	Scale L of the plasmasphere.
L_{PP}	4.0	Location of the plasmapause.
δL_{PP}	0.1	Thickness of the plasmapause.
n_{AZ}	$10 / \text{cm}^3$	Number density at the base of the auroral zone.
n_{PS}	$10^4 / \text{cm}^3$	Number density at the base of the plasmasphere.
r_{AZ}	1 R_E	Scale height of the auroral density distribution.

The perpendicular component of the electric tensor, ϵ_{\perp} , is computed based on Kelley's[48] tabulated low-density values, ϵ_K , which are adjusted to take into account the effects of high density in the plasmapause.

$$\epsilon_{\perp} = \epsilon_K + \frac{Mn}{B_0^2} \quad (5.11)$$

669 Where M is the mean molecular mass, which is large (~ 28 u) at 100 km altitude, then
670 drops quickly (down to 1 u by ~ 1000 km)[61].

671 The Alfvén speed profile is computed from the perpendicular electric constant in the
672 usual way, $v_A^2 \equiv \frac{1}{\mu_0 \epsilon_{\perp}}$. This form takes into account the effect of the displacement
673 current, which becomes important in regions where the Alfvén speed approaches the
674 speed of light.

675 While the density profile is held constant for all runs discussed in the present work,
676 the Alfvén speed profile is not. Four different profiles are used for the low-density

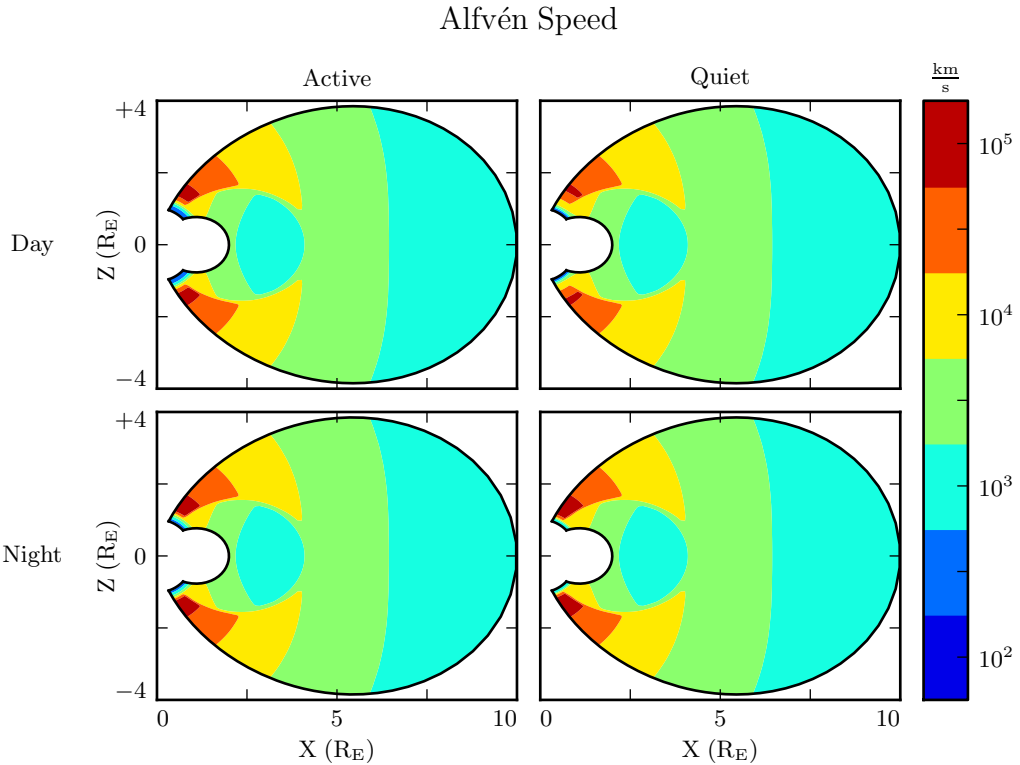


Figure 5.2: Alfvén speed profiles are based on low-density values tabulated by Kelley[48]. They are adjusted to take into account the density of the plasmapause and mass loading near the Earthward boundary.

677 perpendicular electric constant ϵ_K , corresponding to the differing ionospheric conditions
 678 between the dayside and the nightside, and between the high and low points in the
 679 solar cycle. These differences are visible in Figure 5.2, particularly in the size of the
 680 ionospheric Alfvén resonator (the peak in Alfvén speed in the high-latitude ionosphere).

681 **TODO:** Runs are only carried out for day and night... is it even worth showing the
 682 flank profile?

683 Ionospheric conductivity profiles are also based on values tabulated by Kelley, adjusted
 684 by Lysak[61] to take into account the abundance of heavy ions near the Earthward
 685 boundary. Pedersen, Hall, and parallel conductivities are each resolved by altitude, as
 686 shown in Figure 5.3.

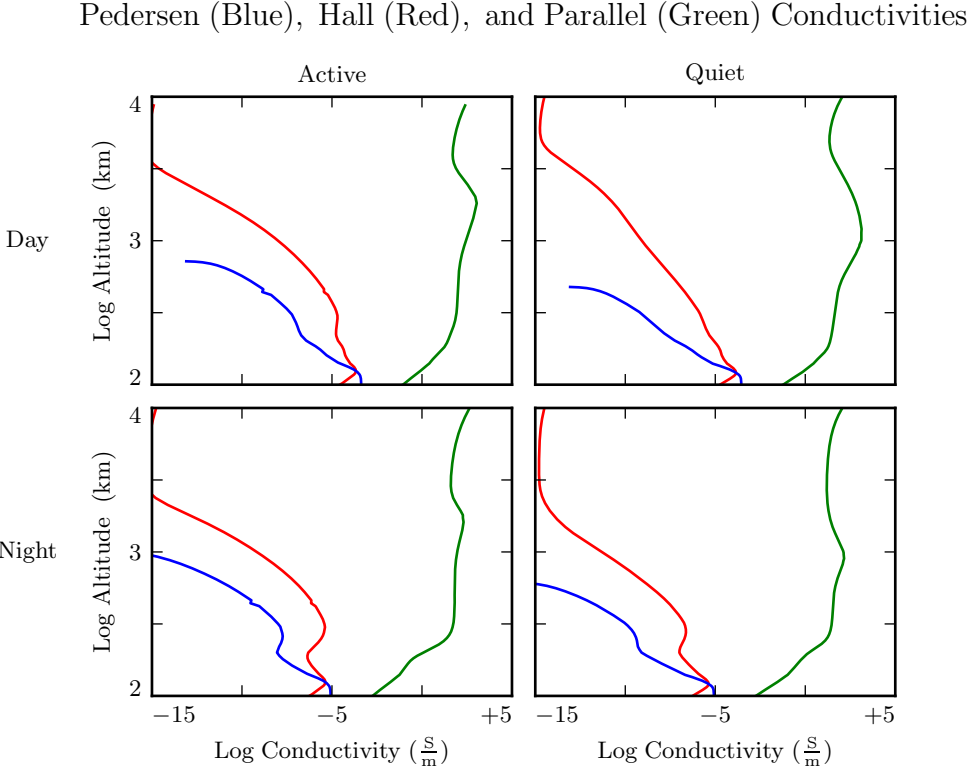


Figure 5.3: Ionospheric conductivity profiles are adapted by Lysak[61] from Kelley's tabulated values[48]. These profiles allow Tuna to simulate magnetosphere-ionosphere coupling under a variety of conditions.

687 Tuna's physical parameter profiles are static over the course of each run. Even so-called
 688 ultra low frequency waves like Pc4 pulsations are fast compared to convective timescales
 689 in the magnetosphere.

690 5.3 Driving

691 Models similar to Tuna have traditionally been driven using compression at the outer
 692 boundary[58, 61, 100, 101]. Such driving acts as a proxy for solar wind compression,
 693 Kelvin-Helmholtz effects at the magnetopause, and so on. However, because of the

694 constraints imposed by the dispersion relation for Alfvén waves⁸, simulations driven from
695 the outer boundary are constrained to the consideration of waves with low azimuthal
696 modenumber (equivalently, large azimuthal wavelength).

697 This issue is demonstrated in Figure 5.4. At low modenumber, energy delivered at
698 the outer boundary propagates across field lines in order to stimulate resonances in
699 the inner magnetosphere. However, as modenumber increases, Alfvén waves become
700 increasingly guided, and the inner magnetosphere is unaffected by perturbations at the
701 outer boundary.

702 In order to simulate high-modenumber Alfvén waves in the inner magnetosphere — such
703 as giant pulsations — a new driving mechanism is necessary. Perturbation of the ring
704 current is a natural choice, as Alfvén waves in the Pc4 range are known to interact with
705 ring current particles through drift and drift-bounce resonances. The ring current is a
706 dynamic region, particularly during and after geomagnetic storms; it's easy to imagine
707 the formation of localized inhomogeneities.

708 In order to estimate an appropriate magnitude for perturbations of the ring current,
709 the Sym-H storm index is used. The index is measured once per minute, and so cannot
710 directly detect ring current modulations in the Pc4 frequency range. Instead, the index
711 is transformed into the frequency domain, allowing a fit of its pink noise⁹.

712 **TODO:** Sym-H is basically the same as DST [99].

713 As shown in Figure 5.5, a Fourier transform of the Sym-H index (taken here from the
714 June 2013 storm) suggests that magnetic field perturbations at Earth's surface due to
715 ring current activity in the Pc4 frequency range could be up to the order of 10^{-2} nT.
716 Supposing that the ring current is centered around $5 R_E$ geocentric, that corresponds to
717 a current on the order of 0.1 MA. Tuna's driving is spread using a Gaussian profile in
718 u^1 (typically centered at $L = 5$) and u^3 (typically centered just off the equator), with a
719 characteristic area of $1 R_E^2$; this gives a current density on the order of $10^{-4} \mu\text{A}/\text{m}^2$.

⁸See Section 4.4.

⁹Pink noise, also called $\frac{1}{f}$ noise, refers to the power law decay present in the Fourier transforms of all manner of physical signals.

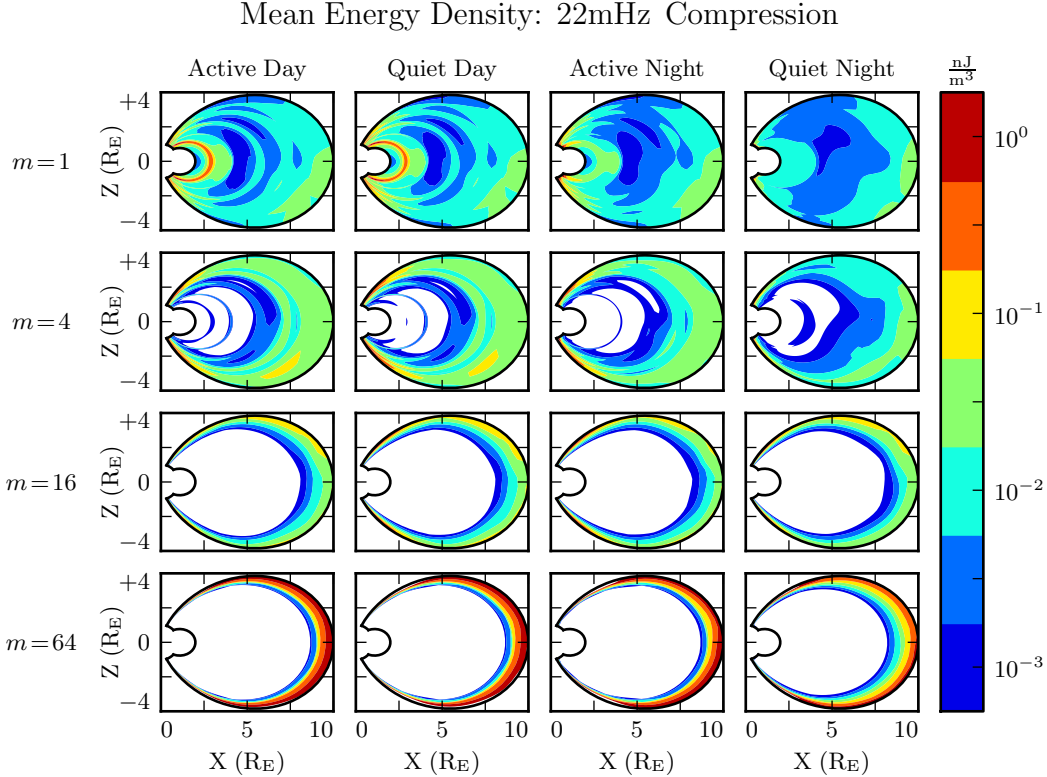


Figure 5.4: Each cell presents the mean energy density over the course of a 300 s run, as a function of position, due to compressional driving at the outer boundary. Azimuthal modenumber varies by row, and ionospheric conditions vary by column. For runs with small azimuthal modenumber, it's clear that energy is able to propagate across field lines and stimulate wave activity in the inner magnetosphere. When the modenumber is large, energy is unable to penetrate to the inner magnetosphere. Notably, the large values on the bottom row should be taken with a grain of salt; it's not clear that the model's results are reliable when waves are continuously forced against the boundary.

- 720 TODO: Admittedly, estimating the strength of localized perturbations using Sym-H —
 721 an index averaged over the entire globe — is a bit of a kludge.
- 722 In situ observations of Pc4 pulsations and giant pulsations have shown waves with
 723 modenumbers across the range $1 \lesssim m \lesssim 100$ [17, 18, 90]. Simulations are carried out
 724 across that range, corresponding to ring current perturbations with azimuthal extent as
 725 small as $0.5 R_E$.

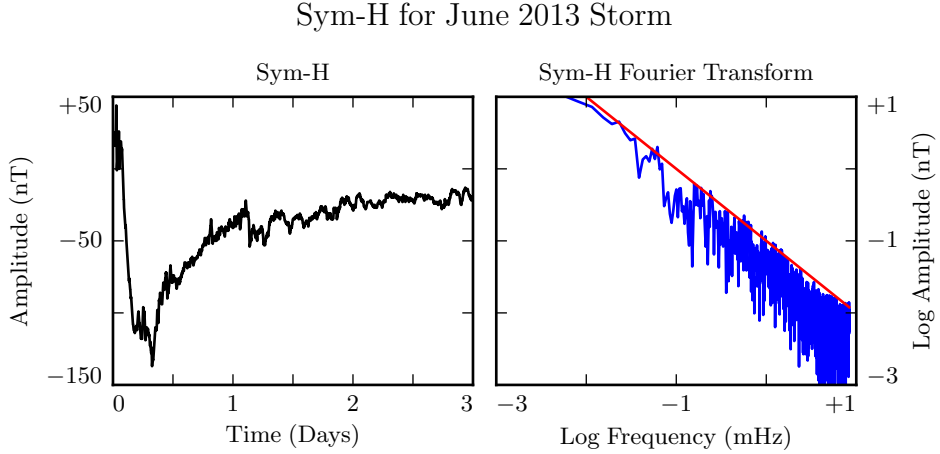


Figure 5.5: The Sym-H storm index[71] measures magnetic perturbations on Earth’s surface due to ring current activity. The amplitude of oscillations in the Pc4 range is estimated by fitting the pink noise in its Fourier transform.

- 726 TODO: Driving is delivered in the azimuthal component of the current only.
- 727 TODO: Driving is sinusoidal.
- 728 TODO: In case it’s not clear: Chapter 7 discusses ONLY simulations using ring current
729 driving. The only compressional driving we look at is Figure 5.4.
- 730 TODO: Driving on the dayside is centered at $L = 5$. On the nightside, due to the
731 increased Alfvén speed, it’s moved out to $L = 6$. The Alfvén bounce time at $L = 5$ on
732 the nightside is well above the Pc4 range.

733 5.4 Maxwell’s Equations

- 734 Tuna simulates the evolution of electromagnetic waves in accordance with Ampère’s
735 law and Faraday’s law. Computation is carried out on a Yee grid[105]: electric fields
736 and magnetic fields are offset by half a time step, and each field component is defined
737 on either odd or even grid points in each dimension to ensure that curls are computed
738 using centered differences.

The Ohmic current in Ampère's law is replaced with $\underline{\sigma} \cdot \underline{E}$ per Kirchhoff's formulation of Ohm's law. Then, taking \underline{J} to represent the driving current discussed in Section 5.3, Maxwell's equations can be written

$$\frac{\partial}{\partial t} \underline{B} = -\nabla \times \underline{E} \quad \underline{\epsilon} \cdot \frac{\partial}{\partial t} \underline{E} = \frac{1}{\mu_0} \nabla \times \underline{B} - \underline{J} - \underline{\sigma} \cdot \underline{E} \quad (5.12)$$

It is convenient to introduce shorthand for the curl of each field: $\underline{C} \equiv \nabla \times \underline{E}$ and $\underline{F} \equiv \nabla \times \underline{B} - \mu_0 \underline{J}$. Or, recalling Equation (5.6),

$$C^i = \frac{\varepsilon^{ijk}}{\sqrt{g}} \frac{\partial}{\partial u^j} E_k \quad F^i = \frac{\varepsilon^{ijk}}{\sqrt{g}} \frac{\partial}{\partial u^j} B_k - J^i \quad (5.13)$$

In these terms, Faraday's law can simply be written:

$$\frac{\partial}{\partial t} B^i = -C^i \quad (5.14)$$

Writing each component out explicitly, and using the metric tensor (per Equation (5.5)) to eliminate contravariant magnetic field components¹⁰, Equation (5.14) becomes:

$$\begin{aligned} B_1 &\leftarrow B_1 - g_{11} \delta t C^1 - g_{13} \delta t C^3 \\ B_2 &\leftarrow B_2 - g_{22} \delta t C^2 \\ B_3 &\leftarrow B_3 - g_{31} \delta t C^1 - g_{33} \delta t C^3 \end{aligned} \quad (5.15)$$

⁷³⁹ Note that the \leftarrow operator is used in Equation (5.15) to indicate assignment, rather than
⁷⁴⁰ equality. Terms on the left are new, while those on the right are old.

Unlike Faraday's law, Ampère's law cannot be trivially solved. Not only does the derivative of \underline{E} depend on its own future value, but the crosswise and azimuthal components of the equation are coupled by the Hall terms in the conductivity tensor. Fortunately,

¹⁰Fields are stored only in terms of their covariant components, and curls in terms of their contravariant components. This reduces Tuna's memory footprint (since each field need not be stored twice) as well as its computational cost (since time need not be spent rotating between bases). As a result, Tuna's solutions to Maxwell's equations are linear expressions whose coefficients are a mishmash of physical constants and geometric factors. To save time, each coefficient is computed once and stored, rather than being multiplied out from scratch with each time step.

the electric tensor can be inverted, allowing a solution by integrating factors:

$$\underline{\epsilon} \cdot \frac{\partial}{\partial t} \underline{E} = \frac{1}{\mu_0} \underline{F} - \underline{\sigma} \cdot \underline{E} \quad \text{becomes} \quad \left(\underline{\Omega} + \underline{\mathbb{I}} \frac{\partial}{\partial t} \right) \cdot \underline{E} = \underline{V}^2 \cdot \underline{F} \quad (5.16)$$

Where $\underline{\mathbb{I}}$ is the identity tensor and in x - y - z coordinates¹¹,

$$\underline{V}^2 \equiv \frac{1}{\mu_0} \underline{\epsilon}^{-1} = \begin{bmatrix} v_A^2 & 0 & 0 \\ 0 & v_A^2 & 0 \\ 0 & 0 & c^2 \end{bmatrix} \quad \text{and} \quad \underline{\Omega} \equiv \underline{\epsilon}^{-1} \cdot \underline{\sigma} = \begin{bmatrix} \frac{\sigma_P}{\epsilon_{\perp}} & \frac{-\sigma_H}{\epsilon_{\perp}} & 0 \\ \frac{\sigma_H}{\epsilon_{\perp}} & \frac{\sigma_P}{\epsilon_{\perp}} & 0 \\ 0 & 0 & \frac{\sigma_0}{\epsilon_0} \end{bmatrix} \quad (5.17)$$

Multiplying through by $\exp(\underline{\Omega} t)$ and applying the product rule, Equation (5.16) becomes¹²

$$\frac{\partial}{\partial t} \left(\exp(\underline{\Omega} t) \cdot \underline{E} \right) = \exp(\underline{\Omega} t) \cdot \underline{V}^2 \cdot \underline{F} \quad (5.18)$$

Equation (5.18) can then be integrated over a small time step δt and expressed in terms of the assignment operator introduced in Equation (5.15).

$$\underline{E} \leftarrow \exp(-\underline{\Omega} \delta t) \cdot \underline{E} + \delta t \exp(-\underline{\Omega} \frac{\delta t}{2}) \cdot \underline{V}^2 \cdot \underline{F} \quad (5.19)$$

The tensor exponential can be evaluated by splitting $\underline{\Omega}$ into the sum of its diagonal and Hall components¹³. The Hall exponential condenses into sines and cosines, giving a rotation around the magnetic field line:

$$\underline{E} \leftarrow \exp(-\underline{\Omega}' \delta t) \cdot \underline{R}_z \left(\frac{-\sigma_H \delta t}{\epsilon_{\perp}} \right) \cdot \underline{E} + \delta t \underline{V}^2 \cdot \exp(-\underline{\Omega}' \frac{\delta t}{2}) \cdot \underline{R}_z \left(\frac{-\sigma_H \delta t}{2\epsilon_{\perp}} \right) \cdot \underline{F} \quad (5.20)$$

¹¹Note the parallel component of the present definition of $\underline{\Omega}$ differs slightly from that used in Chapter 4, due to the present neglect of inertial effects; see Chapter 6.

¹²Tensor exponentiation is analogous to scalar exponentiation[37]: $\exp(\underline{T}) \equiv \sum_n \frac{1}{n!} \underline{T}^n$.

¹³For tensors, $\exp(\underline{S} + \underline{T}) = \exp(\underline{S}) \exp(\underline{T})$ as long as $\underline{S} \cdot \underline{T} = \underline{T} \cdot \underline{S}$.

Where

$$\underline{\underline{R}}_z(\theta) = \begin{bmatrix} \cos \theta & -\sin \theta & 0 \\ \sin \theta & \cos \theta & 0 \\ 0 & 0 & 1 \end{bmatrix} \quad \text{and} \quad \underline{\underline{\Omega}}' \equiv \begin{bmatrix} \frac{\sigma_P}{\epsilon_{\perp}} & 0 & 0 \\ 0 & \frac{\sigma_P}{\epsilon_{\perp}} & 0 \\ 0 & 0 & \frac{\sigma_0}{\epsilon_0} \end{bmatrix} \quad (5.21)$$

The parallel component of term of Equation (5.20) is simply

$$E_z \leftarrow E_z \exp\left(\frac{-\sigma_0 \delta t}{\epsilon_0}\right) + c^2 \delta t F_z \exp\left(\frac{-\sigma_0 \delta t}{2\epsilon_0}\right) \quad (5.22)$$

Or, using Equation (5.7) to map to the covariant basis,

$$E_3 \leftarrow E_3 \exp\left(\frac{-\sigma_0 \delta t}{\epsilon_0}\right) + c^2 \delta t (g_{31} F^1 + g_{33} F^3) \exp\left(\frac{-\sigma_0 \delta t}{2\epsilon_0}\right) \quad (5.23)$$

⁷⁴¹ Tuna's conductivity profile gives a minimum value of $\frac{\sigma_0 \delta t}{\epsilon_0}$ on the order of 10^3 , making
⁷⁴² $\exp\left(\frac{-\sigma_0 \delta t}{\epsilon_0}\right)$ far too small to be stored in a double precision variable¹⁴. That is, this
⁷⁴³ model takes E_3 (and, proportionally, E_z) to be uniformly zero. This issue is revisited
⁷⁴⁴ in Chapter 6.

The perpendicular components of Equation (5.20) give the expressions:

$$\begin{aligned} E_1 + \frac{g^{13}}{g^{11}} E_3 &\leftarrow E_1 \cos\left(\frac{-\sigma_H \delta t}{\epsilon_{\perp}}\right) \exp\left(\frac{-\sigma_P \delta t}{\epsilon_{\perp}}\right) \\ &\quad + E_2 \sin\left(\frac{-\sigma_H \delta t}{\epsilon_{\perp}}\right) \exp\left(\frac{-\sigma_P \delta t}{\epsilon_{\perp}}\right) \sqrt{\frac{g^{22}}{g^{11}}} \\ &\quad + E_3 \cos\left(\frac{-\sigma_H \delta t}{\epsilon_{\perp}}\right) \exp\left(\frac{-\sigma_P \delta t}{\epsilon_{\perp}}\right) \frac{g^{13}}{g^{11}} \\ &\quad + F^1 \cos\left(\frac{-\sigma_H \delta t}{2\epsilon_{\perp}}\right) \exp\left(\frac{-\sigma_P \delta t}{2\epsilon_{\perp}}\right) \frac{v_A^2 \delta t}{g^{11}} \\ &\quad + F^2 \sin\left(\frac{-\sigma_H \delta t}{2\epsilon_{\perp}}\right) \exp\left(\frac{-\sigma_P \delta t}{2\epsilon_{\perp}}\right) \frac{v_A^2 \delta t}{\sqrt{g^{11} g^{22}}} \end{aligned} \quad (5.24)$$

¹⁴Not coincidentally, $\frac{\sigma_0}{\epsilon_0}$ can also be written $\frac{\omega_P^2}{\nu}$. At the ionosphere, the collision frequency ν is fast compared to field line resonance timescales, but it's still slow compared to the plasma frequency.

and

$$\begin{aligned}
E_2 \leftarrow & -E_1 \sin\left(\frac{-\sigma_H \delta t}{\epsilon_{\perp}}\right) \exp\left(\frac{-\sigma_P \delta t}{\epsilon_{\perp}}\right) \sqrt{\frac{g^{11}}{g^{22}}} \\
& + E_2 \cos\left(\frac{-\sigma_H \delta t}{\epsilon_{\perp}}\right) \exp\left(\frac{-\sigma_P \delta t}{\epsilon_{\perp}}\right) \\
& - E_3 \sin\left(\frac{-\sigma_H \delta t}{\epsilon_{\perp}}\right) \exp\left(\frac{-\sigma_P \delta t}{\epsilon_{\perp}}\right) \frac{g^{13}}{\sqrt{g^{11} g^{22}}} \\
& - F^1 \sin\left(\frac{-\sigma_H \delta t}{2\epsilon_{\perp}}\right) \exp\left(\frac{-\sigma_P \delta t}{2\epsilon_{\perp}}\right) \frac{v_A^2 \delta t}{\sqrt{g^{11} g^{22}}} \\
& + F^2 \cos\left(\frac{-\sigma_H \delta t}{2\epsilon_{\perp}}\right) \exp\left(\frac{-\sigma_P \delta t}{2\epsilon_{\perp}}\right) \frac{v_A^2 \delta t}{g^{22}}
\end{aligned} \tag{5.25}$$

745 The E_3 terms in Equations (5.24) and (5.25) can be ignored at present. They are
746 revisited in Chapter 6.

747 It bears recalling that the driving current is defined as part of \underline{F} , per Equation (5.13).
748 When the driving current is purely azimuthal ($J^1 = J^3 = 0$), the driving is in principle
749 applied to both the poloidal and the toroidal electric fields through F^2 . However,
750 in practice, the driving applied to the toroidal electric field is vanishingly small. The
751 driving current J^2 is localized around $5 R_E$ geocentric, and $\exp\left(\frac{-\sigma_P \delta t}{2\epsilon_{\perp}}\right)$ drops off quickly
752 with altitude.

753 5.5 Boundary Conditions

754 Dirichlet and Neumann boundary conditions are applied to the electric field components
755 and magnetic field components respectively. That is, electric fields are forced to go to
756 zero at the inner and outer boundaries, and magnetic fields are forced to have a zero
757 derivative normal to the inner and outer boundaries.

758 These boundary conditions can in principle cause nonphysical reflections at the bound-
759 ary¹⁵. However, in practice, wave activity is concentrated well within the simulation
760 domain. Simulation results are robust under an exchange of Dirichlet and Neumann

¹⁵See, for example, the bottom row of Figure 5.4.

761 boundary conditions (though a self-inconsistent set of boundary condidtions, such as
 762 applying Neumann boundary conditions to B_1 but Dirichlet boundary conditions to B_3 ,
 763 quickly causes instability).

764 The Earthward boundary conditions are as follows.

Between the top of the neutral atmosphere and the bottom of the ionosphere, the model includes a thin, horizontal current sheet representing the ionosphere's E layer[58]. By integrating Ampère's law over the layer, it can be shown[27] that the horizontal electric field values at the edge of the grid are determined by the jump in the horizontal magnetic fields:

$$\underline{\underline{\Sigma}} \cdot \underline{E} = \frac{1}{\mu_0} \lim_{\delta r \rightarrow 0} \left[\hat{r} \times \underline{B} \right]_{R_I - \delta r}^{R_I + \delta r} \quad (5.26)$$

The integrated conductivity tensor $\underline{\underline{\Sigma}}$ can be written in θ - ϕ coordinates as[58]:

$$\underline{\underline{\Sigma}} \equiv \begin{bmatrix} \frac{\Sigma_0 \Sigma_P}{\Sigma_0 \cos^2 \alpha + \Sigma_P \sin^2 \alpha} & \frac{-\Sigma_0 \Sigma_H}{\Sigma_0 \cos^2 \alpha + \Sigma_P \sin^2 \alpha} \\ \frac{\Sigma_0 \Sigma_H}{\Sigma_0 \cos^2 \alpha + \Sigma_P \sin^2 \alpha} & \Sigma_P + \frac{\Sigma_H^2 \sin^2 \alpha}{\Sigma_0 \cos^2 \alpha + \Sigma_P \sin^2 \alpha} \end{bmatrix} \quad (5.27)$$

765 Where α is the angle between the magnetic field and the vertical direction, given by
 766 $\cos \alpha \equiv \frac{-2 \cos \theta}{\sqrt{1+3 \cos^2 \theta}}$, and Σ_P , Σ_H , and Σ_0 are the height-integrated Pedersen, Hall,
 767 and parallel conductivities respectively. Their values are determined by integrating
 768 Kelley's[48] conductivity profiles from Earth's surface to the ionospheric boundary; val-
 769 ues are shown in Table 5.2.

Table 5.2: Integrated Atmospheric Conductivity (S)

	Σ_0	Σ_P	Σ_H
Active Day	424	0.65	6.03
Quiet Day	284	0.44	4.02
Active Night	9	0.01	0.12
Quiet Night	9	0.01	0.12

An expression for the horizontal electric fields at the boundary can be obtained by inverting Equation (5.26). After mapping to covariant coordinates per Equation (5.8), and taking $\Sigma \equiv \det \underline{\underline{\Sigma}}$,

$$\begin{aligned} E_1 &\leftarrow \frac{1}{\mu_0 \Sigma} \lim_{\delta r \rightarrow 0} \left[-\Sigma_{\theta\phi} B_1 - \sqrt{\frac{g_{11}}{g_{22}}} \Sigma_{\phi\phi} B_2 \right]_{R_I-\delta r}^{R_I+\delta r} \\ E_2 &\leftarrow \frac{1}{\mu_0 \Sigma} \lim_{\delta r \rightarrow 0} \left[\sqrt{\frac{g_{22}}{g_{11}}} \Sigma_{\theta\theta} B_1 + \Sigma_{\phi\theta} B_2 \right]_{R_I-\delta r}^{R_I+\delta r} \end{aligned} \quad (5.28)$$

770 In order to compute the atmospheric magnetic field, a scalar magnetic potential (Ψ
771 such that $\underline{B} = \nabla\Psi$) is computed as a linear combination of harmonics. The neutral
772 atmosphere is considered to be a perfect insulator, giving $\nabla \times \underline{B} = 0$. Combined with
773 $\nabla \cdot \underline{B} = 0$ (per Maxwell's equations), Ψ satisfies Laplace's equation, $\nabla^2\Psi = 0$.

Laplace's equation can be solved analytically; however, a numerical solution is preferable to ensure orthonormality on a discrete and incomplete¹⁶ grid. After separating out the radial and azimuthal dependence in the usual way, the latitudinal component of Laplace's equation can be written in terms of $s \equiv -\sin^2\theta$:

$$(4s^2 + 4s) \frac{d^2}{ds^2} Y_\ell + (4 + 6s) \frac{d}{ds} Y_\ell - \frac{m^2}{s} Y_\ell = \ell(\ell+1) Y_\ell \quad (5.29)$$

Using centered differences to linearize the derivatives, Equation (5.29) becomes a system of coupled linear equations, one per field line. It can be solved numerically for eigenvalues $\ell(\ell+1)$ and eigenfunctions Y_ℓ ¹⁷. In terms of the harmonics Y_ℓ , Ψ between the Earth's surface and the top of the atmosphere can be written using eigenweights a_ℓ and b_ℓ :

$$\Psi = \sum_\ell \left(a_\ell r^\ell + b_\ell r^{-\ell-1} \right) Y_\ell \quad (5.30)$$

¹⁶As discussed in Section 5.1, the grid is constrained to finite L , which excludes the equator as well as the poles.

¹⁷Solving Laplace's equation analytically results in spherical harmonics indexed by both ℓ and m , the separation constants for θ and ϕ respectively. In two and a half dimensions, ϕ is not explicitly resolved, so m is set manually.

As a boundary condition for Ψ , Earth is assumed to be a perfect conductor. This forces the magnetic field at Earth's surface to be horizontal; that is, $B_r = \frac{\partial}{\partial r} \Psi = 0$. Noting that solutions to Laplace's equation are orthonormal, each element of the sum in Equation (5.30) must be independently zero at R_E . This allows the coefficients a_ℓ and b_ℓ to be expressed in terms of one another.

$$b_\ell = \frac{\ell}{\ell + 1} R_E^{2\ell+1} a_\ell \quad (5.31)$$

The current sheet at the top of the atmosphere is assumed to be horizontal, so the radial component of the magnetic field must be the same just above and just below it. Taking the radial derivative of Equation (5.30) at the top of the atmosphere, and eliminating b_ℓ with Equation (5.31), gives

$$B_r = \sum_\ell \ell a_\ell R_I^{\ell-1} \left(1 - \lambda^{2\ell+1}\right) Y_\ell \quad \text{where} \quad \lambda \equiv \frac{R_E}{R_I} \sim 0.975 \quad (5.32)$$

The summation can be collapsed by “integrating” over a harmonic¹⁸. Inverse harmonics can be obtained by inverting the eigenvector matrix. Then $Y_\ell \cdot Y_{\ell'}^{-1} = \delta_{\ell\ell'}$ by construction.

$$a_\ell = \frac{1}{\ell R_I^{\ell-1}} \frac{B_r \cdot Y_\ell^{-1}}{1 - \lambda^{2\ell+1}} \quad (5.33)$$

Combining Equations (5.30), (5.31), and (5.33) allows the expression of Ψ at the top and bottom of the atmosphere as a linear combination of radial magnetic field components at the bottom of the ionosphere.

$$\begin{aligned} \Psi_E &= \sum_\ell Y_\ell \frac{R_I}{\ell (\ell - 1)} \frac{(2\ell - 1) \lambda^\ell}{1 - \lambda^{2\ell+1}} B_r \cdot Y_\ell^{-1} \\ \Psi_I &= \sum_\ell Y_\ell \frac{R_I}{\ell (\ell - 1)} \frac{(\ell - 1) + \ell \lambda^{2\ell+1}}{1 - \lambda^{2\ell+1}} B_r \cdot Y_\ell^{-1} \end{aligned} \quad (5.34)$$

¹⁸Because the functions are defined on a discrete grid, their inner product is not an integral, but a sum: $B_r \cdot Y_\ell^{-1} \equiv \sum_i B_r[i] Y_\ell^{-1}[i]$.

Horizontal magnetic fields are obtained by taking derivatives of Ψ .

$$B_1 = \frac{\partial}{\partial u^1} \Psi \quad B_2 = \frac{\partial}{\partial u^2} \Psi \quad (5.35)$$

- 774 Horizontal magnetic field values at the top of the atmosphere are used to impose bound-
775 ary conditions on the electric fields at the bottom of the ionosphere, per Equation (5.28).
776 Those at Earth's surface are valuable because they allow a direct comparison between
777 model output and ground magnetometer data, after being mapped to physical coordi-
778 nates per Equation (5.8).

779 **Chapter 6**

780 **Electron Inertial Effects**

781 As laid out in Chapter 5, Tuna resolves neither parallel currents nor parallel electric
782 fields. This is unfortunate; parallel electric fields generated by kinetic and inertial Alfvén
783 waves (including fundamental field line resonances[79, 95]) are a topic of particular
784 interest in the study of auroral particle precipitation.

Parallel currents and electric fields can be added to Tuna through the consideration of electron inertial effects in Ohm's law:

$$0 = \sigma_0 E_z - J_z \quad \text{becomes} \quad \frac{1}{\nu} \frac{\partial}{\partial t} J_z = \sigma_0 E_z - J_z \quad (6.1)$$

With the addition of the electron inertial term, it is necessary to track the parallel current independent of the parallel electric field¹. Solving by integrating factors² gives

$$J_3 \leftarrow J_3 \exp(-\nu \delta t) + \delta t \frac{ne^2}{m_e} E_3 \exp\left(-\nu \frac{\delta t}{2}\right) \quad (6.2)$$

¹The parallel current J_z is defined on the same points of the Yee grid as E_z . It is offset in time by half of a time step.

²The integrating factors technique is laid out explicitly for Ampère's law in Section 5.4.

From there, the parallel electric field can be updated directly; Equation (5.23) is replaced by the following:

$$E_3 \leftarrow E_3 + c^2 \delta t (g_{31} F^1 + g_{33} F^3) - \frac{\delta t}{\epsilon_0} J_3 \quad (6.3)$$

785 The present section explores the complications that arise from the addition of the elec-
 786 tron inertial term to Ohm's law, as well as a few results that may be gleaned despite
 787 those complications. Notably — for reasons discussed in Section 6.3 — the results
 788 presented in Chapter 7 do not make use of the electron inertial term.

789 6.1 The Boris Factor

With the addition of the electron inertial term, a cyclical dependence appears between Ampère's law and Ohm's law:

$$\frac{\partial}{\partial t} E_z \sim -\frac{1}{\epsilon_0} J_z \quad \text{and} \quad \frac{\partial}{\partial t} J_z \sim \frac{ne^2}{m_e} E_z \quad \text{so} \quad \frac{\partial^2}{\partial t^2} E_z \sim -\omega_P^2 E_z \quad (6.4)$$

790 That is, electron inertial effects come hand in hand with the plasma oscillation.
 791 As mentioned in Chapter 4 and shown in Figure 6.1, plasma oscillation is quite fast —
 792 several orders of magnitude smaller than Tuna's time step as determined in Section 5.1
 793 ($\sim 10 \mu\text{s}$). This poses a conundrum. At Tuna's usual time step, the plasma oscillation
 794 becomes unstable within seconds³. On the other hand, reducing the time step by three
 795 orders of magnitude to resolve the plasma oscillation is computationally infeasible; a
 796 run slated for an hour would require six weeks to complete.
 797 As it happens, this problem can be solved by artificially increasing the parallel electric
 798 constant above its usual value of ϵ_0 . Doing so lowers both the speed of light and the
 799 plasma frequency within the simulation.
 800 This technique — and others like it — has been widespread in numerical modeling since
 801 it was presented by Boris in 1970[6]. More recently, Lysak and Song considered its use

³For stability, $\omega_P \delta t < 1$ is necessary.

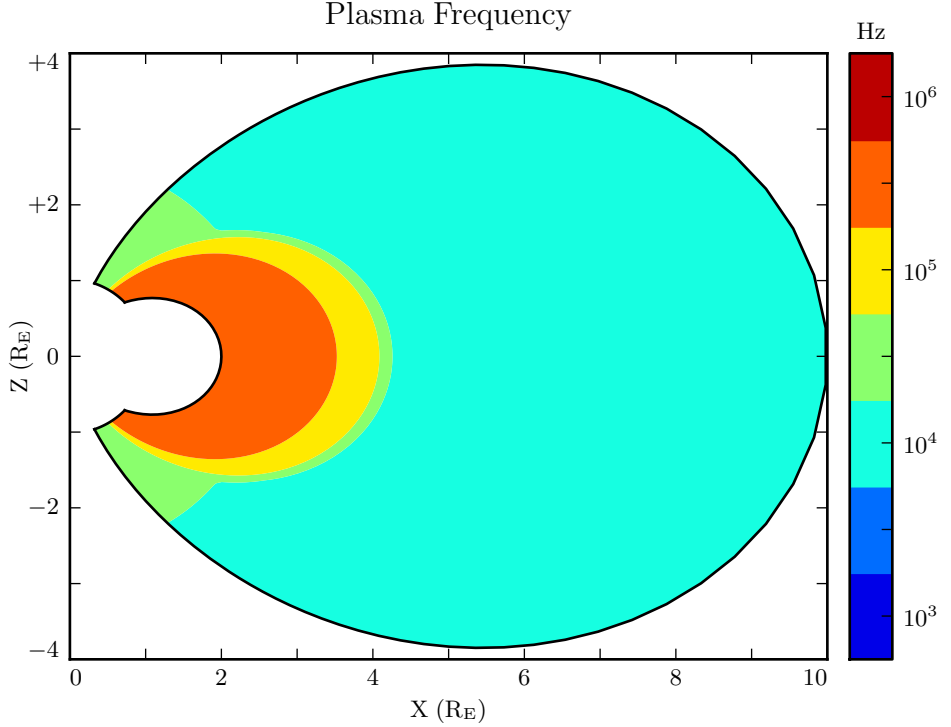


Figure 6.1: The plasma frequency reaches a peak value just under 10^6 Hz near the equator. Outside the plasmasphere, its value is closer to 10^4 Hz, which is still not well-resolved by Tuna's usual time step.

802 specifically for the case of electron inertial effects[60]. The following paraphrases their
 803 argument.

Supposing that the current and electric field are oscillating at frequency ω , the parallel components of Ampère's law and Ohm's law can be written

$$-i\omega\epsilon_0 E_z = \frac{1}{\mu_0} (\nabla \times \underline{B})_z - J_z \quad -\frac{i\omega}{\nu} J_z = \sigma_0 E_z - J_z \quad (6.5)$$

Then, eliminating the current, the parallel electric field can be related to the curl of the magnetic field by⁴

$$\left(1 - \frac{\omega^2 - i\nu\omega}{\omega_P^2}\right) E_z = \frac{c^2}{\omega_P^2} (\nu - i\omega) (\nabla \times \underline{B})_z \quad (6.6)$$

- 804 In Equation (6.6), $\frac{c}{\omega_P}$ is the electron inertial length. While the speed of light and the
 805 plasma frequency each depend on ϵ_0 , their ratio does not. This allows an estimation of
 806 how much the model should be affected by an artificially-large electric constant (and
 807 thus an artificially-small plasma frequency). So long as $\frac{\omega^2 - i\nu\omega}{\omega_P^2}$ remains small compared
 808 to unity, the model should behave faithfully.
- 809 For waves with periods of a minute or so, even perhaps-implausibly large Boris factors
 810 are allowed; for example, increasing ϵ_0 by a factor of 10^6 gives $\left|\frac{\omega^2 + i\omega\nu}{\omega_P^2}\right| \lesssim 0.01$.

811 6.2 Parallel Currents and Electric Fields

- 812 As discussed in Section 4.4, parallel electric fields in this regime are expected to be six
 813 or more orders of magnitude smaller than the perpendicular electric fields. Numerical
 814 results show general agreement: in Figure 6.2, the parallel electric field appears com-
 815 parable to its perpendicular counterparts only after its been scaled up by six orders of
 816 magnitude.
- 817 As such, the inclusion of electron inertial effects does not appreciably impact the sim-
 818 ulation's gross behavior; in Faraday's law, $\nabla \times \underline{E}$ is essentially unaffected. Side by side
 819 snapshots of the magnetic fields in runs carried out with and without electron inertial
 820 effects are not visibly distinguishable⁵ (not shown).
- 821 Even if there is no significant feedback through Faraday's law, it's informative to con-
 822 sider the structures that arise in parallel currents and electric fields driven by pertur-
 823 bations in the ring current. For example, the parallel electric field perturbation (with

⁴From Equation (4.4), $c^2 \equiv \frac{1}{\mu_0 \epsilon_0}$ and $\sigma_0 \equiv \frac{ne^2}{m_e \nu}$ and $\omega_P^2 \equiv \frac{ne^2}{m_e \epsilon_0}$.

⁵In a sense, this is reassuring. It ensures that the present section does not cast doubt on the results presented in Chapter 7, where electron inertial effects are neglected.

Electric Field Snapshots: Quiet Day, 10mHz Current, $m = 16$

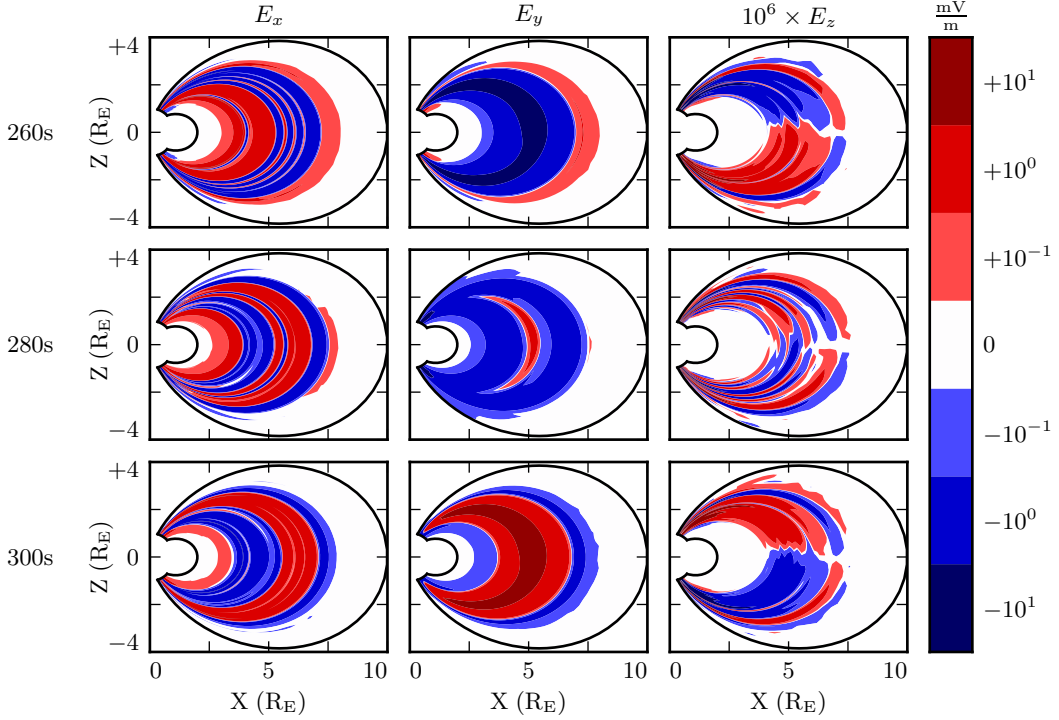


Figure 6.2: Parallel electric fields are smaller than perpendicular electric fields by about six orders of magnitude. As a result, parallel electric fields do not contribute significantly to $\nabla \times \underline{E}$ in Faraday's law.

maxima near the ionosphere) exhibits the opposite harmonic structure to the perpendicular electric field components (which peak near the equator). It is furthermore notable that the parallel electric field (and the parallel current that comes from it) exhibits real and imaginary components of comparable magnitude.

TODO: The compressional component of the magnetic field is also flipped compared to the perpendicular components. Should this have been mentioned in Chapter 3, with the figures showcasing harmonic structure? Radoski showed that it should be the case[78].

831

At low altitude, where the Hall conductivity muddles all of the electric field components together, parallel currents coincide with strong Poynting flux. The imaginary component

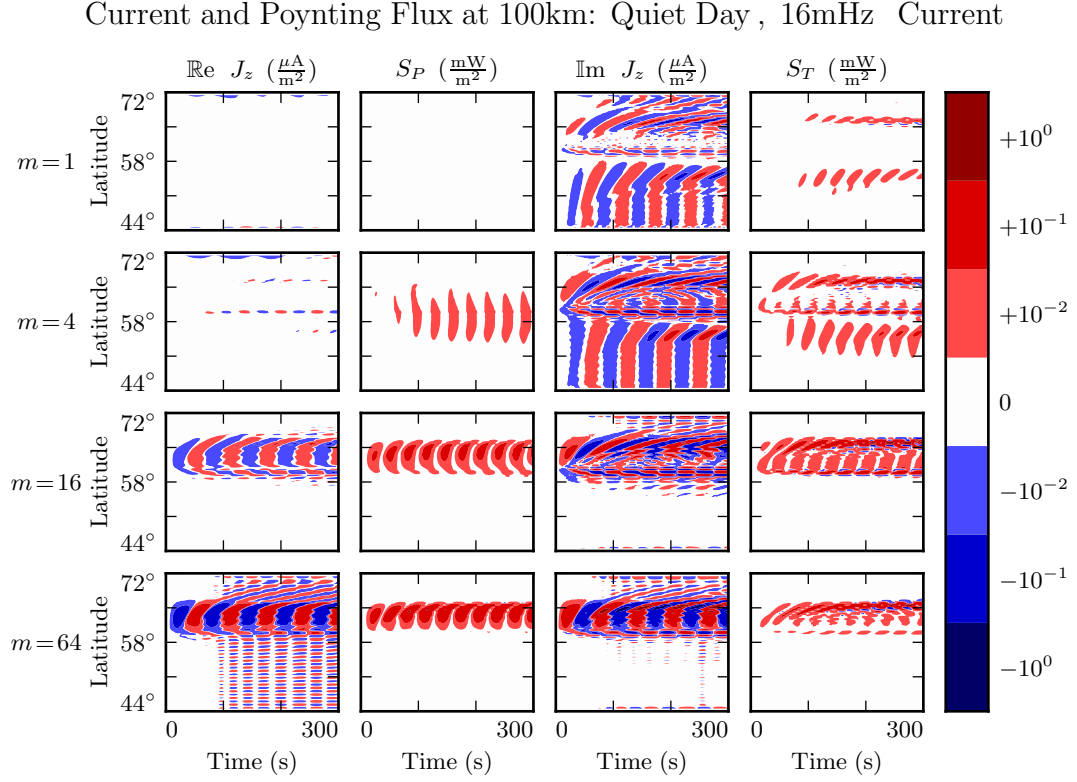


Figure 6.3: TODO: ...

of the current lines up with the toroidal Poynting flux (which comes from imaginary E_x and imaginary B_y^*), while the real current lines up with the poloidal Poynting flux (E_y and B_x^* are real)⁶. This is shown in Figure 6.3, which lays out the real and imaginary components of the parallel current (in the first and third column respectively) next to the poloidal and toroidal Poynting flux (second and fourth columns). Four runs are shown, one per row, with azimuthal modenumbers 1, 4, 16, and 64. Values are measured at an altitude of 100 km, the edge of the simulation.

Notably, the Poynting flux waveforms are rectified — they primarily carry energy Earthward. The current, on the other hand, alternates between upward and downward flow.

⁶As mentioned in Chapter 5, poloidal field components are in practice overwhelmingly real, indicating that they coincide azimuthally with the (real) driving. Toroidal components are overwhelmingly imaginary, which corresponds to an azimuthal offset.

- 843 This effect presumably arises because the current is a linear quantity while the Poynting
 844 flux is quadratic: the electric and magnetic fields that make it up oscillate in phase, so
 845 their product is positive even when they are negative.
- 846 At higher altitude, where the Hall conductivity is small, parallel current is associated
 847 only with the toroidal mode. Figure 6.4 shows data from the same runs as Figure 6.3,
 848 arranged in the same way, but the values are taken at an altitude of 1000 km instead of
 849 100 km.
- 850 In Figure 6.4, as in Figure 6.3, the imaginary component of the parallel current (third
 851 column) coincides more or less with the toroidal Poynting flux (fourth column). How-
 852 ever, the real component of the parallel current (first column) is vanishingly small, even
 853 when the poloidal Poynting flux (second column) is strong. **TODO: Is this expected?**
 854 **Tikhonchuk[95] looks specifically at the toroidal mode when considering shear Alfven**
 855 **waves. Does the poloidal mode count as compressional even when it's guided?**
- 856 The magnitude of the parallel current tops out over $1 \mu\text{A}/\text{m}^2$, just shy of the up-to-tens
 857 of $\mu\text{A}/\text{m}^2$ inferred from ground observations and seen in situ[8, 46, 82].

It's also possible to consider the effect of parallel currents and electric fields on the ionosphere's energy budget, per Poynting's theorem:

$$\frac{\partial}{\partial t} u = -\nabla \cdot \underline{E} - \underline{J} \cdot \underline{E} \quad (6.7)$$

- 858 As shown in Figure 6.5, little energy transfer in the ionosphere is mediated by perpen-
 859 dicular components of the Poynting flux. The parallel component of $\underline{J} \cdot \underline{E}$ is comparably
 860 unimportant. The energy deposited in the ionosphere by the Poynting flux matches
 861 closely with the energy lost to Joule dissipation — as it should, to conserve energy
 862 — but according to the model, parallel currents and electric fields do not contribute
 863 significantly.

Current and Poynting Flux at 1000km: Quiet Day , 16mHz Current

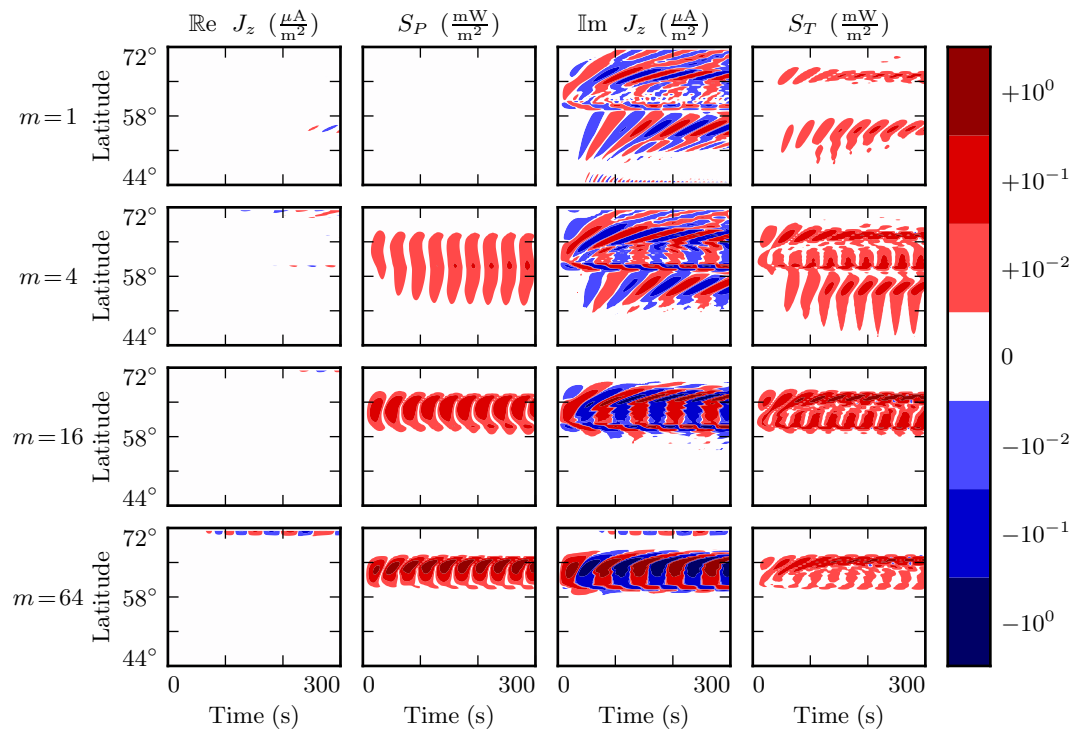


Figure 6.4: TODO: ...

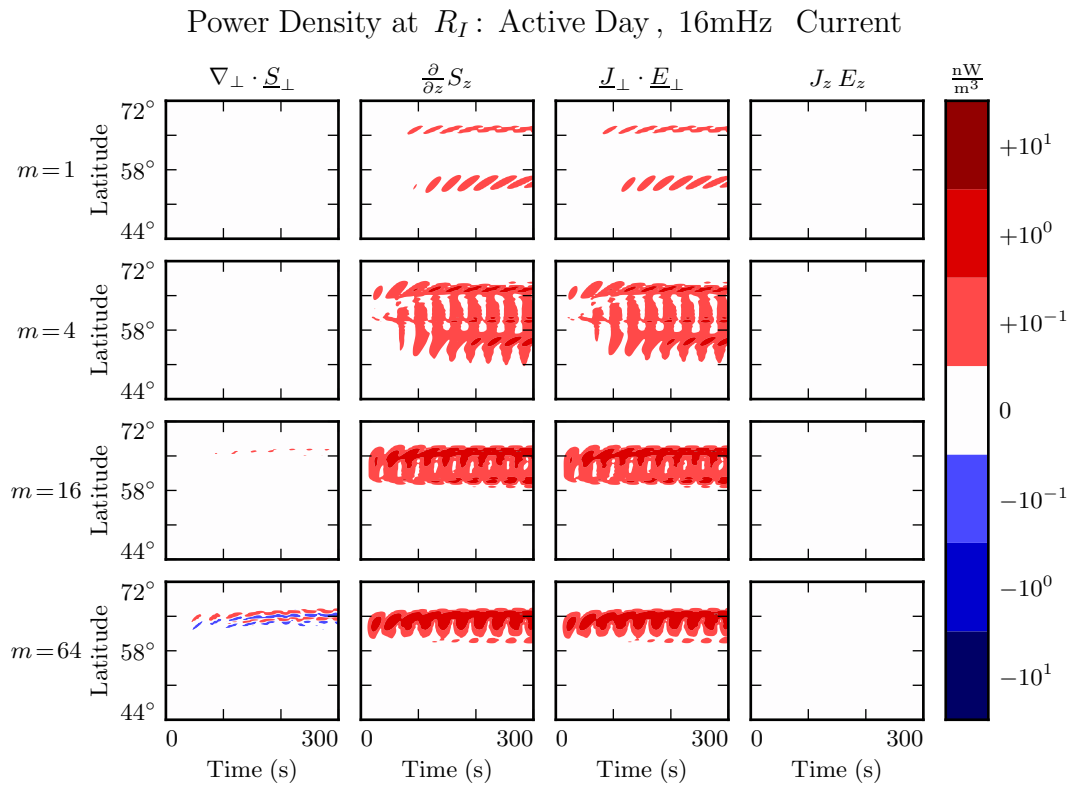


Figure 6.5: While field-aligned currents can be of significant size, they are not particularly good at depositing energy in the ionosphere. Energy deposited by the Poynting flux matches closely with Joule dissipation from the perpendicular currents, while $J_z E_z$ is smaller by several orders of magnitude.

864 **6.3 Inertial Length Scales**

865 It's not quite fair to compare the parallel and perpendicular contributions to $\nabla \times \underline{E}$ as
866 is done in Section 6.2. Perpendicular electric fields are on the order of 1 mV/m, with
867 wavelengths on the order of 10^5 km; they give rise to magnetic field gradients around
868 0.1 nT/s. Parallel electric fields, closer to 10^{-6} mV/m, would need to vary over length
869 scales of 0.1 km to match with that.

870 Such scales are believable. The characteristic length scale of the plasma oscillation is
871 the electron inertial length, $\frac{c}{\omega_p}$, which is on the order of 1 km in the auroral ionosphere
872 and 0.1 km in the low-altitude plasmasphere. However, Tuna's usual grid doesn't resolve
873 structures so fine; its resolution bottoms out closer to 10 km. That is, with the inclusion
874 of electron inertial effects, Tuna's grid is too coarse to resolve all of the waves expected
875 to be present. The model is prone to instability as a result.

876 Figure 6.6 shows a run with perpendicular resolution smaller than the electron inertial
877 length, side by side with an analogous run on the usual grid. In order to carry out
878 the inertial-scale run, several concessions were made to computational cost. The run
879 simulates only a duration of 100 s (other results in previous sections and in Chapter 7
880 show 300 s), and the grid covers only the auroral latitudes from $L = 5$ to $L = 7$.

881 Even so, the run presents a significant computational expense. Spread over 16 cores, a
882 100 s run on Tuna's usual grid takes well under an hour. The inertial-scale run barely
883 finished in 96 hours, the cutoff at the Minnesota Supercomputing Institute⁷.

884 The snapshot shown in Figure 6.6 uses a perpendicular grid resolution of 0.7 km at the
885 Earthward edge, which just satisfies the Nyquist rate for the minimum inertial length
886 of 1.7 km. It's still too coarse. There is clearly some small-scale structure developing in
887 the ionosphere, but it's not well resolved. The large number of "wiggles" portends an
888 imminent crash.

⁷Runtime goes as the inverse square of grid resolution. Not only does finer resolution require more grid cells, but it also gives rise to proportionally smaller crossing times, imposing a smaller time step.

Parallel Electric Fields: Quiet Day, 100s of 16mHz Current, $m = 16$

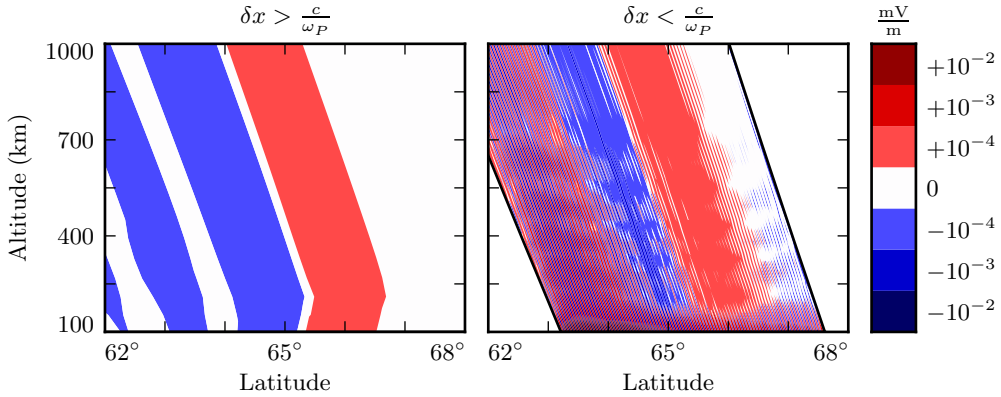


Figure 6.6: The parallel electric field develops significant structure when the perpendicular grid resolution is smaller than the electron inertial length. Unfortunately, such runs are prohibitively expensive. The lower panel — which still fails to resolve wave structure properly — represents a 100-fold increase in computational time.

889 6.4 Discussion

890 TODO: The dispersion relation in Chapter 4 suggests that parallel electric fields should
 891 be smaller than perpendicular electric fields by at least six orders of magnitude. Tuna
 892 agrees.

893 TODO: Tuna computes parallel currents a bit weaker than those that are observed —
 894 $\sim 1 \mu\text{A}/\text{m}^2$ rather than $\sim 10 \mu\text{A}/\text{m}^2$. The currents accompany the toroidal mode, but
 895 not the poloidal mode, except where the two are coupled by a strong Hall conductivity.
 896 Is this expected?

897 TODO: When inertial effects are not properly resolved, the code is prone to instability.
 898 Resolving inertial scales properly presents a prohibitive computational expense.

899 Electron inertial effects present a promising first-principles-based approach to the in-
 900 vestigation of parallel currents and electric fields associated with field line resonances.
 901 Unfortunately, because of the large differences in scale between Pc4 pulsations and the

902 plasma oscillation, the proper deployment of inertial effects presents a prohibitive com-
903 putational expense. Results shown in Chapter 7 make use of the core version of Tuna
904 presented in Chapter 5, which does not include the effects of electron inertia.

905 **Chapter 7**

906 **Numerical Results**

907 TODO: An overarching motivation for the present work is that FLRs exhibit significant
908 behavioral changes as a result of their azimuthal modenumber, but that prior models
909 have been unable to provide a good picture.

910 **7.1 Modenumber and Compression**

911 It's well known that the poloidal FLR mode is compressional at low modenumber,
912 but guided at high modenumber. However, the relationship is not well quantified.
913 Theoretical work has historically been concerned with the limits $m \rightarrow 0$ and $m \rightarrow$
914 ∞ [15, 78], and only a handful of satellite observations have explicitly considered an
915 event's azimuthal modenumber[18, 70, 90]. Using results from Tuna, the present section
916 examines the strength of the poloidal wave's compressional component at an ensemble
917 of finite modenumbers.

918 Figures 7.1 and 7.2 show magnetic field snapshots taken from a pair of runs. The first
919 uses a small azimuthal modenumber, and the second uses a large one. The runs are
920 otherwise identical: both simulations use the quiet dayside ionospheric profile, and both
921 are driven at 22 mHz.

922 The differences between the two runs are striking. At low modenumber, wave activity
923 is visible throughout the simulation domain. Structure in the poloidal magnetic field is
924 only vaguely governed by the dipole geometry, and the compressional magnetic field is
925 comparably strong to the two perpendicular components.

926 In contrast, at high modenumber, the poloidal magnetic field is localized to the L -shells
927 where the driving is delivered: $4 \lesssim L \lesssim 6$. The compressional field is weaker than
928 the poloidal field by at least an order of magnitude. A third-harmonic poloidal mode
929 is visible at the outer boundary — its magnitude is just barely large enough to be
930 visible on the logarithmic scale. The gap between $L \sim 5$ (where 22 mHz matches a first-
931 harmonic FLR) and $L \sim 10$ (where 22 mHz matches a third-harmonic FLR) speaks to
932 the evanescence of non-guided waves above the compressional Alfvén cutoff frequency¹.

933 In both the low- m and high- m runs, toroidal activity is more or less coincident with
934 poloidal activity — as is to be expected, since the driving is purely poloidal, and the
935 poloidal mode rotates to the toroidal mode over time. It is further notable that the
936 toroidal mode is sharply guided. Particularly in Figure 7.2, strong, narrow, toroidal
937 FLRs of opposite phase can be seen oscillating very close to one another. Strong poloidal
938 waves, in contrast, are smeared in L .

939 Snapshots are not shown for runs carried out using the other ionospheric profiles (active
940 day, quiet night, and active night). The morphology of their waves is qualitatively
941 similar. The differences between the profiles is considered in Sections 7.2 to 7.4.

942 Figure 7.3 quantifies the compressional component of the poloidal mode as a function of
943 modenumber. Each subplot corresponds to a different run of Tuna — the runs shown in
944 Figures 7.1 and 7.2 are in the rightmost column, second from the top and second from the
945 bottom respectively. The red line indicates the ratio between the RMS compressional
946 magnetic field and the RMS poloidal magnetic field; both averages are taken over the
947 entire simulation “volume” each time step. Mean values are shown in black.

¹See Section 4.4.

- 948 At $m = 1$, the compressional and poloidal magnetic fields are comparable in magnitude.
949 As m increases, however, the compressional component quickly falls off. The compres-
950 sional component is half the strength of the poloidal component at $m \sim 5$, and a quarter
951 by $m \sim 10$.
- 952 A slight frequency dependence is apparent across each row in Figure 7.3. Compressional
953 coupling falls off slower for waves at higher frequency. This is because higher-frequency
954 waves are that much closer to the cutoff frequency (described in Section 4.4), and so
955 their propagation across L -shells is that much less evanescent.
- 956 Similarly, poloidal waves are more prone to compression on the nightside. Due to the
957 higher Alfvén speed on the nightside, driving is delivered at $L \sim 6$ instead of $L \sim 5$. The
958 cutoff frequency depends inversely on radial distance. For nightside runs (not shown),
959 $\left| \frac{B_z}{B_x} \right|$ falls to 50% at $m \sim 8$ and to 25% at $m \sim 16$.
- 960 Notably, the waves considered in the present work are fundamental harmonics. The
961 compressional behavior of the poloidal mode may vary for the (more-common) second
962 harmonic: Radoski suggests that the asymptotic value of $\left| \frac{B_z}{B_x} \right|$ is inversely proportional
963 to the harmonic number[78].

Magnetic Field Snapshots: Quiet Day , 22mHz Current, $m = 2$

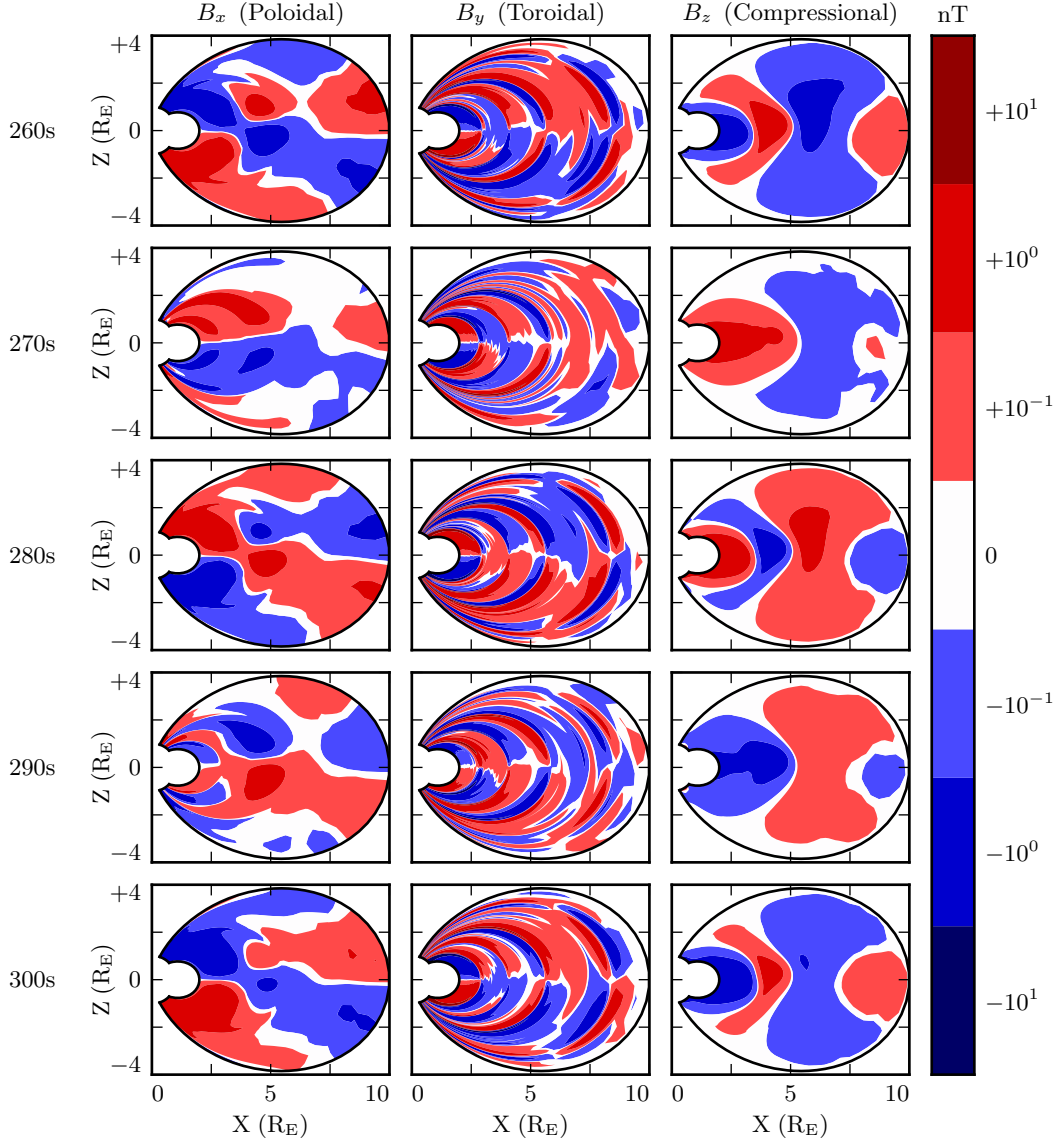


Figure 7.1: Each row in the above figure is a snapshot in time. The three columns show the simulated poloidal, toroidal, and compressional magnetic field. Due to the run's low azimuthal modenumber, the poloidal mode has a significant compressional component. This is visible both in the fact that B_z is comparable in size to B_x , and in that structure in B_x is only vaguely guided by the geometry of the magnetic field. Toroidal waves, in contrast, are sharply guided.

Magnetic Field Snapshots: Quiet Day , 22mHz Current, $m = 32$

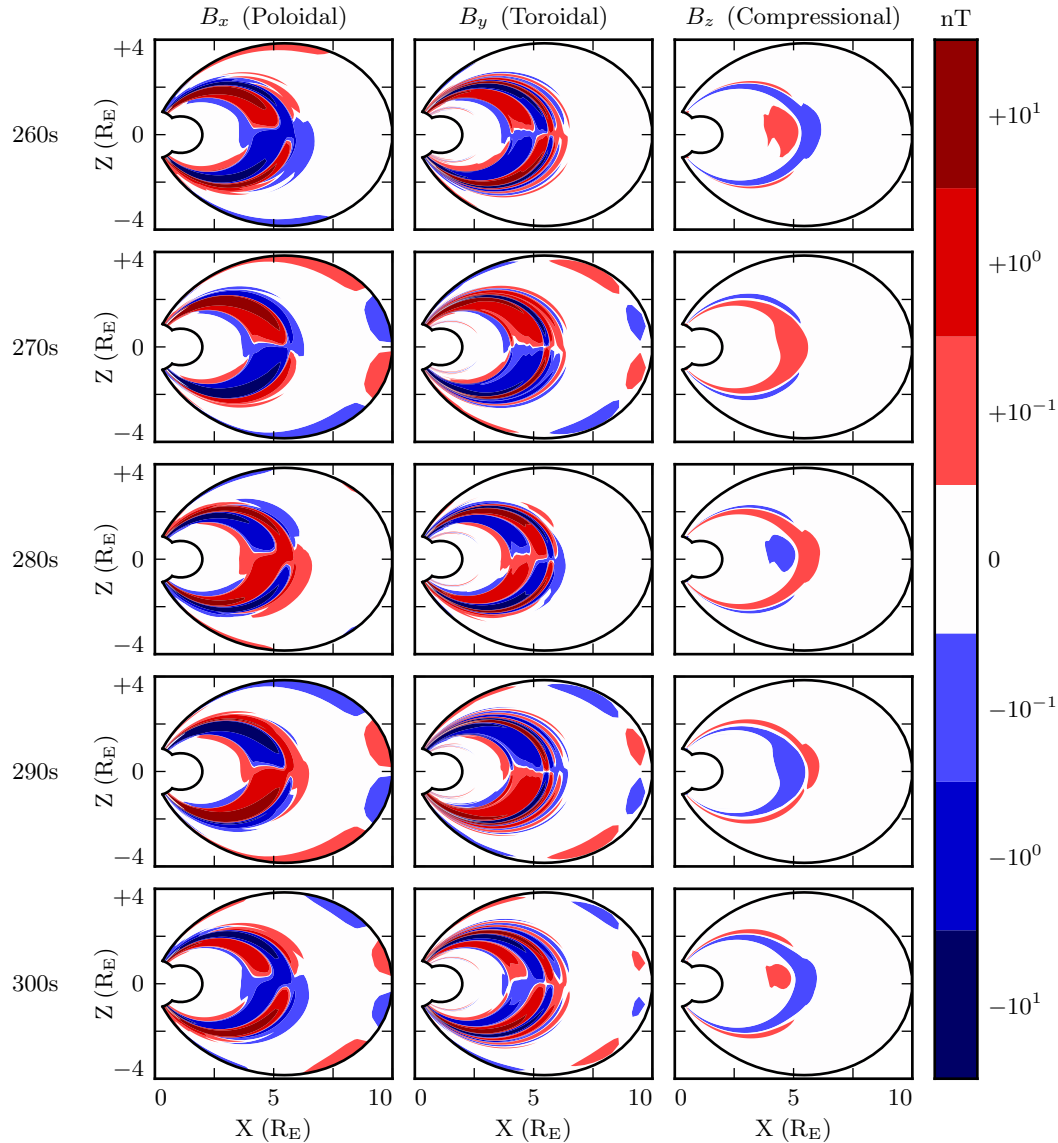


Figure 7.2: The above figure is analogous to Figure 7.1, but the runs use a larger azimuthal modenumber. The change has a dramatic effect. The poloidal wave is concentrated much more sharply in L , and its compressional component is weaker by an order of magnitude. Regardless of modenumber, toroidal waves exist at a range of L shells similar to poloidal waves, and show sharp definition across L -shells.

Compressional Coupling to the Poloidal Mode: Quiet Day

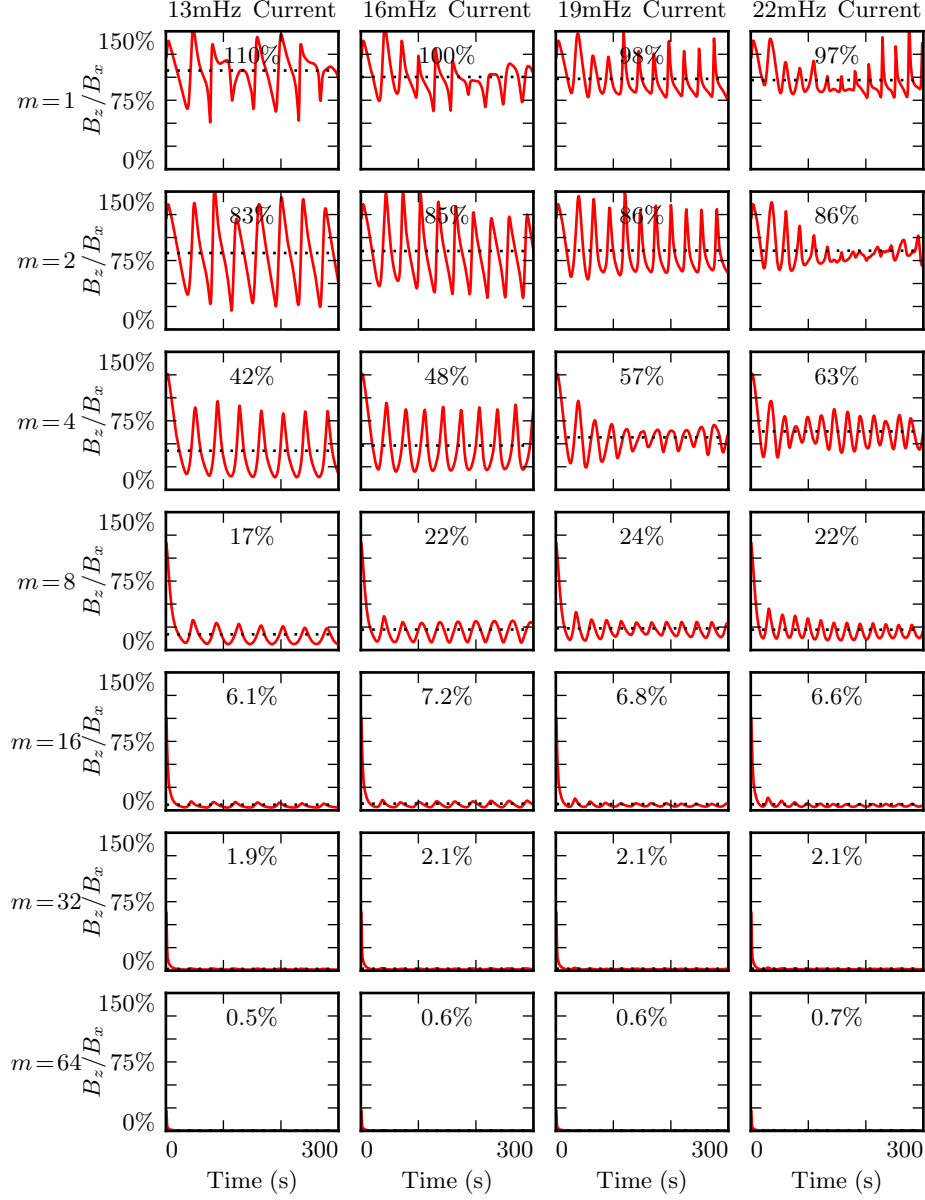


Figure 7.3: Each subplot above corresponds to a different run; the runs shown in Figures 7.1 and 7.2 are in the rightmost column, second from the top and second from the bottom respectively. Red lines indicate the ratio between the RMS compressional and poloidal magnetic fields. Mean values are shown in black. The compressional field is comparable to the poloidal field at $m = 1$, but falls quickly.

964 **7.2 Resonance and Rotation on the Dayside**

- 965 In his 1974 paper, Radoski argues that a poloidally-polarized wave should asymptoti-
966 cally rotate to the toroidal polarization[78] as a result of the curved derivative in the
967 meridional plane. The question of finite poloidal lifetimes is considered further in a 1995
968 paper by Mann and Wright[64]. Their numerical work used a straightened field line,
969 with an Alfvén speed gradient in the “radial” direction. They also found a rotation over
970 time from poloidal to toroidal polarization, with the characteristic time proportional to
971 the azimuthal modenumber.
- 972 The present section builds on the aforementioned results by relaxing several of their non-
973 physical assumptions. Tuna’s geometry is more realistic than Radoski’s half-cylinder or
974 the box model used by Mann and Wright. Previous work has considered the evolu-
975 tion of an initial condition, while the simulations shown below include driving delivered
976 over time. In addition, Tuna features a finite, height-resolved ionospheric conductivity
977 profile, rather than the perfectly-reflecting boundaries used in the past.

Each subplot in Figure 7.4 is analogous to Figure 3 in Mann and Wright’s paper[64]. Blue lines show the total energy in the poloidal mode as a function of time. Red lines show toroidal energy. Runs are organized analogous to those in Figure 7.3: drive frequency is constant down each column, and azimuthal modenumber is constant across each row. Axis bounds are held constant across all subplots. The poloidal and toroidal energy are computed by integrating over the electromagnetic energy density, per Poynting’s theorem:

$$U_P = \int \frac{dV}{2\mu_0} \left(B_x^2 + \frac{1}{v_A^2} E_y^2 \right) \quad U_T = \int \frac{dV}{2\mu_0} \left(B_y^2 + \frac{1}{v_A^2} E_x^2 \right) \quad (7.1)$$

- 978 Where the differential volume dV is computed using the Jacobian² to account for Tuna’s
979 unusual geometry. The integral is evaluated in u^1 and u^3 but not u^2 (Tuna’s missing
980 half-dimension), which gives energy in units of gigajoule per radian. More than anything
981 else, this serves as a reminder that Pc4 pulsations are localized in MLT.

²See Section 5.1.

982 The 28 runs shown in Figure 7.4 use an ionospheric profile corresponding to the dayside
983 during times of low solar activity, where the conductivity is relatively high. The active
984 and quiet dayside profiles are briefly contrasted in Section 7.4; for the most part, the
985 focus of the present work is on the difference between the dayside and the nightside
986 (Section 7.3). Differences between the two dayside profiles are small in comparison.

987 The fact that red (toroidal) lines appear at all in Figure 7.4 speaks to a net rotation
988 of energy from the poloidal mode to the toroidal. As discussed in Section 5.3, Tuna’s
989 driving is delivered purely into the poloidal electric field (reflecting a perturbation in
990 the magnitude of the ring current).

991 As expected, the rotation from poloidal to toroidal is slowest at large azimuthal mode-
992 numbers. The toroidal energy overtakes the poloidal energy within a single drive period
993 at $m = 4$; at $m = 64$, the most of the energy is in the poloidal mode for ~ 10 periods.
994 However, the relationship between azimuthal modenumber and rotation timescale is
995 not linear, as was suggested by Mann and Wright. Instead, in a practical setting, the
996 rotation is fastest at $m \sim 4$.

997 This is explained by the compressional character of the poloidal mode. At very low
998 modenumber, energy in the poloidal mode moves readily across L -shells. A significant
999 fraction of that energy is lost to the outer boundary before rotating to the toroidal
1000 mode. At high modenumber — as discussed in Section 7.1 — compressional propagation
1001 is evanescent, so all energy in the poloidal mode must ultimately rotate to the toroidal
1002 mode or be lost to Joule dissipation.

1003 Joule dissipation is a major player in the system’s energy economy. However, due to the
1004 highly conductive dayside ionosphere, dissipation timescales are in the tens of Pc4 wave
1005 periods. Energy loss through Joule dissipation asymptotically balances energy input
1006 from driving, but most of that energy is not lost until after it has rotated from the
1007 poloidal mode to the toroidal. As such, in most runs shown in Figure 7.4, the energy
1008 content of the toroidal mode asymptotically exceeds that of the poloidal mode.

1009 The asymptotic energy content of the system also depends on how well the drive fre-
1010 quency matches the local eigenfrequency. If the two do not match, energy is lost to
1011 destructive interference between the standing wave and the driving.

1012 In principle, energy moves between the poloidal and toroidal modes due to their direct
1013 coupling through the ionospheric Hall conductivity. In practice, this effect is small.
1014 When the runs shown in Figure 7.4 are repeated with the Hall conductivity set to zero,
1015 the resulting energy curves are not visibly different.

1016 The low- m runs at 19 mHz merit additional discussion. These runs accumulate energy
1017 over a large number of wave periods, while the low- m waves at 13 mHz, 16 mHz, and
1018 22 mHz do not. This effect is likely nonphysical. At 19 mHz, a third-harmonic resonance
1019 forms very close to the outer boundary. The resonance is likely enhanced by nonphysical
1020 reflections against the simulation’s boundary conditions.

1021 The presence of individual harmonics can be seen in the contours shown in Figures 7.5
1022 and 7.6. These figures show the same runs as Figure 7.4, arranged in the same way on
1023 the page. However, instead of showing the total energy integrated over the simulation
1024 domain, the energy densities are averaged over the volume of each flux tube individually.
1025 Figure 7.5 shows contours of poloidal energy density and Figure 7.6 shows toroidal
1026 energy density.

1027 The top few rows of Figure 7.5 confirm that the poloidal mode’s compressional nature is
1028 to blame for its failure to accumulate energy at low modenumber. Waves move so readily
1029 across field lines that no visible amount of energy builds up at $L \sim 5$, the location of the
1030 driving. Some energy moves inward, and is trapped by the peak in Alfvén speed just
1031 inside the plasmapause, while the rest moves to the outer boundary. The time spent
1032 moving across field lines counts against the poloidal mode’s finite lifetime, inhibiting
1033 the buildup of poloidal energy density even at L -shells where the wave matches the local
1034 eigenfrequency.

1035 As m increases, the energy distribution becomes more concentrated in L , though indi-
1036 vidual features remain fairly broad. At $m = 8$, runs at 13 mHz and 16 mHz are inclined
1037 to build up energy just inside the plasmapause, while those at 19 mHz and 22 mHz res-
1038 onate just outside the plasmapause; in all four cases, the energy is spread over a range
1039 of at least 1 in L .

1040 The peak energy density in the bottom-right run (22 mHz driving, $m = 64$) is by far the
1041 largest of any run in Figure 7.5. The azimuthal modenumber is large, so the poloidal

1042 mode is purely guided; energy is not smeared across multiple L -shells. And, crucially, the
1043 frequency of the driving matches closely with the Alfvén frequency at $L \sim 5$. Other runs
1044 on the bottom row are also guided, but they reach lower asymptotic energy densities
1045 because of a mismatch between the drive frequency and the local eigenfrequency —
1046 resulting in destructive interference between the standing wave and its driver.

1047 The eigenfrequencies in the magnetosphere are significantly affected by the location of
1048 the plasmapause. When the runs in Figure 7.5 are repeated with the plasmapause at
1049 $L = 5$ instead of $L = 4$, the strongest resonance at $L \sim 5$ drops from 22 mHz to 16 mHz
1050 (not shown).

1051 Whereas the poloidal contours are smeared over a swath of L -shells (though the high- m
1052 runs less so), the toroidal contours in Figure 7.6 appear only where the wave frequency
1053 matches the local eigenfrequency. A horizontal line drawn through the Alfvén speed
1054 frequency profiles (recall Figure 3.1) intersects the profile up to three times: once as
1055 the Alfvén frequency drops through the Pc4 range from its low-latitude peak, again as
1056 the Alfvén frequency rises sharply at the plasmapause, and a third time as the Alfvén
1057 frequency drops asymptotically. Toroidal waves can be seen resonating at all three of
1058 these locations in the $m = 4$, 22 mHz run in Figure 7.6, along with a third harmonic at
1059 large L . This is consistent with observations: toroidal resonances are noted for having
1060 frequencies which depend strongly on L , in contrast to the poloidal mode's less-strict
1061 relationship between frequency and location.

1062 In only one of the runs shown in Figure 7.5 does the poloidal mode attain an energy
1063 density on the order of 10^{-1} nJ/m³. On the other hand, the toroidal mode reaches
1064 $\sim 10^{-1}$ nJ/m³ in six of the runs in Figure 7.6. That is, the poloidal mode only exhibits
1065 a high energy density on the dayside only when conditions are ideal; the toroidal mode
1066 isn't nearly so particular.

Poloidal (Blue) and Toroidal (Red) Energy: Quiet Day

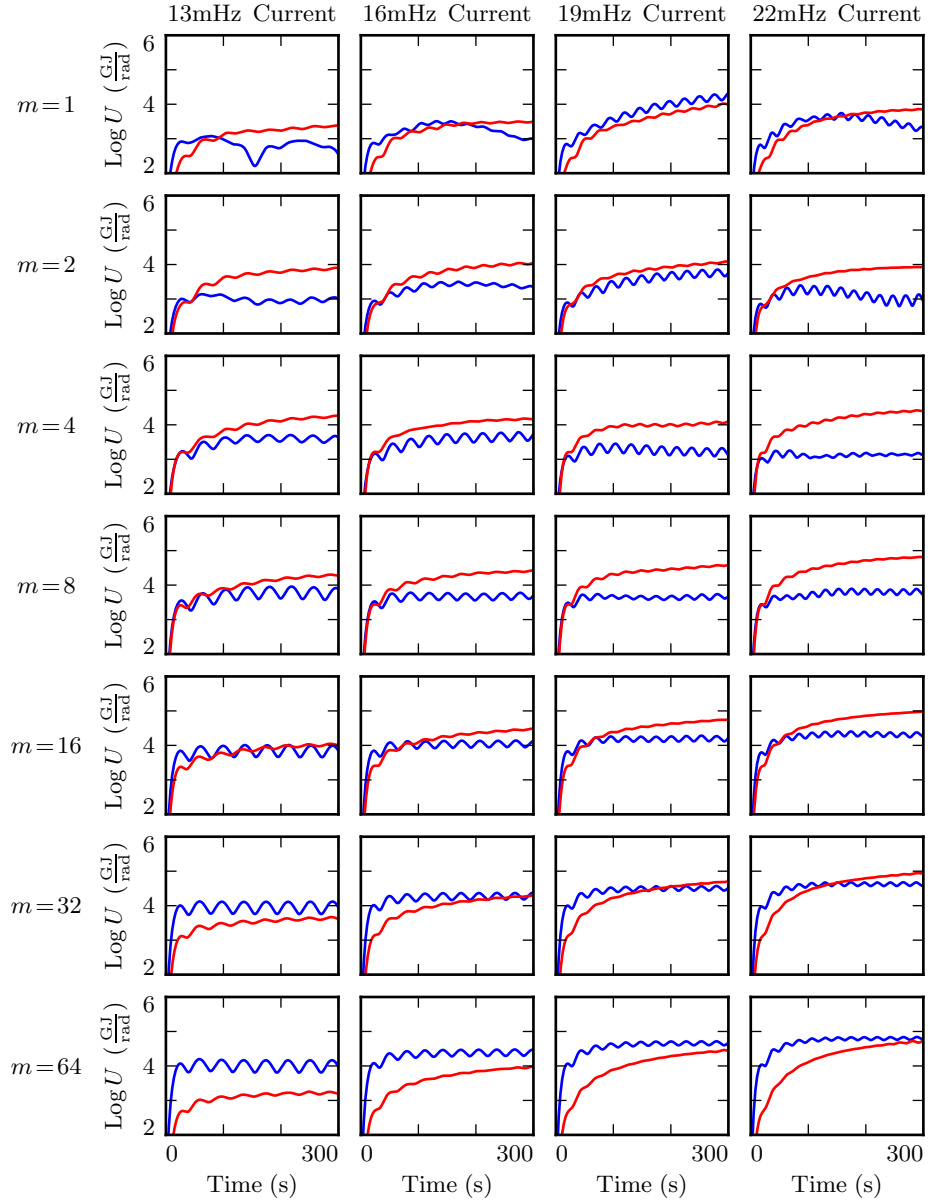


Figure 7.4: TODO: Lorem ipsum dolor sit amet, consectetur adipiscing elit, sed do eiusmod tempor incididunt ut labore et dolore magna aliqua. Ut enim ad minim veniam, quis nostrud exercitation ullamco laboris nisi ut aliquip ex ea commodo consequat. Duis aute irure dolor in reprehenderit in voluptate velit esse cillum dolore eu fugiat nulla pariatur.

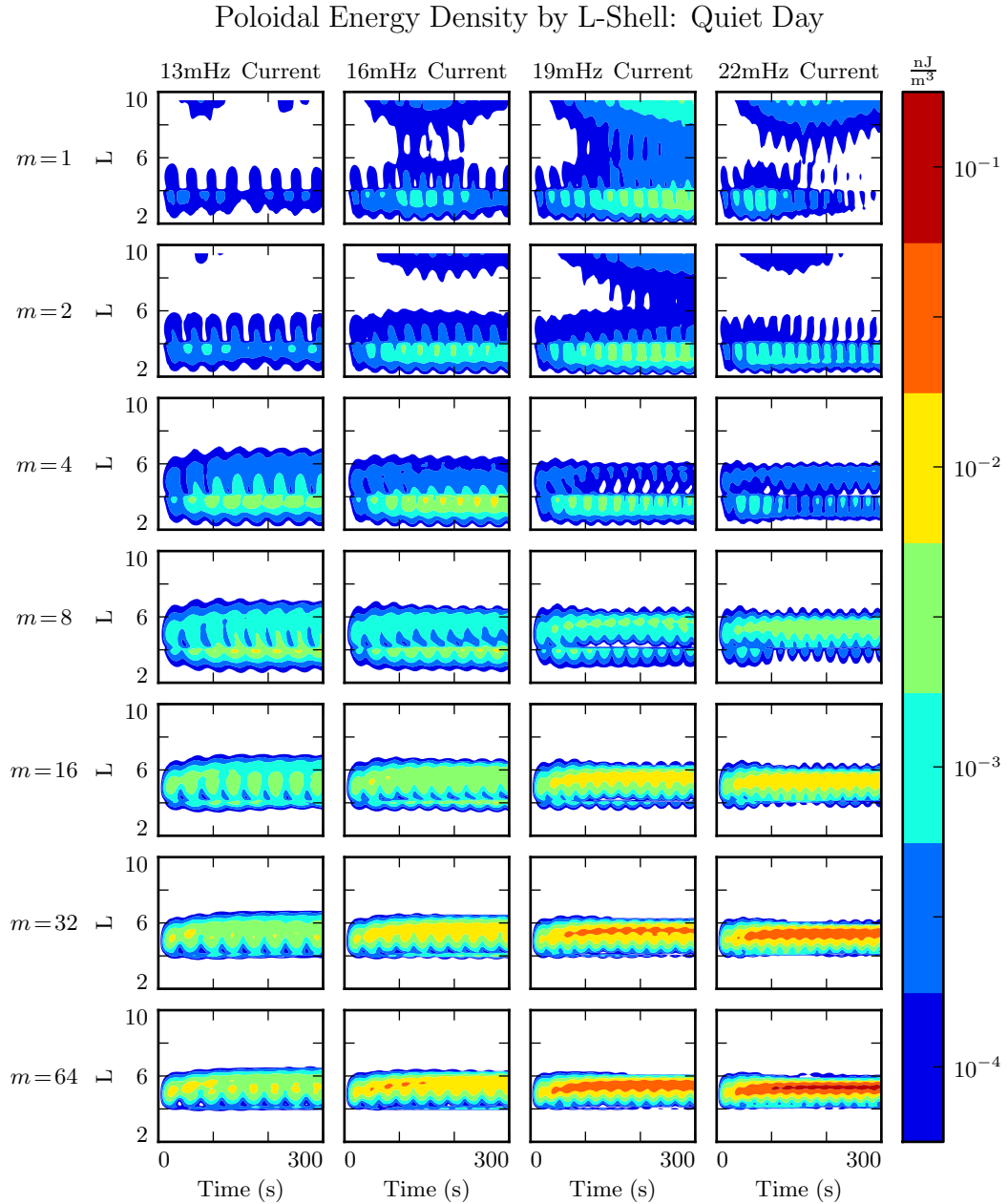


Figure 7.5: TODO: Lorem ipsum dolor sit amet, consectetur adipiscing elit, sed do eiusmod tempor incididunt ut labore et dolore magna aliqua. Ut enim ad minim veniam, quis nostrud exercitation ullamco laboris nisi ut aliquip ex ea commodo consequat. Duis aute irure dolor in reprehenderit in voluptate velit esse cillum dolore eu fugiat nulla pariatur.

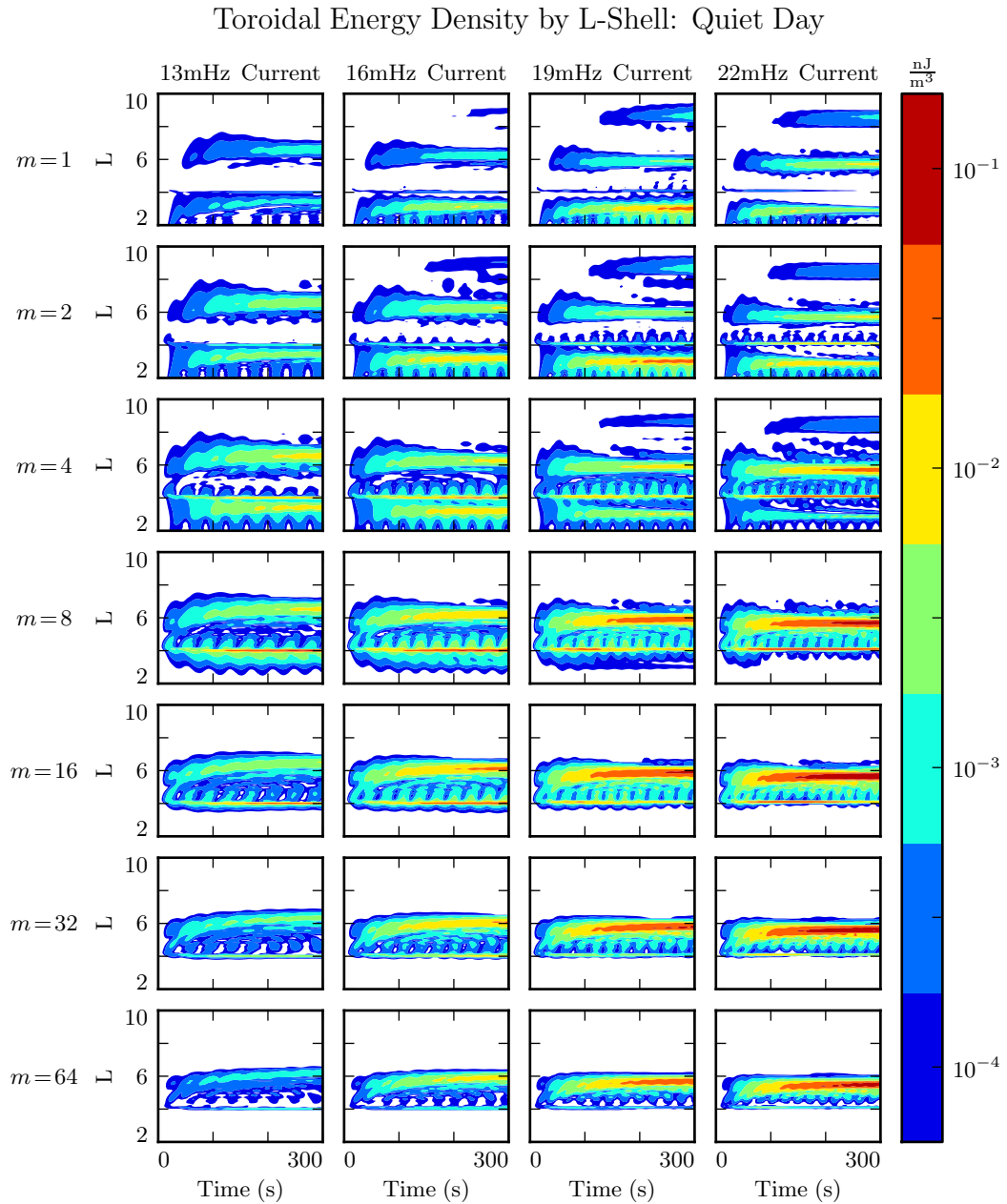


Figure 7.6: TODO: Lorem ipsum dolor sit amet, consectetur adipiscing elit, sed do eiusmod tempor incididunt ut labore et dolore magna aliqua. Ut enim ad minim veniam, quis nostrud exercitation ullamco laboris nisi ut aliquip ex ea commodo consequat. Duis aute irure dolor in reprehenderit in voluptate velit esse cillum dolore eu fugiat nulla pariatur.

1067 7.3 Resonance and Rotation on the Nightside

1068 Compared to the dayside ionosphere employed in Section 7.2, the nightside exhibits
1069 two major differences. The ionospheric conductivity is lower, and the Alfvén speed is
1070 higher. As a result of the higher Alfvén speed, driving on the nightside is delivered at
1071 $L \sim 6$ instead of $L \sim 5$. Runs in the present section specifically use Tuna’s ionospheric
1072 profile corresponding to the nightside during quiet solar conditions; the active nightside
1073 is discussed briefly in Section 7.4, but for the most part the present work is concerned
1074 with the behavior of the nightside compared to that on the dayside.

1075 Other than the change in ionospheric profile, Figures 7.7 to 7.9 are analogous to Fig-
1076 ures 7.4 to 7.6. Each subplot corresponds to a different 300 s run of Tuna. Drive
1077 frequency is constant down each column, and azimuthal modenumber is constant across
1078 each row.

1079 The low conductivity on the nightside gives rise to strong Joule dissipation. Waves are
1080 damped out in just a few bounces, so asymptotic energy values are reached quickly.
1081 No combination of frequency and modenumber gives rise to the accumulation of energy
1082 over multiple drive periods.

1083 As on the dayside, rotation of energy from the poloidal to toroidal mode is fastest at
1084 $m \sim 4$. Unlike the dayside, however, dissipation on the nightside is fast compared to
1085 the rotation of energy to the toroidal mode. Toroidal energy does not asymptotically
1086 exceed the poloidal energy by a significant margin in any run. At $m = 64$, where the
1087 rotation timescale is slowest, no more than 1088 TODO: \dots of the energy in the poloidal
mode rotates to the toroidal mode before being lost.

1089 1090 TODO: The damping on the quiet nightside is so severe that basically nothing resonates
anywhere. Should we show the active nightside instead?

Poloidal (Blue) and Toroidal (Red) Energy: Quiet Night

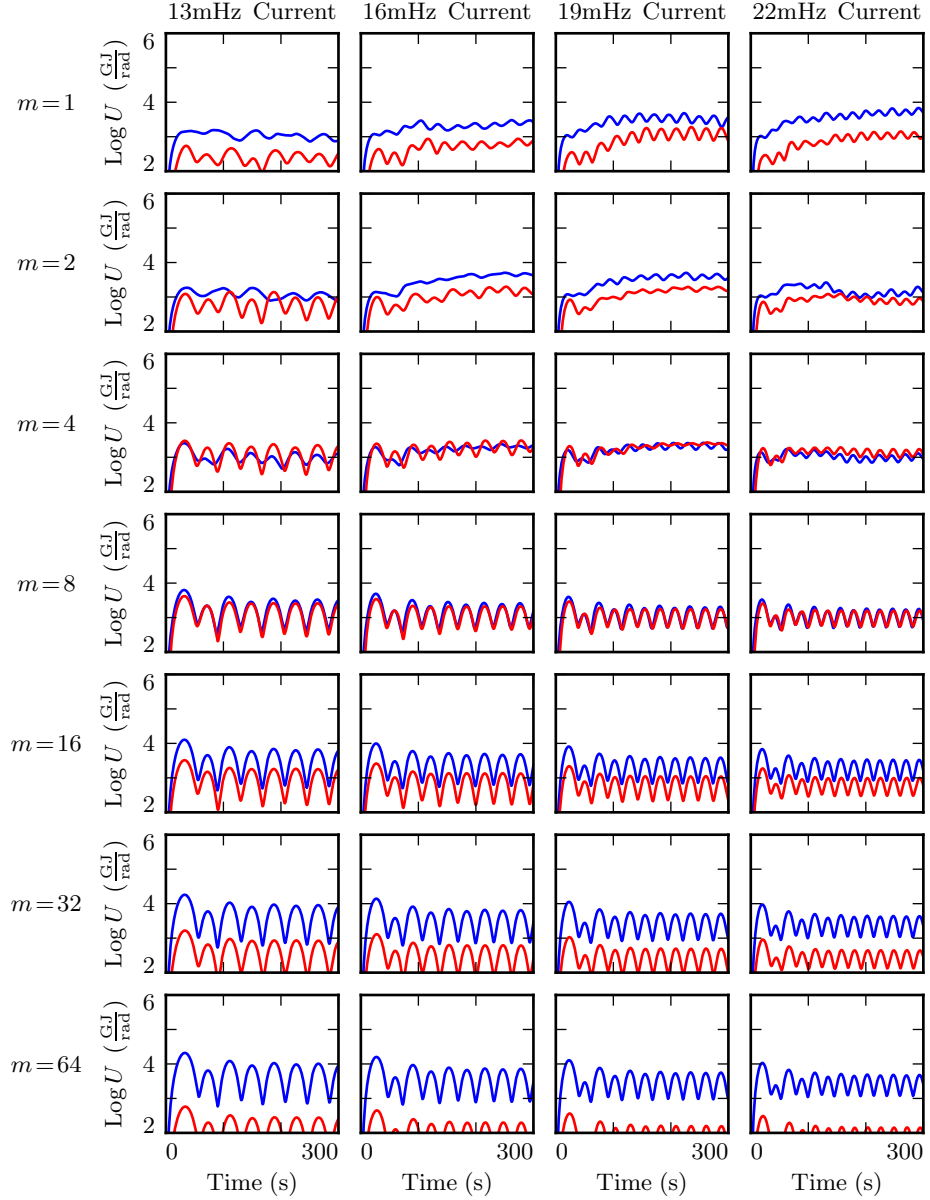


Figure 7.7: TODO: Lorem ipsum dolor sit amet, consectetur adipiscing elit, sed do eiusmod tempor incididunt ut labore et dolore magna aliqua. Ut enim ad minim veniam, quis nostrud exercitation ullamco laboris nisi ut aliquip ex ea commodo consequat. Duis aute irure dolor in reprehenderit in voluptate velit esse cillum dolore eu fugiat nulla pariatur.

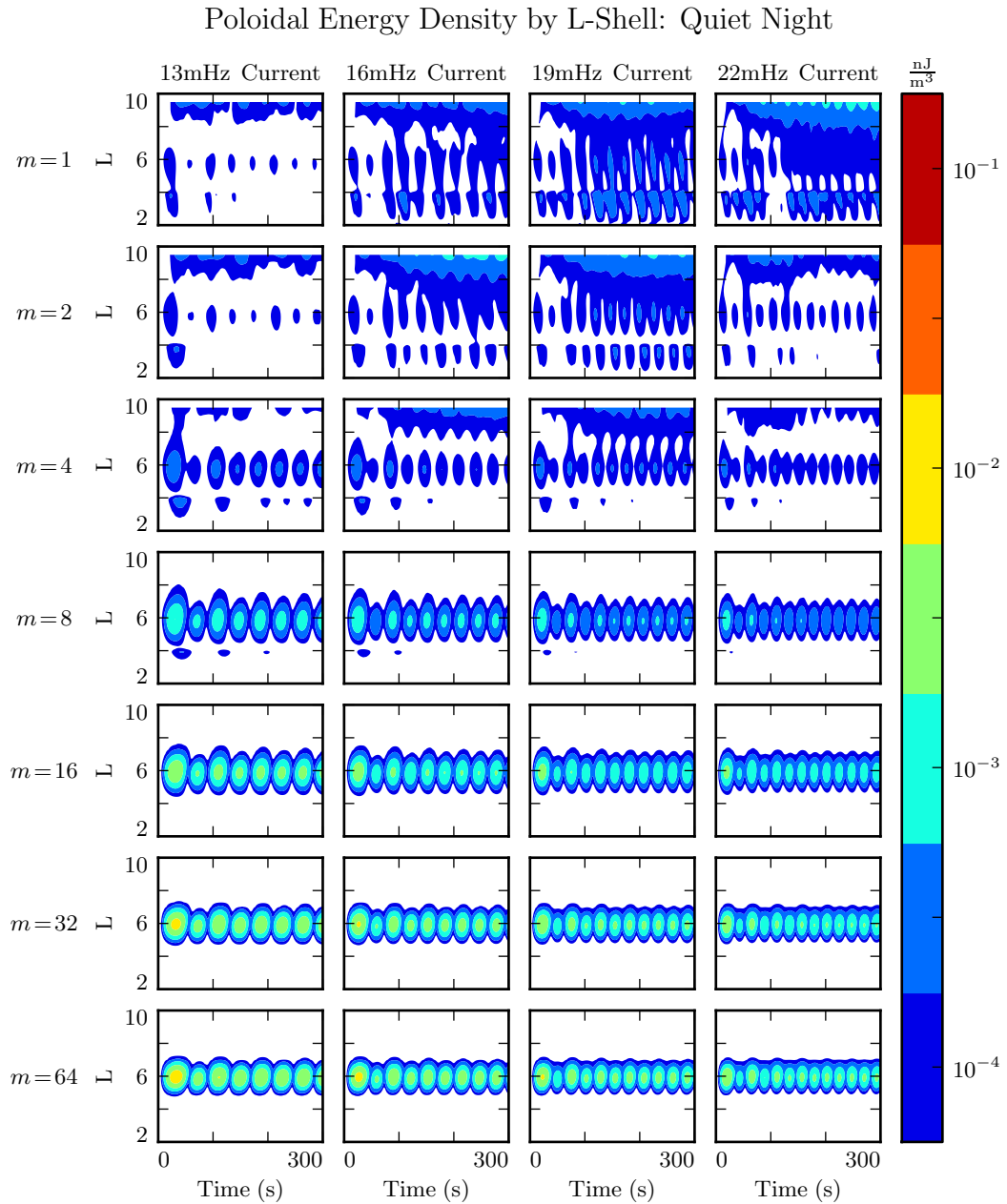


Figure 7.8: TODO: Lorem ipsum dolor sit amet, consectetur adipiscing elit, sed do eiusmod tempor incididunt ut labore et dolore magna aliqua. Ut enim ad minim veniam, quis nostrud exercitation ullamco laboris nisi ut aliquip ex ea commodo consequat. Duis aute irure dolor in reprehenderit in voluptate velit esse cillum dolore eu fugiat nulla pariatur.

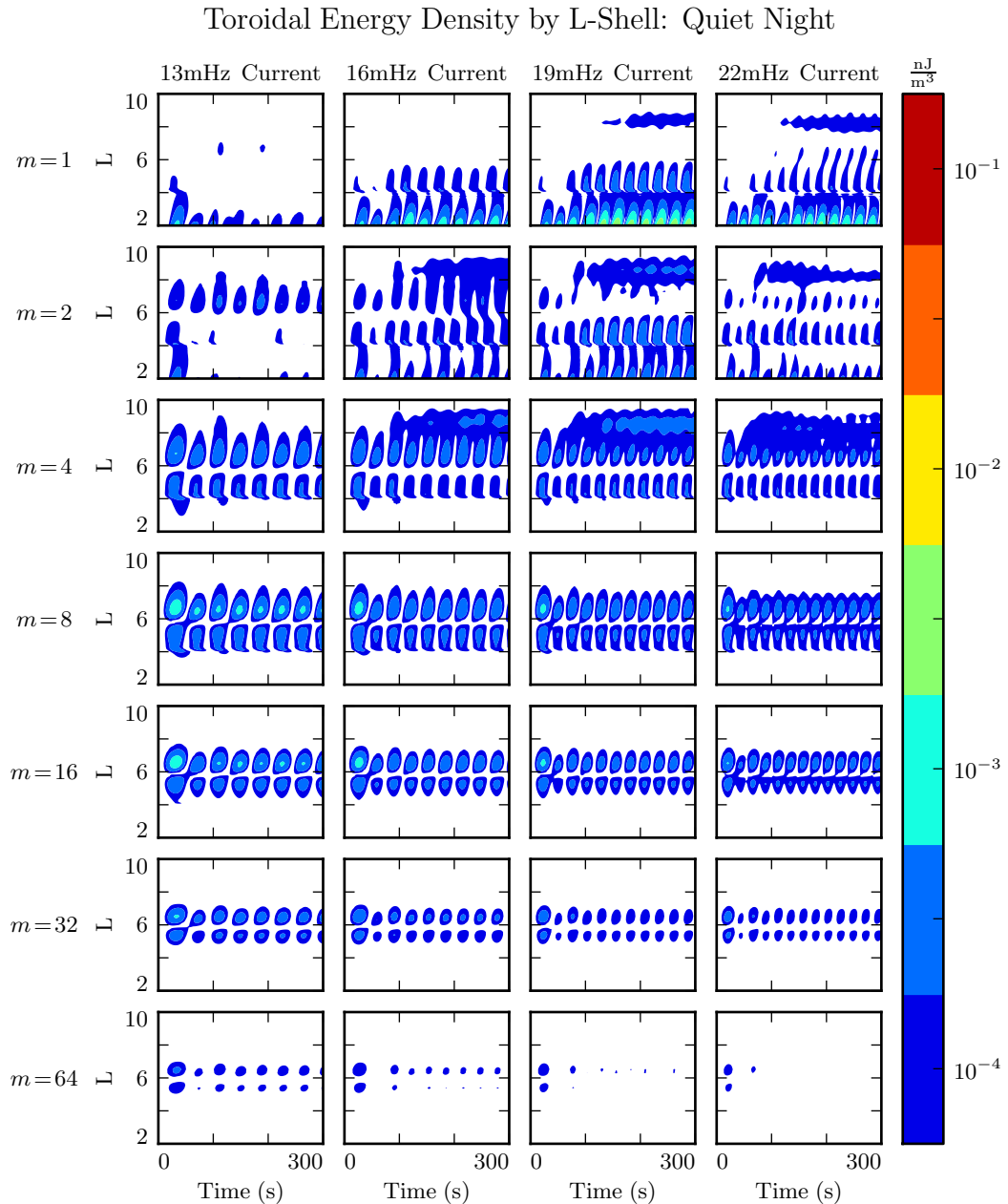


Figure 7.9: TODO: Lorem ipsum dolor sit amet, consectetur adipiscing elit, sed do eiusmod tempor incididunt ut labore et dolore magna aliqua. Ut enim ad minim veniam, quis nostrud exercitation ullamco laboris nisi ut aliquip ex ea commodo consequat. Duis aute irure dolor in reprehenderit in voluptate velit esse cillum dolore eu fugiat nulla pariatur.

1091 7.4 Ground Signatures and Giant Pulsations

1092 While the majority of the action is in space, the majority of FLR observations have
1093 historically been ground-based. The present section explores the same simulations dis-
1094 cussed in Sections 7.2 and 7.3, but in terms of their ground signatures rather than their
1095 broad energy distributions.

1096 As in the figures shown in Sections 7.2 and 7.3, each row in Figures 7.10 and 7.11 shows
1097 runs at a different modenumber. The columns are magnetic field contours; the vertical
1098 axis is latitude, and the horizontal axis is time. The four columns are components of
1099 the magnetic field signatures at the ground: the north-south magnetic field (first and
1100 third columns) and the east-west magnetic field (second and fourth columns). The pair
1101 on the left show a simulation carried out using the active ionospheric profile, and the
1102 pair on the right show a simulation using the quiet profile.

1103 Notably, the magnetic polarization of a low frequency Alfvén wave is rotated by $\sim 90^\circ$ as
1104 it passes through the ionosphere[41]. The east-west field on the ground (B_ϕ) corresponds
1105 to the poloidal polarization in space, and the north-south field on the ground (B_θ)
1106 corresponds to the toroidal mode.

1107 The most striking feature of Figures 7.10 and 7.11 is the modenumber dependence.
1108 As modenumber increases, the magnetic field signatures become sharply localized in
1109 latitude. At high m , ground signatures are concentrated between 60° and 70° , peaking
1110 near 64° on the dayside and 66° on the nightside. Appropriately enough, these latitudes
1111 lie at the $L \sim 5$ and $L \sim 6$ respectively.

1112 **TODO: Is it weird that we see no ducting from the ionosphere? Does the ionosphere**
1113 **duct ULF waves in the θ direction, or just in ϕ ?**

1114 At low modenumber, magnetic signatures are weak on the ground because the waves
1115 in space are also weak. At high modenumber, waves in space are strong, but so is
1116 the attenuation of magnetic signatures by the ionosphere³. The “sweet spot” at which
1117 magnetic ground signatures are maximized falls at $m = 16$ to $m = 32$.

3See Equation (3.2).

1118 Tuna shows stronger ground signatures on the dayside than on the nightside, more or
1119 less in proportion with the difference in magnitude in space. Energy on the dayside
1120 (which depends on field magnitude squared) peaks an order of magnitude larger than
1121 that on the nightside. Peak ground signatures on the dayside are larger by a factor of
1122 five: 45 nT compared to 10 nT. On both the dayside and the nightside, peak ground
1123 signatures are in B_ϕ , the east-west magnetic field component; both are also at $m = 16$,
1124 and both are seen in runs using the ionospheric profile for quiet solar activity.

1125 **TODO:** Check the other frequencies to make sure these are the real maxima. Probably
1126 also should print the maximum magnitude at the bottom of the subplot.

1127 These results match well with observations of giant pulsations, which tend to be east-
1128 west polarized, and are most often observed near 66° , with azimuthal modenumbers
1129 of 16 to 35, at the bottom of the solar cycle[92]. Pgs are most commonly observed
1130 pre-dawn, but dawn and dusk ionospheric profiles are not implemented for Tuna at
1131 present.

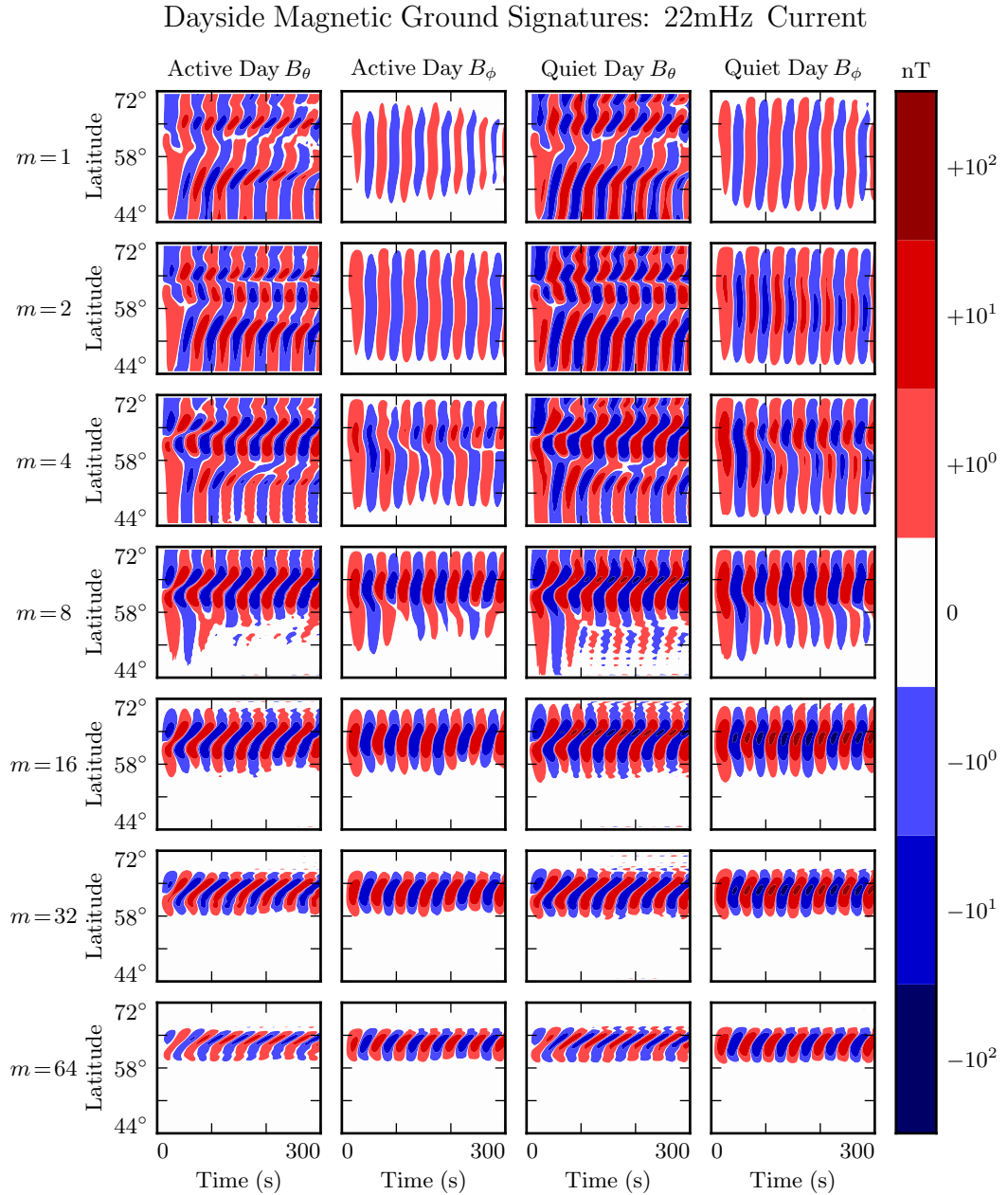


Figure 7.10: TODO: Lorem ipsum dolor sit amet, consectetur adipiscing elit, sed do eiusmod tempor incididunt ut labore et dolore magna aliqua. Ut enim ad minim veniam, quis nostrud exercitation ullamco laboris nisi ut aliquip ex ea commodo consequat. Duis aute irure dolor in reprehenderit in voluptate velit esse cillum dolore eu fugiat nulla pariatur.

Nightside Magnetic Ground Signatures: 13mHz Current

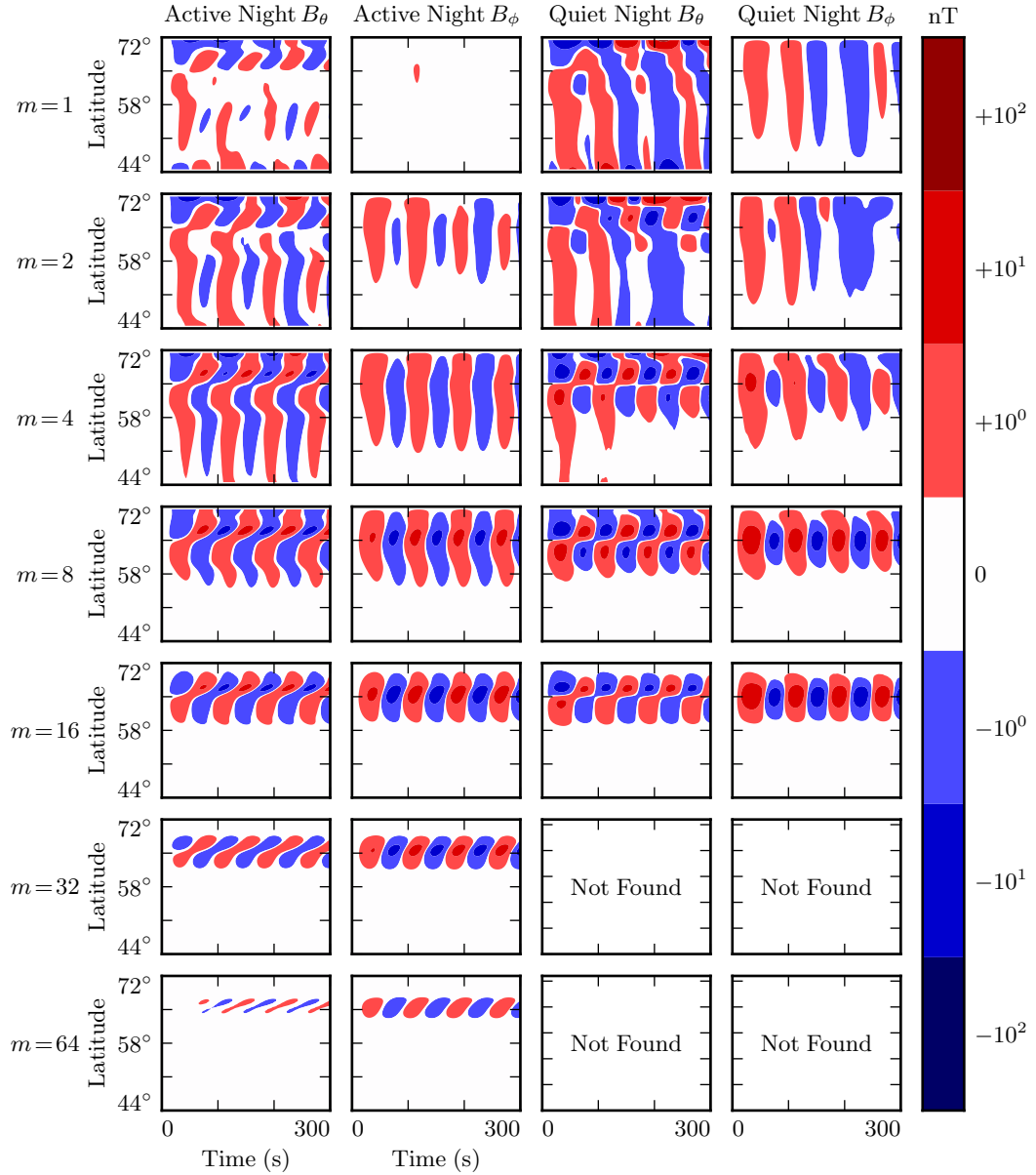


Figure 7.11: Nightside ground signatures are less strongly peaked than those on the dayside, but qualitative features are the same: the strongest signals are in B_ϕ , peaked over just a few degrees in latitude, at a modenumber of 16 or 32, under quiet ionospheric conditions.

1132 **7.5 Discussion**

1133 **TODO:** Make this section read nicely.

1134 Poloidal FLRs rotate to the toroidal mode over time. Toroidal modes do not appear to
1135 rotate back to the poloidal mode. When m is small, the rotation is comparable to an
1136 oscillation period; when m is large, rotation timescales are comparable to ten periods,
1137 sometimes more.

1138 On the dayside, little damping takes place over rotation timescales, so the toroidal mode
1139 asymptotically exceeds the toroidal mode. The exception is waves with low modenumber,
1140 where poloidal waves can escape by propagating across field lines. An evaluation
1141 of what happens then — whether they bounce back off the magnetopause, for example
1142 — is beyond the scope of the present work.

1143 On the nightside, the conductivity of the ionosphere is low enough that damping
1144 timescales become comparable to oscillation timescales. Waves are weaker, since they
1145 are unable to accumulate energy over as many periods. High- m toroidal waves are
1146 particularly weak, since the dissipation timescale is faster than the poloidal-to-toroidal
1147 rotation timescale.

1148 Waves resonate best when the frequency of the driving matches the local eigenfrequency
1149 where it's delivered. The eigenfrequency is significantly affected by the size of the
1150 plasmasphere.

1151 The poloidal mode, due to its compressional character, exhibits an energy profile which
1152 is smeared in L . The toroidal mode, on the other hand, forms sharp resonances where the
1153 drive frequency matches the local eigenfrequency. This may explain why the observed
1154 frequencies of poloidal waves depend weakly on L , while the frequencies of toroidal
1155 waves are strongly dependent on L .

1156 At low m , ground signatures are weak because waves in space are weak because energy
1157 can easily escape through the simulation's outer boundary. At large m , ground signatures
1158 are attenuated by the ionosphere. The “sweet spot” in azimuthal modenumber at
1159 which ground signatures are strongest is around 16 to 32. Furthermore, ground signatures
1160 are strongest when ionospheric profiles corresponding to solar minimum are used.

1161 Driving in the poloidal electric field gives rise to primarily ground signatures polarized
1162 primarily in the east-west direction at the ground. And, when the frequency of the
1163 driving does not match the local eigenfrequency, the high- m resonates weakly in place,
1164 rather than tunneling across field lines to resonate strongly somewhere else.

1165 These findings imply, awkwardly, that the morphology of giant pulsations may reveal
1166 relatively little about their origins. One can consider a hypothetical magnetosphere
1167 subject to constant driving: broadband in frequency, broadband in modenumber, just
1168 outside the plasmapause. Low- m poloidal waves will quickly rotate to the toroidal mode
1169 (and/or propagate away). High- m waves will resonate in place, accumulating energy
1170 over time, and giving rise to “multiharmonic toroidal waves”[89]; Fourier components
1171 that do not match the local eigenfrequency will quickly asymptote. Waves with very high
1172 modenumbers will be attenuated by the ionosphere. The response on the ground will be
1173 significantly stronger during quiet solar conditions. In other words, the measurements
1174 on the ground will look very much like a giant pulsation.

1175 **TODO:** Notably, the present work offers no explanation as to Pgs’ distinctive distribu-
1176 tion in MLT!

1177 **Chapter 8**

1178 **Observations**

1179 TODO: You know what would be great for putting this numerical work in context?
1180 A nice, consistent survey that breaks down the occurrence rate of Pc4 pulsations by
1181 harmonic, etc.

1182 TODO: The tools used in the present chapter — SPEDAS and the SPICE kernel —
1183 are publicly available. They run best with an IDL license, which is not, but they are
1184 functional using just the (free) IDL virtual machine. The code is wrapped up in a Git
1185 repository: <https://github.com/chizarlicious/RBSP> (maybe should make a GitHub
1186 organization to hold this code, to decouple it from my personal account?).

1187 **8.1 Sampling Bias and Event Selection**

1188 The present analysis makes use of all available Van Allen Probe data, which spans from
1189 October 2012 to August 2015. Between the two probes, that's just over 2000 days of
1190 observation.

1191 For the purposes of Pc4 pulsations, it's reasonable to consider the two probes to be
1192 independent observers. Nearly all Pc4 events occur near apogee ($L \gtrsim 5$), at which
1193 point the two probes are several hours apart in MLT. Pc4 events are typically not large

1194 enough to be seen by both probes simultaneously, and not long enough in duration to
1195 be seen by two probes passing through the same region of space several hours apart.

1196 **TODO: Quantify how often an event is seen by both probes?**

1197 Electric and magnetic field waveforms are collected using the probes' **TODO: ...** in-
1198 strument. Values are cleaned up by averaging over the ten-second spin period. Three-
1199 dimensional electric field data is then obtained using the $\underline{E} \cdot \underline{B} = 0$ assumption. Notably,
1200 this assumption is taken only when the probe's spin plane is offset from the magnetic
1201 field by at least 15° . The rest of the data — about half — is discarded, which introduces
1202 a sampling bias against the flanks.

1203 A further bias is introduced by the probes' non-integer number of precessions around
1204 Earth. As of July 2014, apogee had precessed once around Earth[17]. The present work
1205 considers roughly one and a half precessions; the nightside has been sampled at apogee
1206 twice as often as the dayside.

1207 The spatial distribution of usable data — that is, data for which three-dimensional
1208 electric and magnetic fields are available — is shown in Figure 8.1. Bins are unitary
1209 in L and in MLT. Event distribution in magnetic latitude is not shown; the Van Allen
1210 Probes are localized to within $\sim 10^\circ$ of the equatorial plane.

1211 **TODO: L is italicized and MLT is not? That seems weird.**

1212 Field measurements are transformed from GSE coordinates into the same dipole coor-
1213 dinates used in Chapters 5 and 7. The z axis is parallel to the background magnetic
1214 field, which is estimated using a ten-minute running average of the magnetic field mea-
1215 surements. The y axis is set parallel to $\hat{z} \times \underline{r}$, where \underline{r} is the probe's geocentric position
1216 vector. The x axis is then defined per $\hat{x} \equiv \hat{y} \times \hat{z}$. This scheme guarantees that the axes
1217 are right-handed and pairwise orthogonal[56].

1218 The ~ 1000 days of usable data are considered half an hour at a time, which gives a fre-
1219 quency resolution of ~ 0.5 mHz in the discrete Fourier transform. Spectra are computed
1220 for all six field components: \tilde{B}_x , \tilde{B}_y , \tilde{B}_z , \tilde{E}_x , \tilde{E}_y , and \tilde{E}_z . The background magnetic
1221 field is subtracted before transforming the magnetic field components, leaving only the

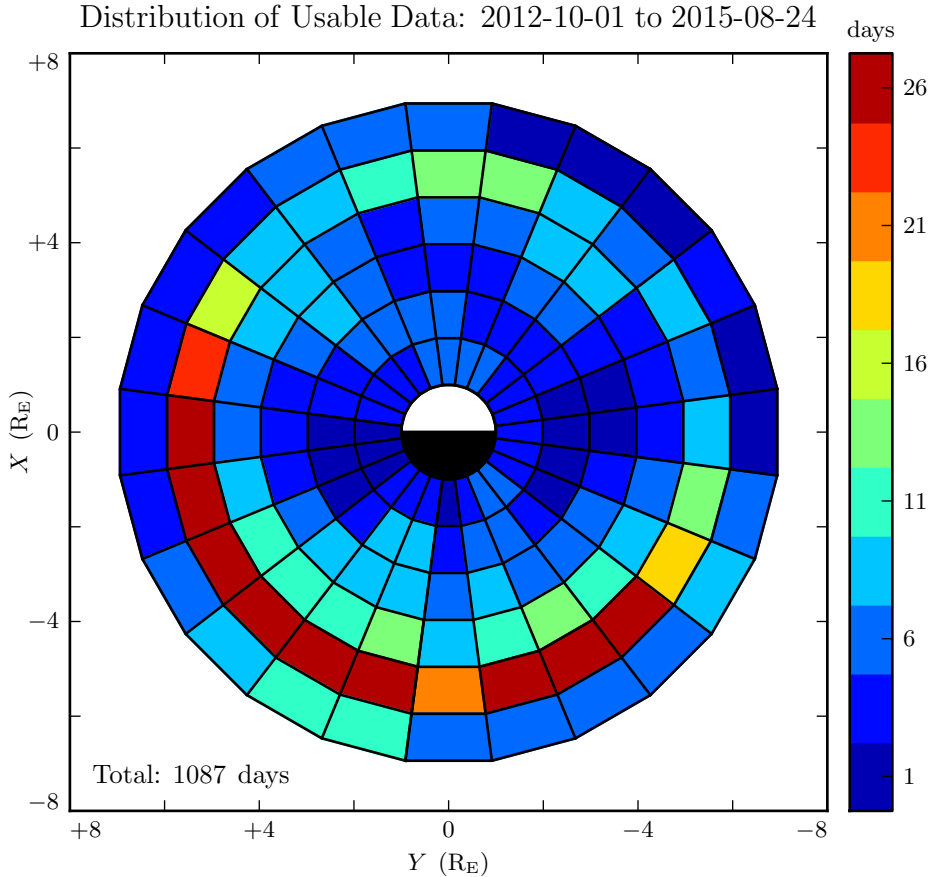


Figure 8.1: Three-dimensional electric field values are computed by assuming $\underline{E} \cdot \underline{B} = 0$. Data is discarded whenever the magnetic field falls within 15° of the spin plane, which introduces a bias against the flanks. Furthermore, the probes have completed one and a half precessions around Earth; the dayside has been sampled once at apogee, and the nightside twice.

1222 perturbation along each axis¹. Each waveform is also shifted horizontally so that its
1223 mean over the thirty minute event is zero.

Frequency-domain Poynting flux is computed from the electric and magnetic field transforms. A factor of L^3 compensates the compression of the flux tube, so that the resulting values are effective at the ionosphere. Poloidal and toroidal Poynting flux, respectively,

¹As in Chapters 5 and 7, B_x refers not to the full magnetic field in the x direction, but to the perturbation in the x direction from the zeroth-order magnetic field.

are given by:

$$\tilde{S}_P \equiv -\frac{L^3}{\mu_0} \tilde{E}_y \tilde{B}_x^* \quad \tilde{S}_T \equiv \frac{L^3}{\mu_0} \tilde{E}_x \tilde{B}_y^* \quad (8.1)$$

1224 The poloidal and toroidal channels are independently checked for Pc4 waves. For each
1225 channel, a Gaussian profile is fit to the magnitude of the Poynting flux, $|\tilde{S}(\omega)|$. If the
1226 fit fails to converge, or if the peak of the Gaussian does not fall within 5 mHz of the
1227 peak value of \tilde{S} , the event is discarded. Events are also discarded if their frequencies
1228 fall outside the Pc4 frequency range (7 mHz to 25 mHz) or if their amplitudes fall below
1229 10^{-2} mW/m² (out of consideration for instrument sensitivity).

1230 Events are discarded if their parity is ambiguous. The electric field and the magnetic
1231 field must be coherent at a level of 0.9 or better (judged at the discrete Fourier transform
1232 point closest to the peak of the Gaussian fit). Any event within 3° of the magnetic
1233 equator is also not used; as discussed in Chapter 3, in order to distinguish an odd mode
1234 from an even mode, it's necessary to know whether the observation is made north or
1235 south of the equator.

1236 **TODO: How much time do the probes spend within 3° of the magnetic equator?**

1237 A visual inspection of events shows that those with broad “peaks” in their spectra
1238 are typically not peaked at all — they are noisy spectra with several spectral features
1239 grouped just closely enough to trick the fitting routine. A threshold is set at a FWHM
1240 of 3 mHz (equally, a standard deviation of 1.27 mHz). Any event with a Gaussian fit
1241 broader than that is discarded.

1242 Notably, events are not filtered on their phase — that is, on the division of their energy
1243 between standing and traveling waves. This is the topic of Section 8.5.

1244 **TODO: First and third harmonics can only be distinguished by guessing at the fre-**
1245 **frequency. Chisham and Orr[14] argue that around 7R_E, frequency around 10 mHz pre-**
1246 **cludes higher harmonics. Or maybe look at [34]?**

1247 **TODO: Are we biased in terms of DST? What's the distribution look like for the good**
1248 **data and for the bad data?**

1249 **8.2 Events by Mode**

1250 The filters described in Section 8.1 yield 762 Pc4 events, the spatial distribution of
1251 which is shown in Figure 8.2. In each bin, the event count is normalized to the amount
1252 of usable data, per Figure 8.1. Bins shown in white contain zero events. The rate in
1253 the bottom corner is an overall mean, weighing each bin equally.

1254 **TODO: Bins should be weighted by L . The small inner bins count too much right now,**
1255 **and are dragging down the average.**

1256 Consistent with previous work, Pc4 events peak on the dayside and are rarely observed
1257 at $L < 4$. Nearly 30 % of the usable data shown in Figure 8.1 is located inside $L = 4$,
1258 yet that data accounts for only 16 of the 762 events.

1259 On the other hand, the present work runs contrary to Dai’s 2015 result in terms of
1260 Pc4 event rates with respect to the plasmapause (not shown). His analysis found Pc4
1261 pulsations to be comparably common inside and outside the plasmapause[17]. In the
1262 present work, only 40 of the 762 events (5 %) fall inside the plasmasphere, despite the
1263 fact that 40 % of the available data falls within the plasmasphere. The disparity is not
1264 likely due to a difference in sampling — Dai’s work, like the present work, uses data
1265 from the Van Allen Probes mission. Rather, the difference is likely due to disagreement
1266 in how the plasmapause is defined. Dai identifies the plasmapause by the maximum
1267 gradient in electron number density, while the present work takes an electron density of
1268 100 /cm^3 to mark the plasmapause².

1269 In Figure 8.3, events are partitioned by parity and polarization, yielding 124 odd poloidal
1270 events, 214 even poloidal events, 415 odd toroidal events, and 83 even toroidal events
1271 — a total of 836 events. The total is greater than 762 because in $\sim 10\%$ of events, the
1272 poloidal and toroidal channels trigger independently. Such cases are marked as a single
1273 event in Figure 8.2, but the toroidal and poloidal events are both shown in Figure 8.3.

1274 Double-triggering can be taken as a vague proxy for event quality. When the channels
1275 both trigger independently, the two events almost always (71 of 74 events) exhibit the
1276 same parity. This suggests a poloidal wave with sufficient power, and a sufficient narrow

²Per ongoing work by Thaller.

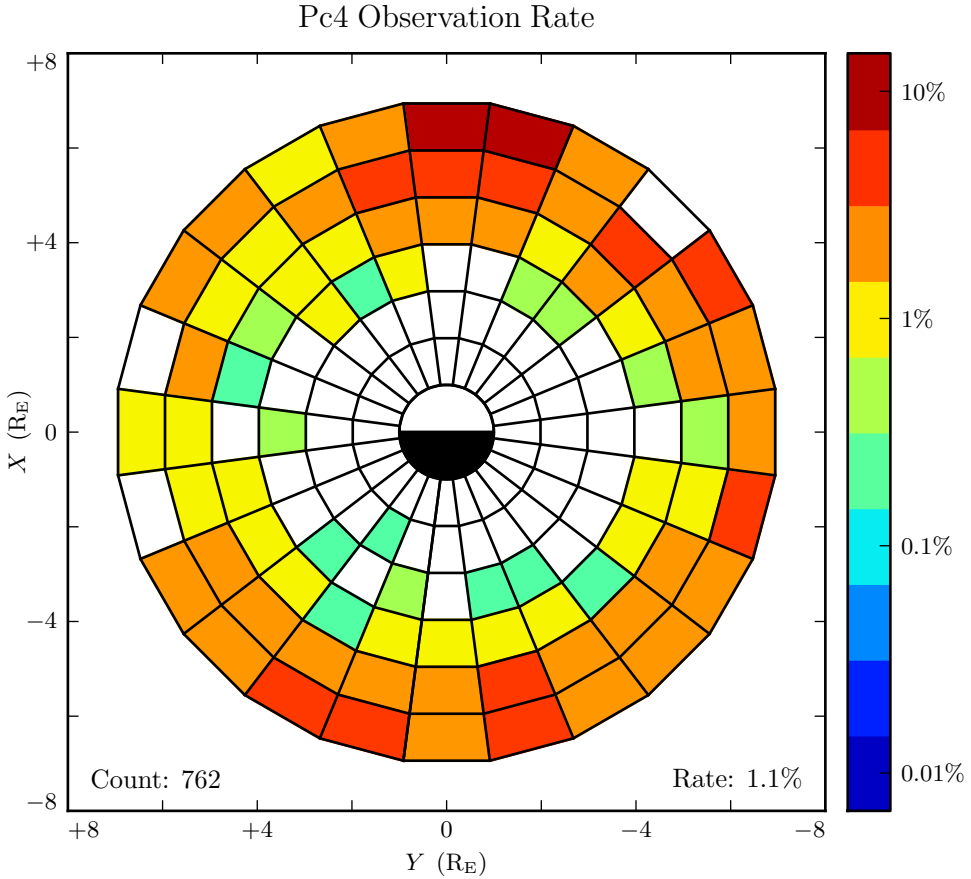


Figure 8.2: The above figure shows the spatial distribution of all 762 observed Pc4 events. Counts are normalized by the amount of usable data in each bin. The value in the bottom-right corner is the mean of the rate in each bin; it's an estimate of how often Pc4 events would be observed if the sampling were distributed uniformly in space. Events where the poloidal and toroidal channel trigger simultaneously ($\sim 10\%$ of cases) are counted as only a single event. Bins shown in white contain zero events.

1277 spectral peak, that it can still be seen after much of its energy has rotated to the toroidal
 1278 mode.

1279 Odd double-triggering events are spread broadly in MLT. They rarely occur twice on the
 1280 same day (23 events spread over 20 days), are observed at comparable rates regardless
 1281 of DST.

1282 Even-harmonic double-triggering events, on the other hand, are mostly seen near noon,
1283 and are significantly more common when $DST < -30$ nT. Even events are also more
1284 concentrated than odd ones. The 48 even-harmonic double-events are spread over 20
1285 days, and 35 of them are spread over just 7 days. This clustering — where the poloidal
1286 and toroidal channel both trigger for five to ten half-hour events in the same day — is
1287 prevalent regardless of DST.

1288 The distribution of even poloidal events in Figure 8.3 is consistent with that reported
1289 by Dai[17]: the observation rate is peaked at noon, and smeared across the dusk side.
1290 Notably, Dai’s work focused on even poloidal waves. While he did not explicitly remove
1291 odd events from his sample, he did introduce a threshold in the magnetic field. This
1292 threshold is preferentially satisfied by even waves (which have a magnetic field antinode
1293 near the equator) compared to odd waves (which have a magnetic field node). Dai
1294 characterized the parity of only a quarter of his events; among those, he found even
1295 harmonics to outnumber odd harmonics ten-to-one.

1296 In fact — to the degree that they can be straightforwardly compared — the distributions
1297 in Figure 8.3 also show agreement with work by Anderson (using AMPTE/CCE[3]),
1298 Kokubun (using ATS6[52]), Liu (using THEMIS[56]), and Motoba (using GOES[70]).
1299 Toroidal events dominate overall, and are primarily seen on the dawn side. Poloidal
1300 events are spread broadly in MLT, with a peak near noon and distinctive odd harmonics
1301 in the early morning.

1302 Crucially, the present work can offer insight into how previous results fit together. Unlike
1303 events considered in previous works, those shown in Figure 8.3 have all been categorized
1304 in terms of both polarization and parity. And, perhaps more importantly, the selection
1305 process has not introduced a bias with respect to polarization or parity (at least not an
1306 obvious one).

1307 Not only does Figure 8.3 show that toroidal events outnumber poloidal events, but it
1308 also shows that toroidal events are predominantly odd harmonics — as opposed to the
1309 primarily-even poloidal events. This may suggest that odd poloidal waves are more
1310 likely than even ones to be driven at low modenumber (allowing a prompt rotation
1311 of that energy to the toroidal mode). One might expect low- m poloidal modes to be

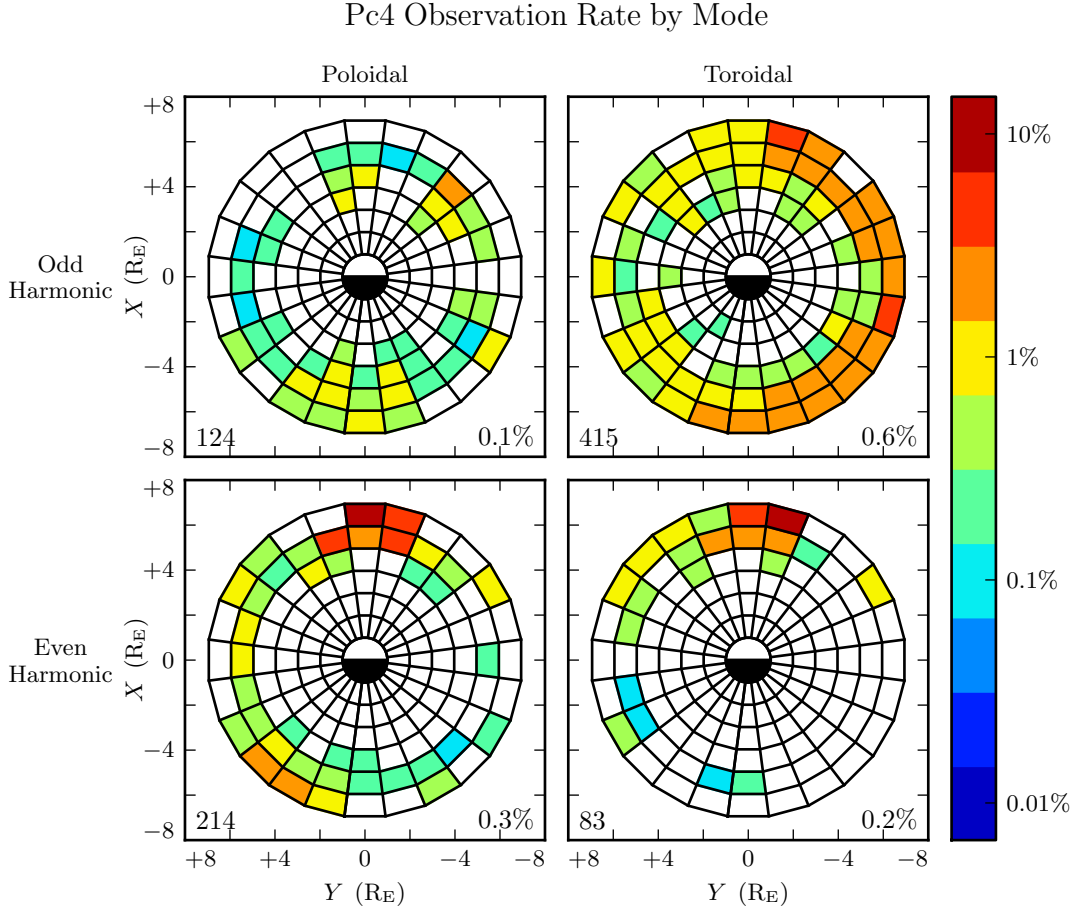


Figure 8.3: The above figure shows the spatial distribution for the same 762 events shown in Figure 8.2, partitioned by polarization and parity. The selection criteria described in Section 8.1 ensure that both properties are known for all events. Event counts are normalized by the time spent by the amount of usable data in each bin. Counts shown in the bottom-left corners do not sum to 762 because some events trigger on both the poloidal channel and the toroidal channel. Bins shown in white contain zero events.

driven by a sudden increase in the solar wind dynamic pressure, for instance. The relative scarcity of odd poloidal observations on the dayside may indicate a short-lived source. At low m , energy rotates to the toroidal mode on the order of a wave period; without an ongoing source, there will be no poloidal wave to observe.

1316 TODO: People have talked about this. Is there a conventional explanation for dawn-dusk asymmetry?

1318 Even poloidal modes and even toroidal modes exhibit similar distributions in space:
1319 both are peaked at noon and smeared across the dusk flank, with little activity on the
1320 dawn side. This is consistent with the idea that the even poloidal mode is a significant
1321 source for the even toroidal mode.

1322 TODO: What else do we want to say here? Or does the rest of the commentary belong
1323 in the later sections? Note that plots in future sections are lower resolution, to make
1324 sure that the number of bins remains much smaller than the number of events.

1325 8.3 Events by Amplitude

1326 One might reasonably be concerned that the spatial distributions presented in Figure 8.3
1327 are dominated by these small events, while Pc4 events large enough to be noteworthy
1328 follow a different distribution entirely. The goal of the present section is to address that
1329 concern.

1330 The distribution of event magnitudes is presented in Figure 8.4, graded based on the
1331 peak of the Gaussian fit of each event's Poynting flux, $|\tilde{S}(\omega)|$. Mean and median
1332 values are listed for each mode. Most events are small, with Poynting flux well below
1333 0.1 mW/m^2 when mapped to the ionosphere. Only a handful of events — 3 out of 762
1334 — exceed 1 mW/m^2 , typically taken to be the threshold at which visible auroral arcs
1335 form. One such event is shown in Figure 8.5.

1336 TODO: Say something about this event? Not really clear what purpose is served by this
1337 example, actually. As a matter of curiosity, the apparent wave activity in the toroidal
1338 channel did not pass the event selection trigger because the electric and magnetic wave-
1339 forms are not coherent.

1340 TODO: The distribution of even poloidal events is flatter in amplitude than the rest.
1341 As the amplitude cutoff increases, so does the proportion of even events.

Amplitude Distribution of Pc4 Events by Mode

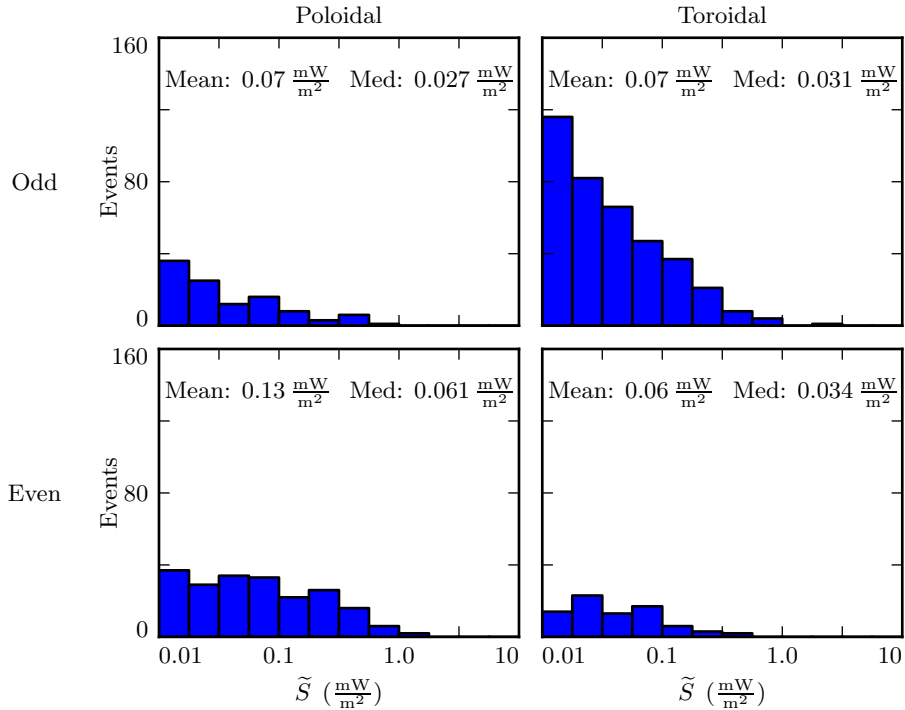


Figure 8.4: TODO: ...

1342 TODO: The distribution of events by mode is reproduced in Figure 8.6 using several different amplitude cutoffs. The qualitative distribution of events does not change.

1343

Waveforms and Spectra: Odd Poloidal Wave

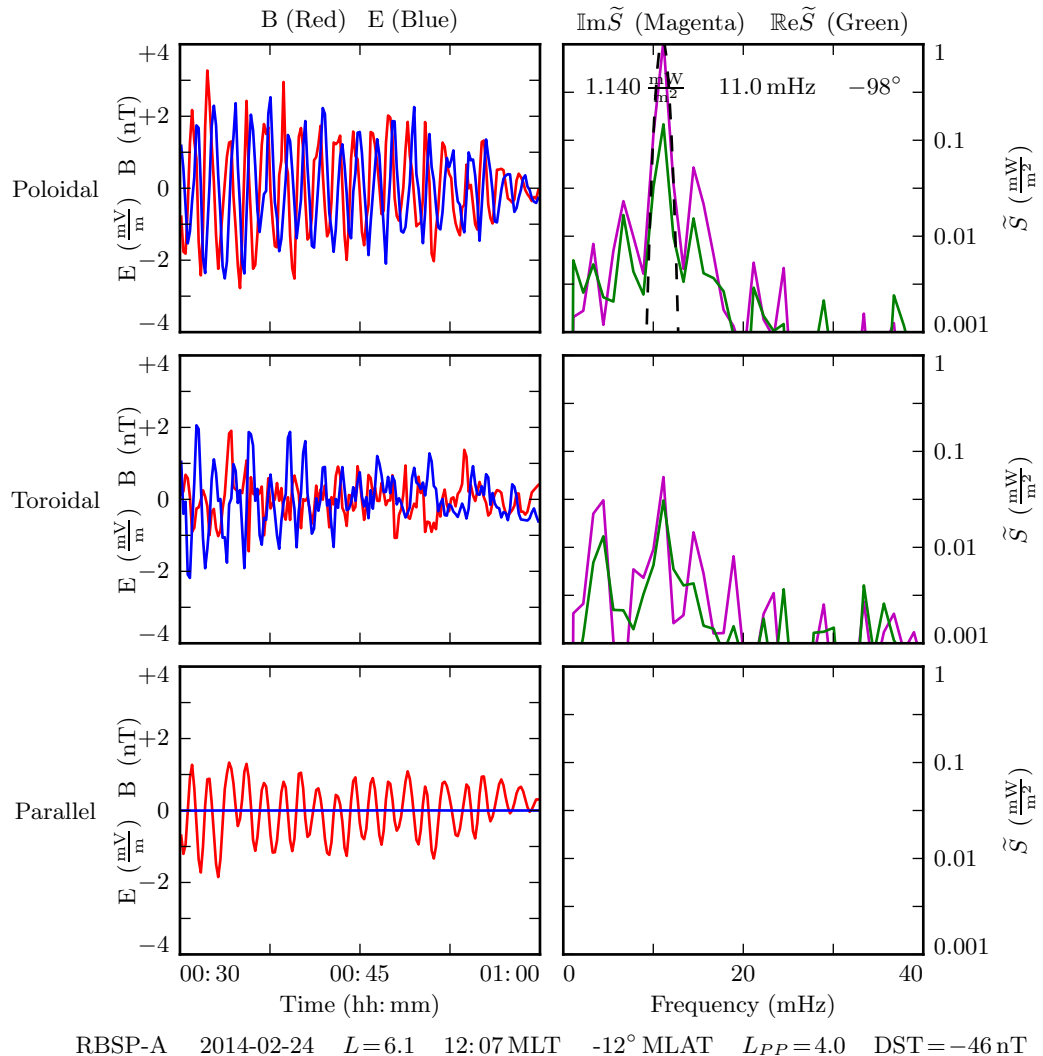


Figure 8.5: **TODO:** ...

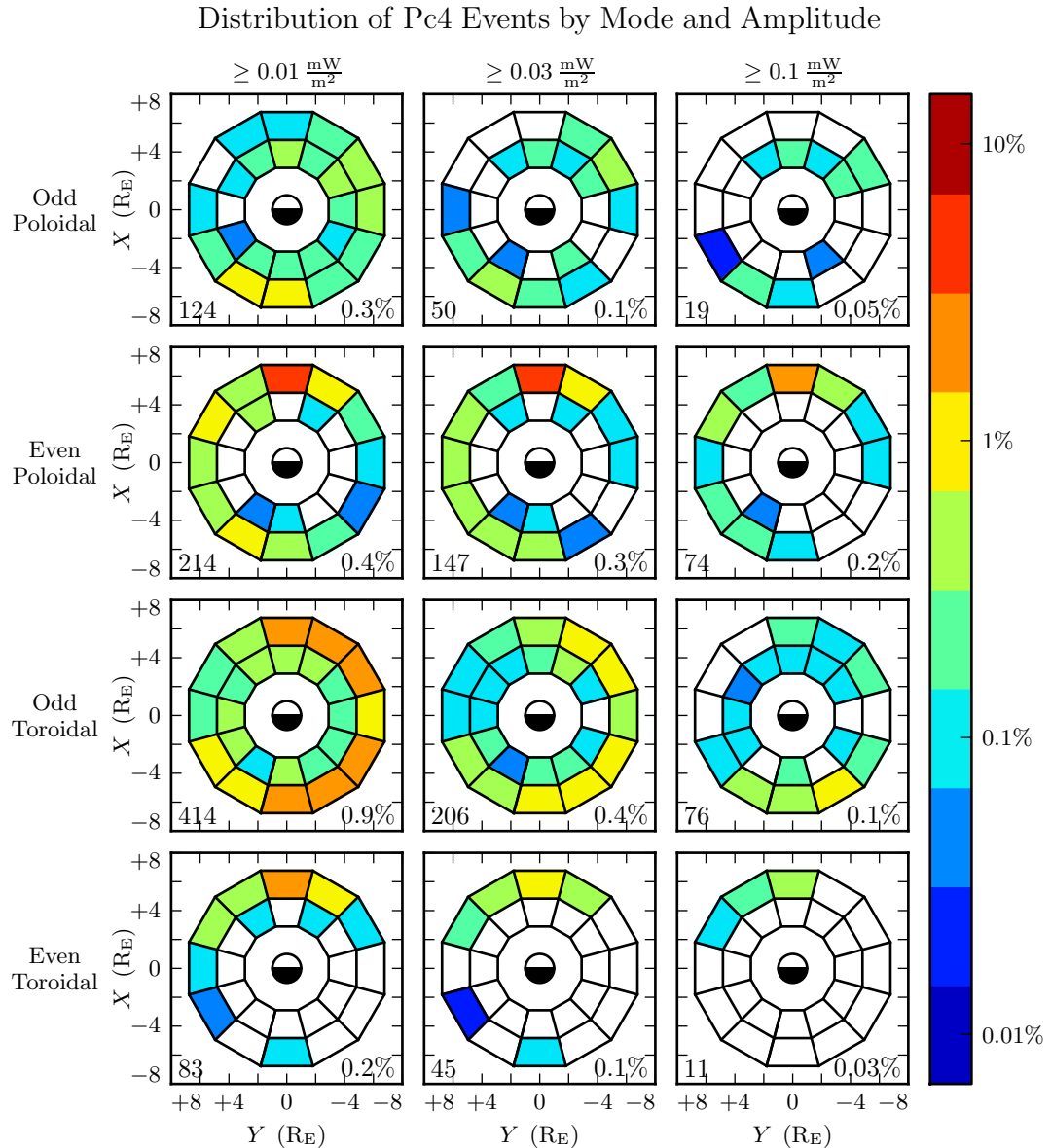


Figure 8.6: TODO: ...

1344 8.4 Events by Frequency

1345 TODO: (Odd) toroidal events exhibit a much stronger peak in frequency than poloidal
1346 events. This is consistent with the fact that toroidal waves align closely with the local
1347 eigenfrequency, while poloidal modes are more smeared in L , as discussed in Section 7.2.
1348 Van Allen Probe observations are mostly concentrated over a small range in L near
1349 apogee.

1350 TODO: Maybe put the Gaussian fit back on top of these distributions? The distributions
1351 are not particularly Gaussian, but it gives a quantitative estimate of the spread.

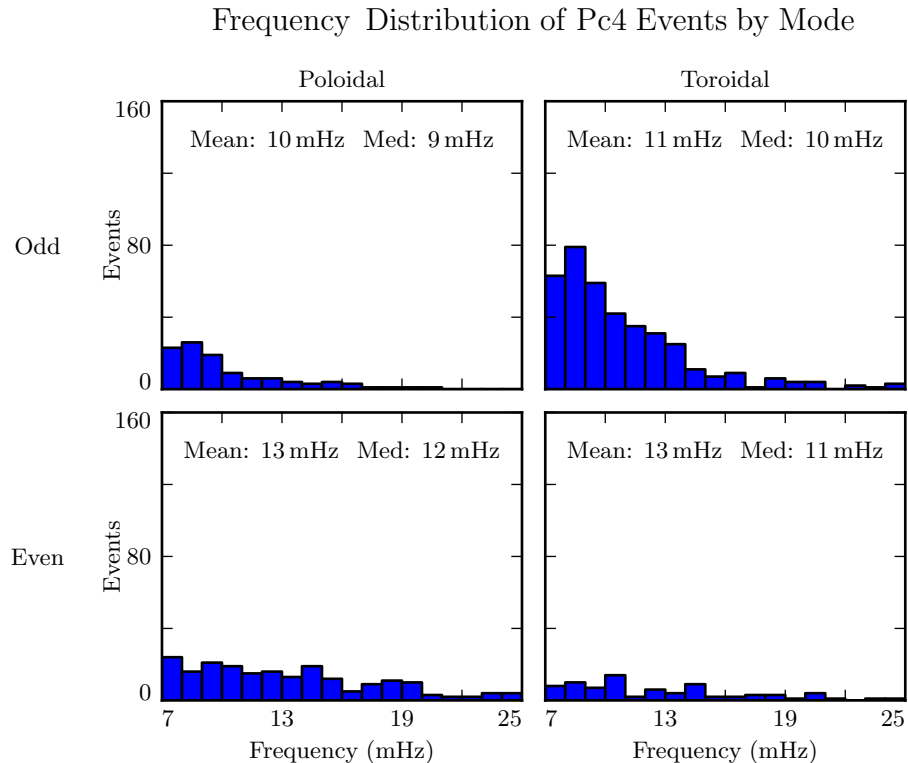


Figure 8.7: TODO: ...

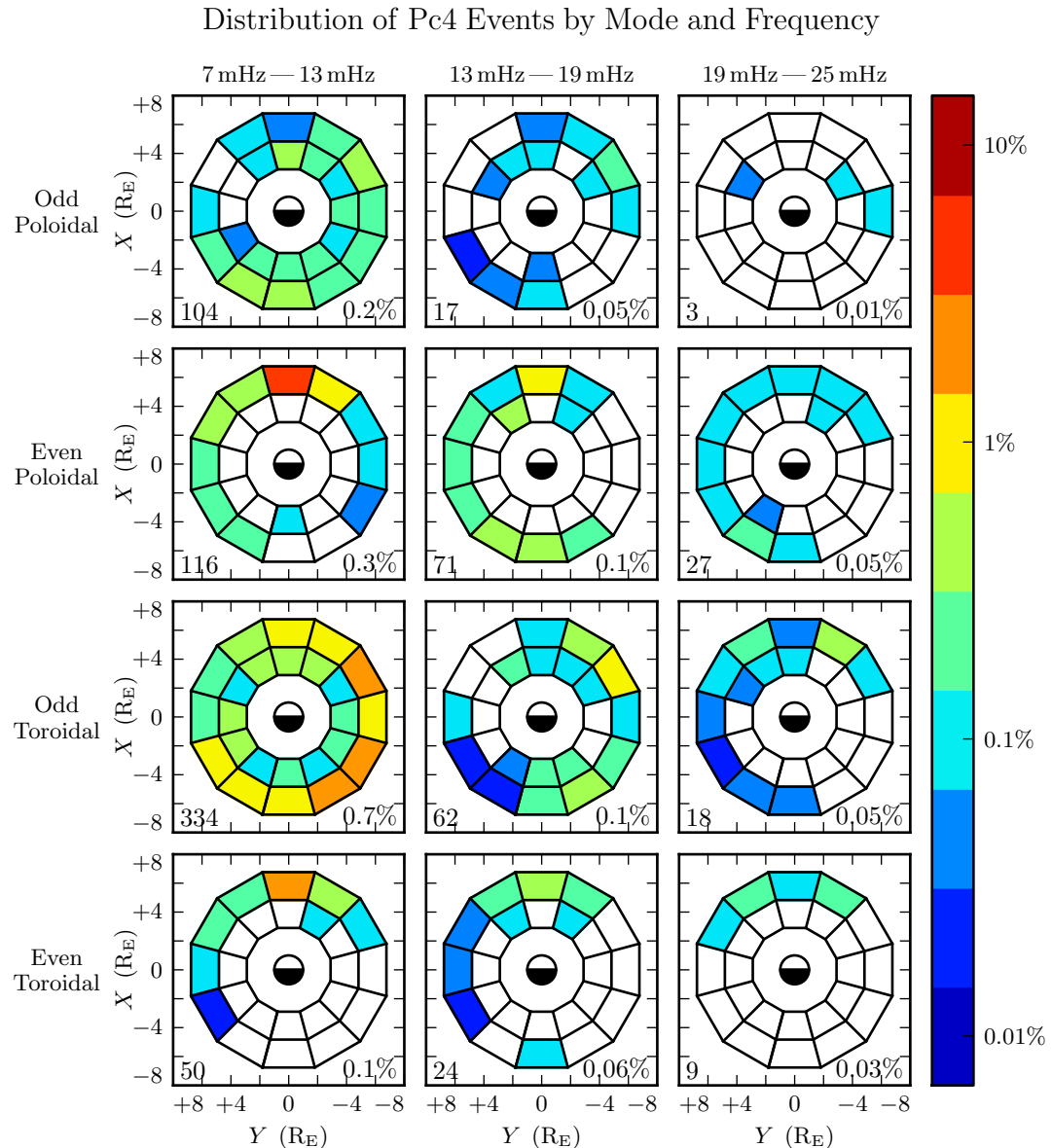


Figure 8.8: TODO: ...

1352 8.5 Events by Phase

1353 The phase of a wave — that is, the phase offset between a wave's electric and magnetic
1354 fields — indicates how its energy is partitioned between the standing and traveling
1355 wave modes. An ideal standing wave has a phase of $\pm 90^\circ$, and thus its Poynting flux is
1356 completely imaginary. A traveling wave, on the other hand, has electric and magnetic
1357 fields in phase (or in antiphase), and is associated with a net movement of energy,
1358 usually toward the ionosphere.

1359 Wave phase is a topic of significant interest, since it allows an estimate to be made of
1360 the wave's lifetime. And, because phase can only be determined using simultaneous
1361 electric and magnetic field measurements, it has only recently become observable.

1362 **TODO: Do people really care about phase, or is it just John?**

The energy per unit volume, and the rate at which energy is carried out of that volume by Poynting flux, are respectively given by:

$$U = \frac{R^3}{2\mu_0} B^2 \quad \frac{\partial}{\partial t} U = \frac{R^2}{\mu_0} EB \cos \varphi \quad (8.2)$$

1363 Where B , E , and R are the characteristic magnetic field magnitude, electric field mag-
1364 nitude, and length scale. The phase, $\varphi \equiv \arctan \frac{\text{Im}S}{\text{Re}S}$, enters because only real Poynting
1365 flux carries energy.

The ratio of the two quantities in Equation (8.2) gives a characteristic timescale over which energy leaves the system

$$\tau \equiv \frac{BR}{2E \cos \varphi} \quad (8.3)$$

1366 In the present case, magnetic fields are on the order of 1 nT and electric fields are on
1367 the order of 1 mV/m. A reasonable scale length might be 10^4 km, the distance traversed
1368 by the probe over the course of a half-hour event (notably, back-to-back events are
1369 unusual).

1370 At a phase of 80° , this timescale is comparable to a Pc4 wave period. At 135° , where
1371 energy is divided evenly between the standing and traveling wave, the timescale is only
1372 7 seconds. A wave with a phase so far from 90° would quickly vanish unless it were
1373 constantly being replenished.

1374 An example of just such an event is shown in Figure 8.9. The left column shows
1375 electric and magnetic field waveforms in blue and red respectively. The right shows
1376 the corresponding spectra: imaginary Poynting flux in magenta (corresponding to the
1377 strength of the standing wave) and real Poynting flux in green (for the traveling wave).
1378 The black line is a Gaussian fit to the magnitude of the Poynting flux.

1379 The poloidal channel shows a mostly-standing wave, with a phase of 79° . The coherent
1380 activity in the compressional magnetic field implies a low azimuthal modenumber, and
1381 thus a fast rotation of energy from the poloidal mode to the toroidal mode. It's likely
1382 the rotation of energy from the poloidal mode is the only thing keeping the toroidal
1383 wave going; its phase is 130° , so its energy should be carried away by Poynting flux
1384 quickly compared to the oscillation of the standing wave.

1385 The selection process described in Section 8.1 does not explicitly consider phase. How-
1386 ever, the discrete Fourier transform is performed over a half-hour time span. An event
1387 with a comparatively short lifetime would be unlikely to register. It's unsurprising to
1388 see the events in Figure 8.10 tightly clustered near 90° .

1389 It's further notable in Figure 8.10 that the odd events are more spread out in phase
1390 than the even events. Near the equator, odd modes have an electric field antinode and
1391 a magnetic field node; per Equation (8.3), an odd mode's lifetime should be longer than
1392 that of an even mode with the same phase.

1393 **TODO:** The spatial distribution of Pc4 events doesn't seem to depend much on phase,
1394 as shown in Figure 8.11.

Waveforms and Spectra: Odd Poloidal Wave and Odd Toroidal Wave

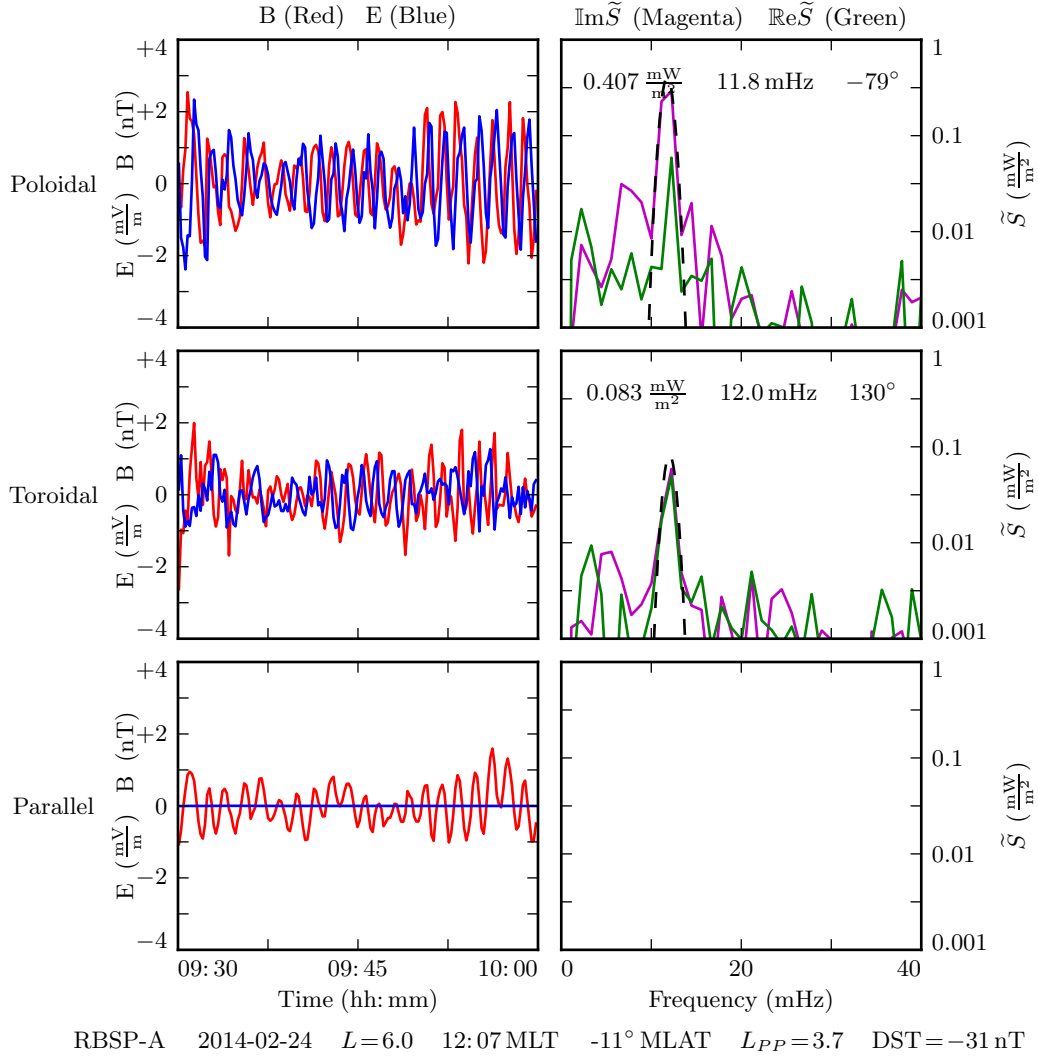


Figure 8.9: The above is a double event, where the poloidal and toroidal channels have been independently selected as events. The poloidal channel shows a wave with most of its energy in the standing wave (phase of 79°). The toroidal mode has a significant traveling component (phase of 130°). The compressional activity implies a low modenumber, which would cause energy to rotate quickly from the poloidal mode to the toroidal mode — evidently at a sufficient rate to replenish the losses due to the traveling mode's real Poynting flux.

Phase Distribution of Pc4 Events by Mode

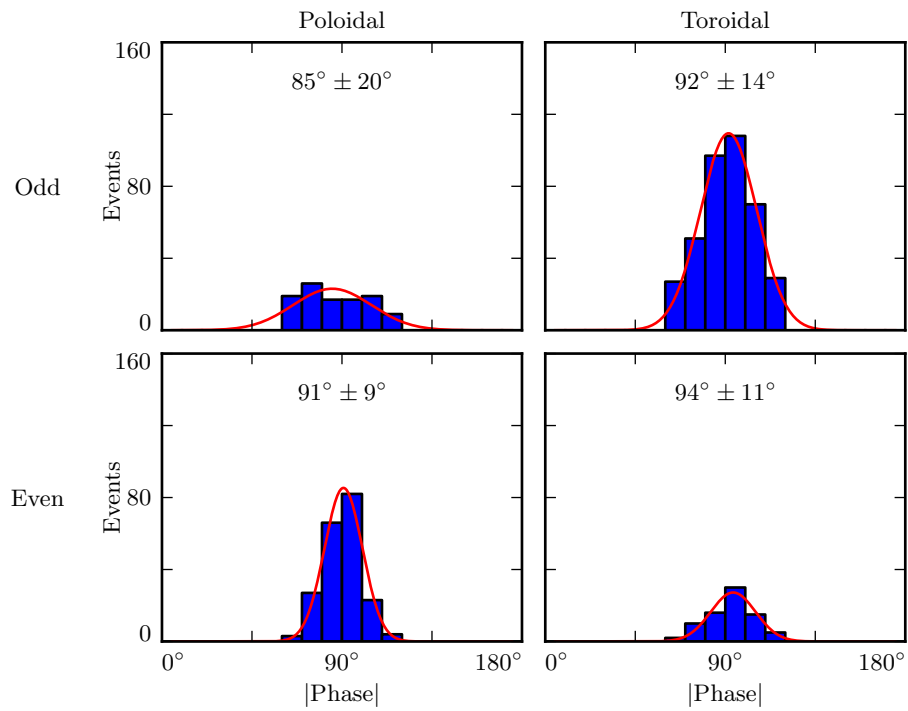


Figure 8.10: **TODO:** ...

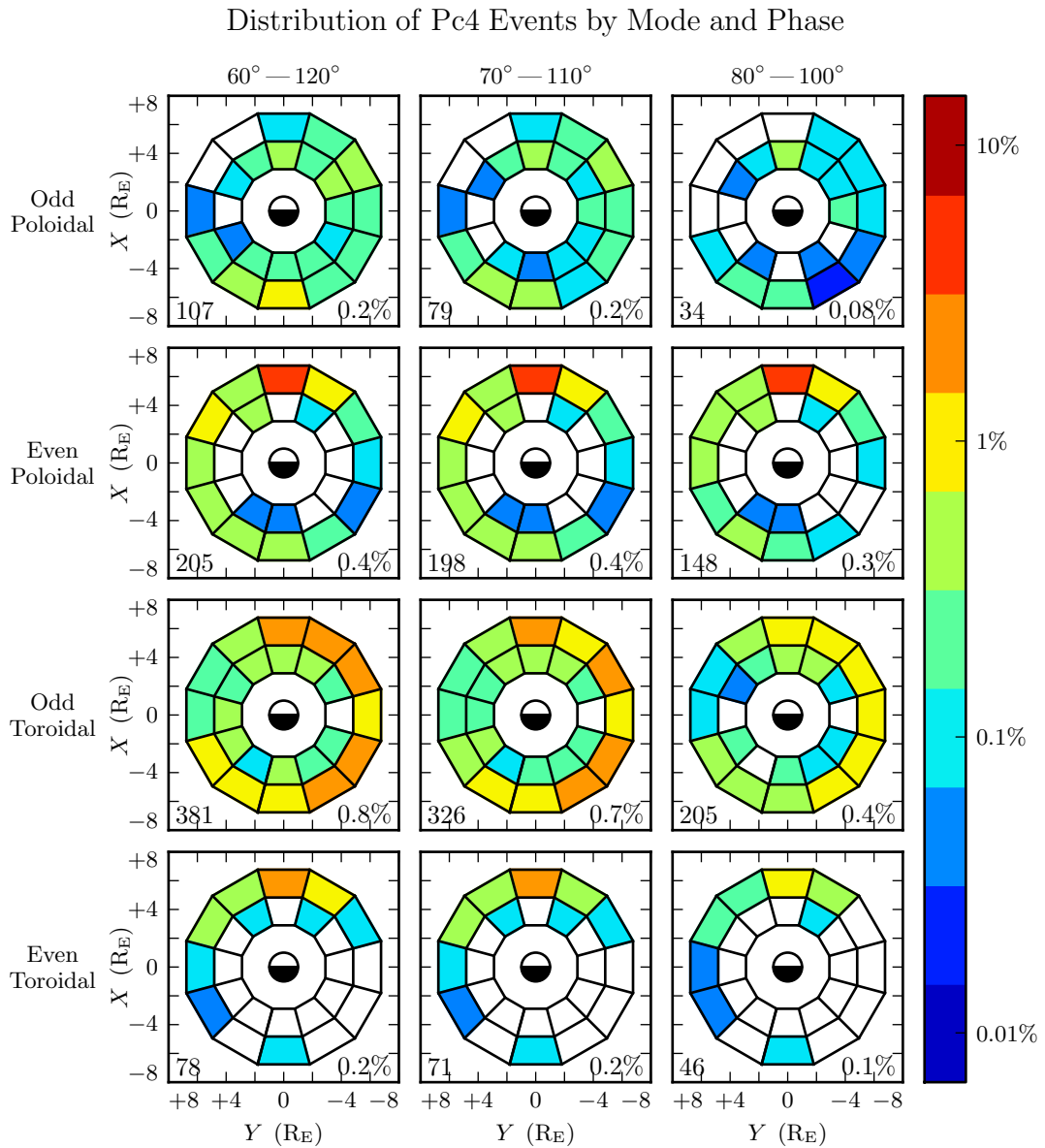


Figure 8.11: TODO: ...

1395 **8.6 Discussion**

1396 **TODO:** ...

1397 **Chapter 9**

1398 **Conclusion**

1399 **9.1 Summary of Results**

1400 TODO: Code development... Chapters 5 and 6

1401 TODO: Make the Git repository public, and link to it.

1402 TODO: Numerical results... Chapter 7

1403 TODO: Re-summarize the Discussion sections, I guess.

1404 TODO: Observational results... Chapter 8

1405 TODO: Link to the Git repository.

1406 **9.2 Future Work**

1407 TODO: Code development.

1408 Arbitrary deformation of grid. Get $\hat{e}_i = \frac{\partial}{\partial u^i} \underline{x}$, then $g_{ij} = \hat{e}_i \cdot \hat{e}_j$, then invert the metric
1409 tensor for contravariant components.

1410 MPI. Time to compute vs time to broadcast. This might make sense for inertial length
1411 scales.

1412 Better ionospheric profiles. Distinction between the dawn and dusk flanks. Maybe even
1413 update the conductivity based on energy deposition — precipitation causes ionization!

1414 IRI ionosphere model. Solar illumination effects.

1415 **TODO:** Numerical work.

1416 More complicated driving. Higher harmonics, non-sinusoidal waveforms. Maybe even
1417 drive based on events?

1418 **TODO:** Analysis of RBSP data.

1419 Basically just do everything over again, twice as well, once the probes have finished
1420 sampling the dayside again.

¹⁴²¹ References

- ¹⁴²² [1] S.-I. Akasofu. The development of the auroral substorm. *Planetary and Space*
¹⁴²³ *Science*, 12(4):273–282, 1964.
- ¹⁴²⁴ [2] H. Alfvén. On the cosmogony of the solar system III. *Stockholms Observatoriums*
¹⁴²⁵ *Annaler*, 14:9.1–9.29, 1946.
- ¹⁴²⁶ [3] B. J. Anderson, M. J. Engebretson, S. P. Rounds, L. J. Zanetti, and T. A. Potemra.
¹⁴²⁷ A statistical study of Pc 3-5 pulsations observed by the AMPTE/CCE magnetic
¹⁴²⁸ fields experiment, 1. occurrence distributions. *J. Geophys. Res.*, 95(A7):10495,
¹⁴²⁹ 1990.
- ¹⁴³⁰ [4] V. Angelopoulos. The THEMIS mission. *Space Science Reviews*, 141(1-4):5–34,
¹⁴³¹ 2008.
- ¹⁴³² [5] K. Birkeland. Expédition norvégienne de 1899-1900 pour l'étude des aurores
¹⁴³³ boréales. *Mat. Naturvidensk. Kl.*, KI(I), 1901.
- ¹⁴³⁴ [6] J. P. Boris. A physically motivated solution of the Alfvén problem. *NRL Memo-*
¹⁴³⁵ *randum Report*, 2167, 1970.
- ¹⁴³⁶ [7] A. Brekke, T. Feder, and S. Berger. Pc4 giant pulsations recorded in Tromsø,
¹⁴³⁷ 1929-1985. *Journal of Atmospheric and Terrestrial Physics*, 49(10):1027–1032,
¹⁴³⁸ 1987.
- ¹⁴³⁹ [8] C. W. Carlson, R. F. Pfaff, and J. G. Watzin. The fast auroral Snapshot (FAST)
¹⁴⁴⁰ mission. *Geophys. Res. Lett.*, 25(12):2013–2016, 1998.

- 1441 [9] A. A. Chan, M. Xia, and L. Chen. Anisotropic alfvén-balloon modes in Earth's
1442 magnetosphere. *J. Geophys. Res. Space Physics*, 99(A9):17351–17366, 1994.
- 1443 [10] L. Chen and A. Hasegawa. A theory of long-period magnetic pulsations: 1. steady
1444 state excitation of field line resonance. *J. Geophys. Res.*, 79(7):1024–1032, 1974.
- 1445 [11] L. Chen and A. Hasegawa. Kinetic theory of geomagnetic pulsations: 1. internal
1446 excitations by energetic particles. *J. Geophys. Res.*, 96(A2):1503, 1991.
- 1447 [12] L. Chen, R. White, C. Cheng, F. Romanelli, J. Weiland, R. Hay, J. V. Dam,
1448 D. Barnes, M. Rosenbluth, and S. Tsai. Theory and simulation of fishbone-type
1449 instabilities in beam-heated tokamaks. Technical report, 1984.
- 1450 [13] C. Z. Cheng and Q. Qian. Theory of ballooning-mirror instabilities for anisotropic
1451 pressure plasmas in the magnetosphere. *J. Geophys. Res.*, 99(A6):11193, 1994.
- 1452 [14] G. Chisham and D. Orr. Statistical studies of giant pulsations (pgs): Harmonic
1453 mode. *Planetary and Space Science*, 39(7):999–1006, 1991.
- 1454 [15] W. D. Cummings, R. J. O'Sullivan, and P. J. Coleman. Standing Alfvén waves in
1455 the magnetosphere. *J. Geophys. Res.*, 74(3):778–793, 1969.
- 1456 [16] L. Dai. Collisionless magnetic reconnection via Alfvén eigenmodes. *Phys. Rev.*
1457 *Lett.*, 102(24), 2009.
- 1458 [17] L. Dai, K. Takahashi, R. Lysak, C. Wang, J. R. Wygant, C. Kletzing, J. Bonnell,
1459 C. A. Cattell, C. W. Smith, R. J. MacDowall, S. Thaller, A. Breneman, X. Tang,
1460 X. Tao, and L. Chen. Storm time occurrence and spatial distribution of Pc4
1461 poloidal ULF waves in the inner magnetosphere: A Van Allen Probes statistical
1462 study. *J. Geophys. Res. Space Physics*, 120:4748–4762, 2015.
- 1463 [18] L. Dai, K. Takahashi, J. R. Wygant, L. Chen, J. Bonnell, C. A. Cattell, S. Thaller,
1464 C. Kletzing, C. W. Smith, R. J. MacDowall, D. N. Baker, J. B. Blake, J. Fennell,
1465 S. Claudepierre, H. O. Funsten, G. D. Reeves, and H. E. Spence. Excitation of
1466 poloidal standing Alfvén waves through drift resonance wave-particle interaction.
Geophys. Res. Lett., 40:4127–4132, 2013.

- 1468 [19] A. W. Degeling, R. Rankin, and Q.-G. Zong. Modeling radiation belt electron
1469 acceleration by ULF fast mode waves, launched by solar wind dynamic pressure
1470 fluctuations. *J. Geophys. Res. Space Physics*, 119(11):8916–8928, 2014.
- 1471 [20] W. D. D’haeseleer, W. N. G. H. J. D. Callen, and J. L. Shohet. *Flux Coordinates*
1472 and *Magnetic Field Structure*. Springer-Verlag, New York, 1991.
- 1473 [21] J. W. Dungey. The attenuation of Alfvén waves. *J. Geophys. Res.*, 59(3):323–328,
1474 1954.
- 1475 [22] J. W. Dungey. Interplanetary magnetic field and the auroral zones. *Phys. Rev.*
1476 *Lett.*, 6(2):47–48, 1961.
- 1477 [23] A. Einstein. Die grundlage der allgemeinen relativitätstheorie. *Ann. Phys.*,
1478 354:769–822, 1916.
- 1479 [24] S. R. Elkington, M. K. Hudson, and A. A. Chan. Acceleration of relativistic
1480 electrons via drift-resonant interaction with toroidal-mode Pc-5 ULF oscillations.
1481 *Geophys. Res. Lett.*, 26(21):3273–3276, 1999.
- 1482 [25] M. J. Engebretson, D. L. Murr, K. N. Erickson, R. J. Strangeway, D. M. Klumpar,
1483 S. A. Fuselier, L. J. Zanetti, and T. A. Potemra. The spatial extent of radial
1484 magnetic pulsation events observed in the dayside near synchronous orbit. *J.*
1485 *Geophys. Res.*, 97(A9):13741, 1992.
- 1486 [26] P. T. I. Eriksson, L. G. Blomberg, A. D. M. Walker, and K.-H. Glassmeier. Poloidal
1487 ULF oscillations in the dayside magnetosphere: a Cluster study. *Ann. Geophys.*,
1488 23(7):2679–2686, 2005.
- 1489 [27] S. Fujita and T. Tamao. Duct propagation of hydromagnetic waves in the upper
1490 ionosphere, 1, electromagnetic field disturbances in high latitudes associated with
1491 localized incidence of a shear Alfvén wave. *J. Geophys. Res.*, 93(A12):14665, 1988.
- 1492 [28] K.-H. Glassmeier. Magnetometer array observations of a giant pulsation event. *J.*
1493 *Geophys.*, 48:127–138, 1980.
- 1494 [29] K.-H. Glassmeier. On the influence of ionospheres with non-uniform conductivity
1495 distribution on hydromagnetic waves. *J. Geophys.*, 54(2):125–137, 1984.

- 1496 [30] K.-H. Glassmeier, S. Buchert, U. Motschmann, A. Korth, and A. Pedersen. Con-
1497 cerning the generation of geomagnetic giant pulsations by drift-bounce resonance
1498 ring current instabilities. *Ann. Geophysicae*, 17:338–350, 1999.
- 1499 [31] K.-H. Glassmeier, D. Klimushkin, C. Othmer, and P. Mager. ULF waves at
1500 mercury: Earth, the giants, and their little brother compared. *Advances in Space
1501 Research*, 33(11):1875–1883, 2004.
- 1502 [32] C. Goertz. Kinetic alfvén waves on auroral field lines. *Planetary and Space Science*,
1503 32(11):1387–1392, 1984.
- 1504 [33] C. K. Goertz and R. W. Boswell. Magnetosphere-ionosphere coupling. *J. Geophys.
1505 Res.*, 84(A12):7239, 1979.
- 1506 [34] C. A. Green. Giant pulsations in the plasmasphere. *Planetary and Space Science*,
1507 33(10):1155–1168, 1985.
- 1508 [35] J. L. Green and S. Boardsen. Duration and extent of the great auroral storm of
1509 1859. *Advances in Space Research*, 38(2):130–135, 2006.
- 1510 [36] C. Greifinger and P. S. Greifinger. Theory of hydromagnetic propagation in the
1511 ionospheric waveguide. *J. Geophys. Res.*, 73(23):7473–7490, 1968.
- 1512 [37] B. C. Hall. *Lie Groups, Lie Algebras, and Representations*. Graduate Texts in
1513 Mathematics. Springer, New York, second edition, 2015.
- 1514 [38] Y. X. Hao, Q.-G. Zong, Y. F. Wang, X.-Z. Zhou, H. Zhang, S. Y. Fu, Z. Y.
1515 Pu, H. E. Spence, J. B. Blake, J. Bonnell, J. R. Wygant, and C. A. Kletzing.
1516 Interactions of energetic electrons with ULF waves triggered by interplanetary
1517 shock: Van allen probes observations in the magnetotail. *J. Geophys. Res. Space
1518 Physics*, 119(10):8262–8273, 2014.
- 1519 [39] L. Harang. *Pulsations in the terrestrial magnetic records at high latitude stations*.
1520 Grondahl, 1942.
- 1521 [40] O. Hillebrand, J. Muench, and R. L. McPherron. Ground-satellite correlative
1522 study of a giant pulsation event. *Journal of Geophysics Zeitschrift Geophysik*,
1523 51:129–140, 1982.

- 1524 [41] W. J. Hughes. The effect of the atmosphere and ionosphere on long period mag-
1525 netospheric micropulsations. *Planet. Space Sci.*, 22:1157–1172, 1974.
- 1526 [42] W. J. Hughes. Magnetospheric ULF waves: A tutorial with a historical perspec-
1527 tive. In M. J. Engebretson, K. Takahashi, and M. Scholer, editors, *Solar Wind*
1528 *Sources of Magnetospheric Ultra-Low-Frequency Waves*, volume 81 of *Geophys.*
1529 *Monogr.*, pages 1–12. American Geophysical Union, Washington, DC, 1994.
- 1530 [43] W. J. Hughes and D. J. Southwood. The screening of micropulsation signals by
1531 the atmosphere and ionosphere. *J. Geophys. Res.*, 81(19):3234–3240, 1976.
- 1532 [44] W. J. Hughes, D. J. Southwood, B. Mauk, R. L. McPherron, and J. N. Barfield.
1533 Alfvén waves generated by an inverted plasma energy distribution. *Nature*,
1534 275(5675):43–45, 1978.
- 1535 [45] J. A. Jacobs, Y. Kato, S. Matsushita, and V. A. Troitskaya. Classification of
1536 geomagnetic micropulsations. *J. Geophys. Res.*, 69(1):180–181, 1964.
- 1537 [46] T. Karlsson and G. T. Marklund. A statistical study of intense low-altitude electric
1538 fields observed by freja. *Geophys. Res. Lett.*, 23(9):1005–1008, 1996.
- 1539 [47] Y. Kato and T. Tsutomu. Hydromagnetic oscillations in a conducting medium
1540 with hall couduct-ivity under the uniform magnetic field. *Science reports of the*
1541 *Tohoku University. Ser. 5, Geophysics*, 7(3):147–164, 1956.
- 1542 [48] M. C. Kelley. *The Earth’s Ionosphere*. Academic Press, San Diego, second edition,
1543 1989.
- 1544 [49] R. L. Kessel. Solar wind excitation of pc5 fluctuations in the magnetosphere and
1545 on the ground. *J. Geophys. Res.*, 113(A4), 2008.
- 1546 [50] D. Y. Klimushkin, P. N. Mager, and K.-H. Glassmeier. Toroidal and poloidal
1547 Alfvén waves with arbitrary azimuthal wavenumbers in a finite pressure plasma
1548 in the earth’s magnetosphere. *Annales Geophysicae*, 22(1):267–287, 2004.
- 1549 [51] S. Kokubun. Observations of Pc pulsations in the magnetosphere: Satellite-ground
1550 correlation. *J. Geomagn. Geoelec*, 32(Supplement2):SII17–SII39, 1980.

- 1551 [52] S. Kokubun, K. N. Erickson, T. A. Fritz, and R. L. McPherron. Local time asymmetry of Pc 4-5 pulsations and associated particle modulations at synchronous orbit. *J. Geophys. Res.*, 94(A6):6607–6625, 1989.
- 1552
- 1553
- 1554 [53] D.-H. Lee and K. Kim. Compressional MHD waves in the magnetosphere: A new approach. *J. Geophys. Res.*, 104(A6):12379–12385, 1999.
- 1555
- 1556 [54] A. S. Leonovich and V. A. Mazur. Structure of magnetosonic eigenoscillations of an axisymmetric magnetosphere. *J. Geophys. Res.*, 105(A12):27707–27715, 2000.
- 1557
- 1558 [55] W. Liu, J. B. Cao, X. Li, T. E. Sarris, Q.-G. Zong, M. Hartinger, K. Takahashi, H. Zhang, Q. Q. Shi, and V. Angelopoulos. Poloidal ULF wave observed in the plasmasphere boundary layer. *J. Geophys. Res. Space Physics*, 118(7):4298–4307, 2013.
- 1559
- 1560
- 1561
- 1562 [56] W. Liu, T. E. Sarris, X. Li, S. R. Elkington, R. Ergun, V. Angelopoulos, J. Bonnell, and K. H. Glassmeier. Electric and magnetic field observations of Pc4 and Pc5 pulsations in the inner magnetosphere: A statistical study. *J. Geophys. Res.*, 114(A12), 2009.
- 1563
- 1564
- 1565
- 1566 [57] W. Liu, T. E. Sarris, X. Li, Q.-G. Zong, R. Ergun, V. Angelopoulos, and K. H. Glassmeier. Spatial structure and temporal evolution of a dayside poloidal ULF wave event. *Geophys. Res. Lett.*, 38(19), 2011.
- 1567
- 1568
- 1569 [58] R. L. Lysak. Magnetosphere-ionosphere coupling by Alfvén waves at midlatitudes. *J. Geophys. Res.*, 109, 2004.
- 1570
- 1571 [59] R. L. Lysak and D. hun Lee. Response of the dipole magnetosphere to pressure pulses. *Geophys. Res. Lett.*, 19(9):937–940, 1992.
- 1572
- 1573 [60] R. L. Lysak and Y. Song. A three-dimensional model of the propagation of Alfvén waves through the auroral ionosphere: first results. *Adv. Space Res.*, 28:813–822, 2001.
- 1574
- 1575
- 1576 [61] R. L. Lysak, C. L. Waters, and M. D. Sciffer. Modeling of the ionospheric Alfvén resonator in dipolar geometry. *J. Geophys. Res. Space Physics*, 118, 2013.
- 1577

- 1578 [62] P. N. Mager and D. Y. Klimushkin. Giant pulsations as modes of a transverse
1579 Alfvénic resonator on the plasmapause. *Earth, Planets and Space*, 65(5):397–409,
1580 2013.
- 1581 [63] I. R. Mann, E. A. Lee, S. G. Claudepierre, J. F. Fennell, A. Degeling, I. J. Rae,
1582 D. N. Baker, G. D. Reeves, H. E. Spence, L. G. Ozeke, R. Rankin, D. K. Milling,
1583 A. Kale, R. H. W. Friedel, and F. Honary. Discovery of the action of a geophysical
1584 synchrotron in the Earth’s Van Allen radiation belts. *Nature Communications*, 4,
1585 2013.
- 1586 [64] I. R. Mann and A. N. Wright. Finite lifetimes of ideal poloidal Alfvén waves. *J.
1587 Geophys. Res.*, 100:23677–23686, 1995.
- 1588 [65] I. R. Mann, A. N. Wright, and A. W. Hood. Multiple-timescales analysis of ideal
1589 poloidal Alfvén waves. *J. Geophys. Res.*, 102(A2):2381–2390, 1997.
- 1590 [66] T. Maynard, N. Smith, S. Gonzalez, et al. Solar storm risk to the North American
1591 electric grid. 2013.
- 1592 [67] K. McGuire, R. Goldston, M. Bell, M. Bitter, K. Bol, K. Brau, D. Buchenauer,
1593 T. Crowley, S. Davis, F. Dylla, H. Eubank, H. Fishman, R. Fonck, B. Grek,
1594 R. Grimm, R. Hawryluk, H. Hsuan, R. Hulse, R. Izzo, R. Kaita, S. Kaye, H. Kugel,
1595 D. Johnson, J. Manickam, D. Manos, D. Mansfield, E. Mazzucato, R. McCann,
1596 D. McCune, D. Monticello, R. Motley, D. Mueller, K. Oasa, M. Okabayashi,
1597 K. Owens, W. Park, M. Reusch, N. Sauthoff, G. Schmidt, S. Sesnic, J. Strachan,
1598 C. Surko, R. Slusher, H. Takahashi, F. Tenney, P. Thomas, H. Towner, J. Valley,
1599 and R. White. Study of high-beta magnetohydrodynamic modes and fast-ion
1600 losses in PDX. *Phys. Rev. Lett.*, 50(12):891–895, 1983.
- 1601 [68] R. L. McPherron. The role of substorms in the generation of magnetic storms.
1602 *Washington DC American Geophysical Union Geophysical Monograph Series*,
1603 98:131–147, 1997.
- 1604 [69] R. L. McPherron, G. K. Parks, D. S. Colburn, and M. D. Montgomery. Satellite
1605 studies of magnetospheric substorms on august 15, 1968: 2. solar wind and outer
1606 magnetosphere. *J. Geophys. Res.*, 78(16):3054–3061, 1973.

- 1607 [70] T. Motoba, K. Takahashi, J. V. Rodriguez, and C. T. Russell. Giant pulsations on
1608 the afternoonside: Geostationary satellite and ground observations. *J. Geophys.*
1609 *Res. Space Physics*, 120:8350–8367, 2015.
- 1610 [71] NASA. Coordinated data analysis (workshop) web.
- 1611 [72] NASA. Near miss: The solar superstorm of july 2012.
- 1612 [73] M. Nicolet. The collision frequency of electrons in the ionosphere. *Journal of*
1613 *Atmospheric and Terrestrial Physics*, 3(4):200–211, 1953.
- 1614 [74] L. G. Ozeke and I. R. Mann. Energization of radiation belt electrons by ring
1615 current ion driven ULF waves. *J. Geophys. Res.*, 113(A2), 2008.
- 1616 [75] E. M. Poulter, W. Allan, E. Nielsen, and K.-H. Glassmeier. Stare radar observa-
1617 tions of a PG pulsation. *J. Geophys. Res.*, 88(A7):5668, 1983.
- 1618 [76] J. A. Proehl, W. Lotko, I. Kouznetsov, and S. D. Geimer. Ultralow-frequency
1619 magnetohydrodynamics in boundary-constrained geomagnetic flux coordinates.
1620 *J. Geophys. Res.*, 107(A9):1225, 2002.
- 1621 [77] H. R. Radoski. A note on oscillating field lines. *J. Geophys. Res.*, 72(1), 1967.
- 1622 [78] H. R. Radoski. A theory of latitude dependent geomagnetic micropulsations: The
1623 asymptotic fields. *J. Geophys. Res.*, 79, 1974.
- 1624 [79] R. Rankin, J. C. Samson, and V. T. Tikhonchuk. Parallel electric fields in dis-
1625 persive shear alfvén waves in the dipolar magnetosphere. *Geophys. Res. Lett.*,
1626 26(24):3601–3604, 1999.
- 1627 [80] B. Rolf. Giant micropulsations at abisko. *J. Geophys. Res.*, 36(1):9, 1931.
- 1628 [81] G. Rostoker, H.-L. Lam, and J. V. Olson. PC 4 giant pulsations in the morning
1629 sector. *J. Geophys. Res.*, 84(A9):5153, 1979.
- 1630 [82] J. C. Samson, L. L. Cogger, and Q. Pao. Observations of field line resonances,
1631 auroral arcs, and auroral vortex structures. *J. Geophys. Res.*, 101(A8):17373–
1632 17383, 1996.

- 1633 [83] H. J. Singer, W. J. Hughes, and C. T. Russell. Standing hydromagnetic waves
1634 observed by ISEE 1 and 2: Radial extent and harmonic. *J. Geophys. Res.*,
1635 87(A5):3519, 1982.
- 1636 [84] D. J. Southwood. Some features of field line resonances in the magnetosphere.
1637 *Planetary and Space Science*, 22(3):483–491, 1974.
- 1638 [85] D. J. Southwood. A general approach to low-frequency instability in the ring
1639 current plasma. *J. Geophys. Res.*, 81(19):3340–3348, 1976.
- 1640 [86] J. Stratton and N. J. Fox. Radiation belt storm probes (RBSP) mission overview.
1641 In *2012 IEEE Aerospace Conference*. Institute of Electrical & Electronics Engi-
1642 neers (IEEE), 2012.
- 1643 [87] E. Sucksdorff. Giant pulsations recorded at sodankyl during 19141938. *Terrestrial*
1644 *Magnetism and Atmospheric Electricity*, 44(2):157–170, 1939.
- 1645 [88] K. Takahashi, J. Bonnell, K.-H. Glassmeier, V. Angelopoulos, H. J. Singer, P. J.
1646 Chi, R. E. Denton, Y. Nishimura, D.-H. Lee, M. Nosé, and W. Liu. Multipoint
1647 observation of fast mode waves trapped in the dayside plasmasphere. *J. Geophys.*
1648 *Res.*, 115(A12), 2010.
- 1649 [89] K. Takahashi, K.-H. Glassmeier, V. Angelopoulos, J. Bonnell, Y. Nishimura, H. J.
1650 Singer, and C. T. Russell. Multisatellite observations of a giant pulsation event.
1651 *J. Geophys. Res.*, 116:A11223, 2011.
- 1652 [90] K. Takahashi, M. D. Hartinger, V. Angelopoulos, K.-H. Glassmeier, and H. J.
1653 Singer. Multispacecraft observations of fundamental poloidal waves without
1654 ground magnetic signatures. *J. Geophys. Res. Space Physics*, 118:4319–4334, 2013.
- 1655 [91] K. Takahashi, R. W. McEntire, A. T. Y. Lui, and T. A. Potemra. Ion flux oscilla-
1656 tions associated with a radially polarized transverse Pc 5 magnetic pulsation. *J.*
1657 *Geophys. Res.*, 95(A4):3717, 1990.
- 1658 [92] K. Takahashi, N. Sato, J. Warnecke, H. Lühr, H. E. Spence, and Y. Tonegawa.
1659 On the standing wave mode of giant pulsations. *J. Geophys. Res. Space Physics*,
1660 97(A7):10717–10732, 1992.

- 1661 [93] B. J. Thompson and R. L. Lysak. Electron acceleration by inertial alfvén waves.
1662 *J. Geophys. Res.*, 101(A3):5359–5369, 1996.
- 1663 [94] S. M. Thompson and M. G. Kivelson. New evidence for the origin of giant pulsations.
1664 *J. Geophys. Res.*, 106(A10):21237–21253, 2001.
- 1665 [95] V. T. Tikhonchuk and R. Rankin. Electron kinetic effects in standing shear alfveén
1666 waves in the dipolar magnetosphere. *Physics of Plasmas*, 7(6):2630, 2000.
- 1667 [96] B. T. Tsurutani, W. D. Gonzalez, G. S. Lakhina, and S. Alex. The extreme
1668 magnetic storm of 12 september 1859. *Journal of Geophysical Research: Space
1669 Physics*, 108(A7), 2003. 1268.
- 1670 [97] A. Y. Ukhorskiy. Impact of toroidal ULF waves on the outer radiation belt elec-
1671 trons. *J. Geophys. Res.*, 110(A10), 2005.
- 1672 [98] J. Veldkamp. A giant geomagnetic pulsation. *Journal of Atmospheric and Ter-
1673 restrial Physics*, 17(4):320–324, 1960.
- 1674 [99] J. A. Wanliss and K. M. Showalter. High-resolution global storm index: Dst versus
1675 sym-h. *Journal of Geophysical Research: Space Physics*, 111(A2):n/a–n/a, 2006.
1676 A02202.
- 1677 [100] C. L. Waters, R. L. Lysak, and M. D. Sciffer. On the coupling of fast and shear
1678 Alfvén wave modes by the ionospheric Hall conductance. *Earth Planets Space*,
1679 65:385–396, 2013.
- 1680 [101] C. L. Waters and M. D. Sciffer. Field line resonant frequencies and ionospheric
1681 conductance: Results from a 2-d MHD model. *J. Geophys. Res.*, 113(A5), 2008.
- 1682 [102] D. M. Wright and T. K. Yeoman. High-latitude HF doppler observations of ULF
1683 waves: 2. waves with small spatial scale sizes. *Ann. Geophys.*, 17(7):868–876,
1684 1999.
- 1685 [103] J. R. Wygant, A. Keiling, C. A. Cattell, R. L. Lysak, M. Temerin, F. S. Mozer,
1686 C. A. Kletzing, J. D. Scudder, V. Streltsov, W. Lotko, and C. T. Russell. Evidence
1687 for kinetic alfvn waves and parallel electron energization at 46 re altitudes in the

- 1688 plasma sheet boundary layer. *Journal of Geophysical Research: Space Physics*,
1689 107(A8):SMP 24–1–SMP 24–15, 2002.
- 1690 [104] B. Yang, Q.-G. Zong, Y. F. Wang, S. Y. Fu, P. Song, H. S. Fu, A. Korth, T. Tian,
1691 and H. Reme. Cluster observations of simultaneous resonant interactions of ULF
1692 waves with energetic electrons and thermal ion species in the inner magnetosphere.
1693 *J. Geophys. Res.*, 115(A2), 2010.
- 1694 [105] K. Yee. Numerical solution of initial boundary value problems involving maxwell's
1695 equations in isotropic media. *IEEE Trans. Antennas Propagat.*, 14(3), 1966.
- 1696 [106] T. K. Yeoman and D. M. Wright. ULF waves with drift resonance and drift-bounce
1697 resonance energy sources as observed in artificially-induced HF radar backscatter.
1698 *Ann. Geophys.*, 19(2):159–170, 2001.
- 1699 [107] Q.-G. Zong, X.-Z. Zhou, X. Li, P. Song, S. Y. Fu, D. N. Baker, Z. Y. Pu, T. A.
1700 Fritz, P. Daly, A. Balogh, and H. Réme. Ultralow frequency modulation of ener-
1701 getic particles in the dayside magnetosphere. *Geophys. Res. Lett.*, 34(12), 2007.
- 1702 [108] Q.-G. Zong, X.-Z. Zhou, Y. F. Wang, X. Li, P. Song, D. N. Baker, T. A. Fritz,
1703 P. W. Daly, M. Dunlop, and A. Pedersen. Energetic electron response to ULF
1704 waves induced by interplanetary shocks in the outer radiation belt. *J. Geophys.
1705 Res.*, 114(A10), 2009.